NASA CONTRACTOR
REPORT

NASA CR-1445

# EMPIRICALLY DETERMINED WIND AND SCALE EFFECTS ON HOT GAS RECIRCULATION CHARACTERISTICS OF JET V/STOL AIRCRAFT

*by Patrick E. Ryan and Wayne J. Cosgrove*

*Prepared by*
BELL AEROSYSTEMS COMPANY
Buffalo, N. Y.
*for Langley Research Center*

NATIONAL AERONAUTICS AND SPACE ADMINISTRATION • WASHINGTON, D. C. • OCTOBER 1969

# EMPIRICALLY DETERMINED WIND AND SCALE EFFECTS

# ON HOT GAS RECIRCULATION CHARACTERISTICS

# OF JET V/STOL AIRCRAFT

.By Patrick E. Ryan and Wayne J. Cosgrove

Distribution of this report is provided in the interest of
information exchange.     Responsibility for the contents
resides in the author or organization that prepared it.

Issued by Originator as Report No. 2099-956005

# ABSTRACT

The results from a small scale experimental investigation into the engine inlet temperature rise and recirculating flow field caused by the hot exhaust gases from various simulated V/STOL lift jet engine arrangements in static proximity to ground are presented in this report.

The objective was to evaluate the effect of wind and geometric model scale on the recirculating flow field and engine inlet air temperature rise. The effect of engine height, exhaust deflection angle, angle of attack, exhaust nozzle geometry, relative wind speed and direction, and wing planform are included.

The tests were conducted at the Bell Aerosystems Jet Impingement Test Facility which provided simulated inlet and exhaust conditions typical of full scale turbojet engines.

# CONTENTS

CONTENTS (cont)

# EMPIRICALLY DETERMINED WIND AND SCALE EFFECTS

## ON HOT GAS RECIRCULATION CHARACTERISTICS

## OF JET V/STOL AIRCRAFT

By Patrick E. Ryan and Wayne J. Cosgrove
Bell Aerosystems Company

## SUMMARY

Small scale tests were conducted at the Bell Aerosystems Jet Impingement Test Facility during 1968 to investigate the Inlet Temperature Rise (ITR) and hot gas recirculation of three basic configurations representative of jet V/STOL aircraft. This program was sponsored by the National Aeronautics and Space Administration's Langley Research Center under Contract NAS1-7463.

Small scale lift jet engine models (approximately 1/16) and a small scale model (0.24) of a NASA jet V/STOL aircraft model were operated at full scale exhaust conditions (1200°F, and exhaust total pressure ratio from 1.7 to 2.0) so as to maintain exhaust momentum similitude. The major test parameters included wind speed ($V_\infty$) and direction ( $\theta$ ), model height above ground ($h/D_e$) exhaust deflection angle (EDA), angle of attack ($\alpha$), wing planform to jet exhaust area ratio ($S/S_j$), and model geometry.

Temperature time histories measured in and about the models were used to compute steady state values of ITR and near field temperatures. Smoke flow pattern photographs, tufts, and ground flow patterns were used to evaluate recirculation patterns.

Ground winds were found to distort the recirculation of hot gases such as to result in maximum ingestion at approximately 30 fps. Wind direction attenuated ITR as did the presence of wings and exhaust deflection angles. Insight was gained into the structure and distortion of the flow field as affected by wind.

Small scale ITR data based on full scale exhaust conditions may be used to reliably assess full scale gross design effects on ITR.

# INTRODUCTION

One of the most critical problems unique to jet V/STOL aircraft when operating near the ground is hot gas ingestion or inlet temperature rise (ITR). This ingestion of heated air into the lift engine inlets can result in a severe loss in engine thrust, such as to prevent takeoff or cause a hard landing.

Several investigations have been conducted at both large and small scale (Reference 1 through 9) and much insight has been gained; however, many important questions still remain unanswered. Two of these are: (1) What is the effect of ground wind on ITR? and (2) Is there an ITR scale effect associated with geometric model scale?

The first question is significant because winds can result in either an increase or decrease in ITR. Proper ground wind heading of a jet VTOL aircraft during take-off or landing could mean the difference between an aborted or successful mission.

The second question is economically important. If small scale test data is found reliable, then the necessary future experimental investigations may be more economically accomplished through the use of more versatile models and test facilities.

These two questions were experimentally investigated during the course of this program and the results are presented in this report. The tests were conducted out-doors at the Bell Aerosystems Jet Impingement Test Facility. Small scale lift jet engine models used in the Reference 2 tests and a specially constructed (0.24) scale model of the jet V/STOL aircraft model used in Reference 3 were used during this program. The major test parameters included wind speed and direction, model height above ground, exhaust deflection angle, angle of attack, wing planform to total jet exhaust area ratio, and model geometry.

Appendix A presents a theoretical derivation of hot gas recirculation scaling parameters based on a dimensional analysis. This analysis, made by V. Krishnamoorthy of Bell Aerosystems, is presented in this report in the interest of information exchange and to provide further insight into the complexities inherent in hot gas ingestion scaling.

# SYMBOL LIST

| | |
|---|---|
| $d_e$ | nozzle exit diameter, in. (m) |
| $D_e$ | nozzle effective diameter (diameter of circle whose area is equal to the sum of the areas of all the individual nozzles), in. (m) |
| EDA | outward exhaust deflection angle, deg (measured from the vertical). |
| h | height above ground plane, in. (m) |
| ITR | inlet temperature rise above ambient, $^\circ$F. |
| M | Mach number |
| P, p | pressure, psf (N/m$^2$) |
| q | dynamic pressure, psf (N/m$^2$) |
| r | ground jet peeling radius of curvature, ft. (m) |
| R | radial distance along ground plane from exhaust pattern center, ft. (m) |
| S | wing planform area, in.$^2$ (m$^2$) |
| $S_j$ | total exhaust area at nozzle exit, in.$^2$ (m$^2$) |
| t | time, seconds |
| T | Temperature, $^\circ$F |
| $\triangle$T | temperature difference above ambient, $^\circ$F |
| $T_R$ | temperature ratio $-(T-T_{amb})/(T_{ex}-T_{amb})$ |
| T.C. | thermocouple |
| $V_\infty$ | wind speed, fps (m/sec) |
| $V_R$ | velocity ratio, $V/V_j$ |
| $\dot{w}$ | mass flow rate, lbm/sec (kg/sec) |

3

| | |
|---|---|
| x | distance along longitudinal axis of jet, in. (m) |
| y | engine spacing – distance between engine centerlines at EDA pivot point, in. (m) |
| $\alpha$ | angle of attack, deg. |
| $\delta$ | jet exhaust impingement angle, deg. (measured from the vertical) |
| $\gamma$ | ratio of specific heats |
| $\theta$ | wind azimuth angle, deg. |
| $\rho$ | density, slug/ft$^3$ (kg/m$^3$) |
| $\chi$ | full scale wind azimuth angle, deg. ($\chi = -\theta$) |

## Subscripts

| | |
|---|---|
| amb | ambient condition |
| bar | barometric |
| ex | exit condition |
| in | inlet condition |
| j | jet nozzle exit condition |
| x | condition along jet longitudinal axis |

4

# TEST FACILITY, MODELS, AND APPARATUS

## Jet Impingement Test Facility

A recent photograph of the outdoor Jet Impingement Test Facility is presented in Figure 1. The facility provides variable hot exhaust gas flows typical of conventional jet engine exhaust temperatures and pressures. Simulated engine inlet flows are induced by a vacuum producing steam ejector system. Facility controls and instrumentation readouts are located in the adjacent Aerodynamics Laboratory.

Filtered air and JP-4 fuel are metered to combustors in the test area. The combustor cans and the vacuum supply lines are mounted on an overhead track assembly which permits one combination to be positioned relative to the other. This feature provides a means for easily changing the separation distance between the simulated engines in the model. The burner exhaust flow is ducted through relatively short insulated pipes to the exhaust chambers in the model. Scaled flows at typical jet engine exhaust temperatures up to 1700°F can be produced. The desired exhaust conditions (pressure ratio and temperature) are controlled by simultaneous adjustments of the fuel and air supply. During these tests a nominal exhaust flow rate of from 2.0 to 2.3 lb/sec was maintained.

Model engine inlet flow induced by the steam jet ejector system may be controlled to equal the hot gas exhaust flow rate.

The facility ground plane is rectangular, smooth and level to a minimum radial distance of 13 ft (approximately 49 equivalent diameters). A large (42 in. by 12 in.) quick acting hydraulically operated trap door is located in the ground plane directly beneath the model. The trap door opens to ducting beneath the ground plane which carries the hot jet exhaust gases away from the test site prior to test start. This minimizes preheating of the surrounding ground plane and model during the pretest engine setup conditions, and provides an exact reference point for test start time.

The hinged roof of the test facility is raised to eliminate any trapping of hot gases in the test area during test operations. During inclement weather, the roof is closed to protect the test area and equipment.

The model support and model flow systems are supported from above by a single, high pressure hydraulic actuator. This provides unobstructed space around the model and permits vertical positioning of the model to be remotely controlled from the control panel in the Aerodynamics Laboratory. A manually operated mechanism permits setting the model at any desired angle of attack up to approximately 15 degrees.

5

## Pod (circ) and Dual (circ) Models

The Pod (circ) and Dual (circ) Models described in detail in Reference 2, were used during the first phase of this test program to simulate wing tip mounted and isolated lift jet engines. Similar fabrication and installation techniques were employed for both models. Each incorporated separate closed systems to simulate inlets and exhausts of turbojet engines. Insulation was provided between these systems to minimize heat transfer. Cowlings were fitted about the engines to provide a smooth, external flow surface for the simulated turbojet engines. Insulation was also provided in the space between the model hardware and the cowling.

Turning vanes which were necessary to obtain the desired exhaust jet quality and vertical jet flow were installed inside the exhaust chambers just upstream of the nozzle exits. A set of interchangeable elbows were provided which could be installed in the inlet and exhaust supply ducts near the engines to obtain outward exhaust deflection angles of 10 and 20 deg. The scale of the models is 1/16, when based upon a representative V/STOL fighter airplane design with a gross weight of 35,000 lb, a wing loading of 100 lb/ft$^2$, and a thrust-to-weight ratio of 1.15.

The models were designed to the following nominal conditions:

(a)    Exhaust gas temperature = 1200°F

(b)    Ratio of exhaust gas specific heats, $\gamma$ = 1.33

(c)    Total exhaust flow rate, $\dot{w}_{ex}$ = 2.4 lb/sec

(d)    Exit Mach number, $M_{ex}$ = 1.0

(e)    Total inlet flow rate, $\dot{w}_{in}$ = 2.4 lb/sec

(f)    Inlet Mach number, $M_{in}$ = 0.3

(g)    Inlet total temperature = 60°F

(h)    Inlet total pressure = 14.4 psia

The design requirements resulted in total inlet and exhaust areas of 14.6 in.$^2$ and 7.2 in.$^2$, respectively. The exit total pressure ratio was held constant at 2.0 during the ITR tests.

The Pod (circ) model, shown installed in the facility in the photograph of Figure 2, is representative of a cluster of three vertically oriented lift engines in each of two lift engine pods. One engine pod is designated as engine No. 1 and the other as engine No. 2. The simulated engines within each pod are designated as inlet A, B, and C. Instead of the wing shown in the photograph, a larger wing ($S/S_j$ = 100) was used during these tests. The lateral spacing of the engine pods was $y/D_e$ = 8.6.

The model features individual suction tubes leading from each of the wooden bellmouth inlets (1.76 inches diameter each). These tubes are attached by a flange to a single inlet suction pipe for each engine. The exhaust gases flow through a tapered supply tube into the exhaust chamber, and thence through individual circular exhaust nozzles each of which are 1.25 inches in diameter.

The dual (circ) model represents two separated turbojet engines and is shown installed in the test facility above the open trap door in the photograph of Figure 3. The cowling is removed to show the one-quarter inch slab of insulation between the hot exhaust chamber and the inlet chamber. The wooden bellmouth inlets (3.09 inches diameter), the thermocouple leads, and the inlet and exhaust flow supply tubes are visible. The distance between the engines was fixed and this space was devoid of obstructions so that the hot exhaust gases could recirculate unimpeded to the engine inlets, thereby giving a measure of the most severe ingestion possible for jet VTOL aircraft. Subsequently, a rectangular wing (aspect ratio = 4.24) with planform to jet area ratio $(S/S_j)$= 100 was located in this space to determine gross effects of aircraft configuration on ITR. The spacing of the dual (circ) engines was $y/D_e$ = 10.0.

## Scaled NASA Model

During the second phase of this test program, two basic configurations of a 1/4 scale model of the NASA model described in Reference 3 were used. The high delta wing configurations with planform to jet exit area ratios $(S/S_j)$ of 43 and 86 were simulated for both the top inlet and forward facing side inlet configurations using the rectangular exhaust nozzle arrangement. The inlet and exhaust flows were simulated using one combustor can and the steam ejector system of the Jet Impingement Test Facility. The exhaust total pressure ratio was held constant at 1.7 with exhaust gas temperature equal to 1200°F. Figure 4 shows the top inlet configuration of the scaled NASA model installed in the test facility. The exhaust gases were supplied individually to each of the four 1.49 inch diameter convergent exhaust nozzles. The inlet line was similarly divided such that inlet flows were induced individually through each of the four 1.92 inch diameter bellmouth inlets of the top inlet configuration and each of the forward facing side inlets.

Except for the unavoidable compromise at the aft end of the fuselage (see Figure 5), external model surface scaling was closely maintained to provide a firm basis from which ITR scale effects might be assessed.

## Apparatus

Wind machine. - A wind machine with an 8 x 10 foot exit section was used to produce simulated ground wind velocities up to 55 fps. It was variously positioned in a 90 degree arc about the test facility ground plane to provide simulated ground winds at various headings to the model.

Hot wire anemometer. - A commercially available hot wire anemometer or as called by the manufacturer, "air velocity meter", was used to measure wind transients. The sensing element consisted of two thin platinum filaments 0.188 inches long oriented at right angles to one another at the tip of the probe. Each is 0.0005 inches in diameter, and the constant resistance ratio principle is used. This crossed wire technique permitted a measure of both wind magnitude and direction. The probe was simply immersed in the air stream, and a continuous accurate measurement of velocity was read directly from a meter and permanently recorded on an oscillograph.

Visual aids. - Smoke, ground flow patterns, and tufts were used to assist in the qualitative assessment of the recirculating flow fields. Two high speed (approximately 20 frames per second) 70 mm sequence cameras were used to photograph the smoke paths. A portable smoke generating system was used to apply puffs or continuous streams of smoke at any selected point in space about the model. The intensely white and very dense smoke afforded an excellent means of photographic coverage as well as visual observation.

The longitudinal displacement of the NASA model exhaust nozzles due to thermal expansion was measured by utilizing a surveyor's transit. It was also used in conjunction with ground flow patterns, to determine the degree of vertical alignment of the exhaust jets.

Auxiliary ground plane. - An auxiliary ground plane (visible in Figure 4) was positioned above the fixed ground plane for use with the scaled NASA model. The space between the ground planes (approx. 12 inches) permitted the boundary layer, which was built up in the diffuser of the wind machine and along the fixed ground plane, to pass underneath the auxiliary ground plane. The dimensions of this rectangular ground plane (8 x 10 feet) simulated the ground plane size in Reference 3. The auxiliary ground plane was positioned such to closely duplicate the boundary layer thickness present during the large scale tests (Appendix B), and featured a manually operated sliding trap door which, as in the fixed ground plane, provided a well defined test start point.

Servo positioned exhaust gas probe. - A servo operated probe was used to measure the temperature and pressure distribution in each of the exhaust jets of the NASA model. The device consisted of total pressure and total temperature probes connected to a hydraulic cylinder. An electrical potentiometer and servo valve system were used to remotely control the probe position with respect to the exhaust nozzle.

INSTRUMENTATION

In general, the instrumentation consisted of 30 gage (AWG) bare bead iron-constantan thermocouples to measure inlet and field temperature time histories, and pressure and temperature probes to monitor internal model flow conditions. To simplify data reduction an electrical circuit was connected to the inlet thermocouple

circuits such that the inlet thermocouples could be electrically averaged to provide a representative value of inlet temperature rise for selected inlets. Most of the internal model flow data were visually recorded from manometer banks, point recorders, or gages. Oscillographs were employed to collect permanent time histories of all the inlet and field temperature data, the wind conditions, and selected test condition pressures.

The relative wind speed was monitored by means of the hot wire anemometer and recorded as a time history on an oscillograph. In addition, the average relative wind speed for each test run was measured by means of a hand held rotary arm anemometer.

## Pod (circ) and Dual (circ) Models

The Pod and Dual (circ) model instrumentation locations are indicated in Reference 2. Figures 6, 7, and 8 redefine the inlet and field thermocouple locations as well as thermocouple identification numbers. The inlet thermocouples were located just inside the wooden bellmouth inlets to measure temperatures which are considered to be representative of those present at the first compressor stage in a full scale jet engine. The bare bead thermocouple junctions were formed by using a capacitance welder and trimming the excess to a resulting bead size radius of approximately 0.015 in.

Figure 6 shows the five thermocouples located in each of the three inlets of Engine No. 1 of the Pod (circ) model, as well as the thermocouples positioned on the axis of each of the six inlet supply tubes. Figure 7 locates the eleven thermocouples in each of the inlets of the Dual (circ) model. Each of these were electrically averaged as were the five thermocouples in inlets A and B of the Pod (circ) model.

Five additional thermocouples were located in the field above the models as shown in Figure 8. The tabulation included in Figure 8 indicates the variations in the relative distances between the thermocouples and the engine inlets resulting from changes in EDA. These data were recorded on an oscillograph and were used in analyzing the recirculation flow paths.

## Scaled NASA Model

The location of temperature and pressure probes used to determine the internal flow characteristics of both configurations of the scaled NASA model is shown in Figure 9. It is noted that only one burner can was used and that the probes used to monitor the internal flow characteristics of the Pod (circ) and Dual (circ) models remained operational.

The exhaust gas total temperature was sensed in the exhaust line to nozzle No. 3 and recorded on an oscillograph to provide continuous monitoring of exhaust conditions. Total and static pressures were measured in each of the inlet and exhaust lines to insure equal flows to each engine. The total and static pressures in the inlet and exit lines of Engine No. 1 (assumed representative of all engines) were transduced and permanently recorded along with the total pressure at the burner can.

Figures 10 and 11 show the locations of the inlet thermocouples for the top inlet and forward facing side inlet configurations respectively. The inlet thermocouples were positioned at the same locations as those in Reference 3, and the five thermocouples in inlet 1 and 4 of the top inlet configuration were electrically averaged to assist in data analysis. Similarly, the eight thermocouples in each of the forward facing side inlets were electrically averaged.

Figure 12 shows the locations of field thermocouples used with the NASA model configurations. Four thermocouples were mounted on the right wing (3 on the underside of the wing root and 1 at the tip) to assist in determining near field recirculation paths. Five additional thermocouples were located just outside the fuselage skin in the region between the four exhaust nozzles to measure temperatures in the upward flowing "fountain" of exhaust gases caused by the mutual impingement of the four exhaust plumes.

# TESTS AND TEST TECHNIQUES

All tests were conducted outdoors at the Jet Impingement Test Facility during times of day when the random wind speeds were less than 5 fps. The majority of data was collected when the random wind speeds were less than 2 fps. Many runs were made to check the model exhaust and internal flow characteristics, to assess the effect of random wind, and to calibrate instrumentation and the various special apparatus. The results of these tests are presented in Appendices B, C, D, and E.

The test objectives were to determine the effect of wind speed and direction on ITR and the recirculation flow paths for variations in $S/S_j$, EDA, $\alpha$, and $h/D_e$. The scaled NASA model was used to determine ITR scale effects as well as the effect of wind on ITR and the flow field for variations in $S/S_j$, $h/D_e$, and inlet location.

The test procedure, which was essentially the same for all models is outlined below:

(1)    The random wind speed was measured. Most of the tests were conducted during the early morning hours to take advantage of the calm wind conditions. The wind speeds were generally from zero to 2 fps and no tests were conducted when they exceeded 5 fps.

(2)    The trap door was opened and the simulated engines started.

(3)    After two to three minutes, which was the time required to establish the desired exhaust conditions and to heat the hardware to steady state, the steam ejector was turned on and adjusted to give the desired inlet mass flow.

(4)    The wind machine was started and throttled to the desired nominal wind speed which was measured by a hand held rotary arm anemometer.

(5)    A check was made of the test conditions.

(6)    On signal, one of the test operators turned on the oscillographs, and the trap door was closed one to three seconds later (test start).

(7)    After 16 to 20 seconds, the trap door was opened (end of test) and one to three seconds later the oscillographs were turned off.

(8)    The inlet and exhaust pressure data were read from manometers and manually recorded.

(9)    When required, the smoke gun was activated and photographs taken before either returning to step (4) for the next run or shutting down the test stand.

(10)    Visual observations (tufts and smoke) and any unusual occurrences were logged.

# RESULTS AND DISCUSSION

The results presented herein provide information on the effect of wind on ITR and the recirculating flow field as well as an assessment of the effect of model scale on measured values of ITR. The results are based on values of ITR and $\triangle$T calculated from temperatures measured after steady state conditions had been achieved.

## Presentation of Results

During the course of this program, observations and measurements were made which led to results of general interest. These, even though important, are presented in the Appendices B, C, and D in order to maintain simplicity and conciseness in the body of this report. Reference is made to these results at pertinent places in the text.

The Pod (circ) and Dual (circ) Model test results are discussed first. The effect of wind on the recirculating flow field is followed by a discussion of the effect of wind on ITR. These results should be considered as extensions to the Reference 2 results.

The scaled NASA model test results are discussed next. A discussion of the recirculating flow field is followed by one concerning wind and scale effects on ITR. In addition to assessing scale effects, these results are an extension to Reference 3.

The results are presented in the following figures:

## Pod (circ) and Dual (circ) Models

Flow field. - The various elements of the flow field for the Dual (circ) Model which have been described in detail in reference 2 are illustrated in Figure 13. Observations made during this present study are discussed in this section to provide more insight into the effects of wind on these elements and to lend a better understanding to the ITR data which follows.

The reinforced ground jets (item c in Figure 13) strongly influence ITR. Figure 14 schematically illustrates how the wind peels these reinforced ground jets from the ground plane and directs the hot gases back toward the model. By observation of the smoke flow pattern, the turning radius (r) of the peeled jet and hence the height of the peeled exhaust gas above the ground board was found to be an inverse function of the wind speed. Also noted was, that at sufficiently high wind speeds, this radius of turn was small enough to allow entrainment of the peeled gases in the ground jet and cause the formation of an eddy at the peeling point. Although the peeling point Radius (R) for the dual (circ) model was found to vary inversely with wind speed it was relatively independent of wind direction ($\theta$). See Figure 15. Extrapolation to zero speed agrees well with the data presented in Reference 2. It can be seen (Figure 15) that the peeling point was relatively close to the pod (circ) model and was independent of $V_\infty$. This variance between the pod and dual models suggests that exhaust arrangement has a large effect on the distance from the model at which peeling will occur.

The effect of wind azimuth ($\theta$) on the direction of the peeled exhaust gases subsequent to peeling was clearly evident from smoke observations. For the case of $\theta = -30°$ or $-60°$, the exhaust gases peeled from the reinforced ground jet were blown toward the downstream engine inlet. This effect was visible for both models but was more pronounced for the dual (circ) model. The distribution of temperatures in the field 6 inches above the model are shown in Figure 16. The temperatures directly above the inlets are essentially equal to the ITR values at each inlet. The field temperatures respond to wind direction in the same fashion as ITR.

The phenomenon of fountain instability (first observed in Reference 2) was observed for the wing off case of the dual (circ) model. Smoke injected into the region approximately 6 inches above the inlet plane was seen to be drawn by each inlet alternately in a random fluctuating manner. Figure 17 is a tracing of the electrical average channels from oscillograph records and clearly describes this phenomenon. This data is for the dual (circ) model, wing off, $h/d_e = 2$, $V_\infty = 11$ ft/sec, and $\theta = 0°$. It can be seen that one or the other engines experiences excessive levels of ITR even though the other engine ITR may be relatively low. This problem should be considered by the designer whenever engine inlet placement does not provide the benefit of blockage by the wing or other aircraft surfaces. In addition, Figure 17 reveals that the average of the ITR for Engine No. 1 and No. 2 is approximately the same whether the engines are experiencing different or the same levels of ingestion. This fact is used in the

analysis of data which is characterized by fountain instability. The random fluctuations and very short duration of equal ITR is easily understood when it is realized how critical the balance between $V_\infty$ , $\theta$, and ground jet velocity (not to mention outside influences such as random wind) must be to maintain stability (flow symmetry) in the region between the two engines.

   Wind Effects, Pod (circ) Model. - Levels of ingestion resulting from variations of $V_\infty$ , $h/D_e$, EDA, $\alpha$, and $\theta$ are shown in Figures 18 through 22 for the pod (circ) model with the $S/S_j$ = 100 wing in place. Each figure is divided into four blocks of information. The three blocks showing the ITR for inlets A, B, and C of both engines No. 1 and No. 2 are based on inlet tube temperatures which were shown to be representative of the inlet temperatures (Appendix B). The block showing a comparison between inlets A and B of Engine No. 1 are based on electrically averaged values.

   Wind speed and direction: ITR increases with wind speed to a peak value of 70°F at approximately 30 ft/sec and then decreases. See Figure 18. The upstream inlets experience the highest ITR. ITR decreases as $\theta$ increases. The downstream engine which is in the path of the recirculating hot gases because of the distortion of the major reinforced ground jet and attendant peeling, experiences the highest ITR for $\theta$ = -30° and -60°. Figure 19 presents the variation of ITR with wind direction at wind speeds which result in maximum ITR for exhaust deflection angles of 0°, 10°, and 20°. ITR decreases with increasing $\theta$ and increasing EDA.

   Model height: Figure 20 shows the variation of ITR with height above the ground plane for exhaust deflection angles of 0°, 10°, and 20°. These data are for the wind speed which resulted in maximum ITR so that the worst condition might be examined. A maximum ITR of 107°F was measured at $h/D_e$ = 1 at EDA = 0°. ITR in general decreases with height. However, this trend is modified for EDA = 10° in that ITR increases to a peak value at $h/D_e \approx$ 3 and then decreases.

   EDA and angle of attack: Figures 20 and 21 show that ITR reduces with EDA to nearly zero at EDA = 20°, and Figure 22 shows that positive angles of attack have a relatively small effect on ITR for wind speeds which result in maximum ITR at $\theta$ = 0°. For $\theta$ = -30°, ITR increases to a maximum value at $\alpha$ = 5° and decreases for $\alpha > 5$°.

   Inlet temperature distribution: The temperature distribution along the length of the engine pods is shown in Figure 23 for wind directions of 0° and -30° at wind speeds which result in maximum ITR. The upstream inlets and the downstream engine experience the greatest ITR. Temperature variations up to 25°F exist at the inlet face of each inlet. It is seen that the electrical average and inlet tube thermocouples (Figure 6) give a good representation of the average ITR at each inlet (see Appendix B). The field temperatures 6 inches above inlet B of both engines are only slightly lower than the average ITR at those inlets, indicating the presence of relatively high temperature gases in a region above the model. These data, along with visual observations, substantiate the downward flowing mass of air which was depicted above the model in Figure 13.

Wind Effects, Dual (circ) Model. - The effects of wind, height, exhaust deflection angle, angle of attack and wing on ITR (based on electrical average) are presented in Figures 24 through 27 for both engines of the Dual (circ) Model. The data at the top of all these figures depict the wing off case, while the data at the bottom present ITR for the wing on case $(S/S_j = 1.00)$. The effect of wind direction ($\theta$) is also shown.

Since the relatively large scatter of the wing off data was the result of fountain instability (see discussion in previous section and Figure 17), curves were faired through the $\theta = 0°$ wing off data points by averaging the engine 1 and engine 2 results. The presence of a wing effectively suppresses the effects of fountain instability on ITR and the repeatability of results is greatly improved. See Appendix B.

Wind speed and direction, wing on: As shown in Figure 24, ITR generally increases with wind speed to a maximum value at 30 fps ($\theta = 0°$) and then decreases. The wind speed at which maximum ITR occurs reduces with increasing wind direction angle. ITR decreases with increasing $\theta$ and the downstream engine experiences the highest ingestion. The modification of Reference 2 data shown on Figure 24 indicates an average ITR value of engine No. 1 and No. 2 instead of the published maximum value.

Model height: A general reduction in ITR with increasing height is indicated from the data in Figure 25.

EDA and angle of attack: In the presence of a wing the maximum ITR is reduced by deflecting the exhausts outboard as indicated in Figure 26. The greatest ITR reduction resulting from EDA is achieved at $\theta = 0°$ and as expected, there is no appreciable difference in ITR between engines 1 and 2. When no wing is present, ITR is relatively independent of EDA for both engines at $\theta = 0°$ and for the upstream engine when $\theta = -30°$ and $-60°$. EDA results in an ITR decrease for engine No. 2 at $\theta = -30°$ and $-60°$. Positive angles of attack up to 10 degrees have only a relatively small effect on ITR as evidenced by the data in Figure 27.

Wing effect: The presence of a wing generally results in reduced ITR except for winds greater than 20 fps at $\theta = 0°$. See Figures 24 through 27. At $\theta = 0°$, the maximum ITR is about 40°F at $V_\infty$ about 30 fps. See Figure 23.

### Scaled NASA Model

Flow field. - A scaled representation of the effect of wind on the flow field about the NASA model based on smoke and tuft observations and temperature data is presented in Figure 28. The flow field is characterized by four mutually perpendicular reinforced ground jets formed by the mutual interaction of the four exhausts with the ground plane, and by ground jet peeling and the formation of two trapped vortices or "eddies"; one at the peeling point of the ground jet (i) and the other under the wing (j). The smoke flow pattern photographs in Figure 29 show several examples of ground jet peeling and the presence of eddy "i" and "j". Eddy "i" is similar to that encountered with the Pod and

Dual (circ) models. See Figure 14. The approximate distance (R) of the peeling line from the center of the exhaust pattern was determined from smoke observations and is presented in Figure 30 as a function of wind speed and direction. It is noted in passing that for all wind speeds and direction the auxiliary ground board was large enough to accommodate the peeling point and that the peeling point was always located upstream of the exhaust impingement points.

Smoke issued from a position above the model (top inlet configuration) during wind off conditions was observed flowing downward and being entrained by the exhaust jets. Tufts on the upper surface of the wing were also pulled by the entraining action of the jet exhaust except in the immediate vicinity of the inlets. The entrainment strength of the exhaust became less pronounced with increasing model height above the ground. At moderate heights ($h/D_e = 3$), the increasing influence of the inlet sink was evident as shown in Figure 31 where it can be seen that even those wool tufts placed at the leading edges and tips of the wing are pulled by the inlets. Although not presented herein, at an $h/D_e$ of 5, even more influence was seen to be exerted on the tufts by the inlets.

At low to moderate wind speeds ($15 < V_\infty < 30$), the relatively high temperature gases of the reinforced ground jet were found to peel at sufficient distance from the model (R) such that the wing did not serve to trap or channel the peeled gases. See Figure 32. Here, the peeled gases of the reinforced ground jet were forced to flow back toward the model and were ingested by the inlets and entrained by the exhaust jets. It was also observed that at these speeds the inlet sinks controlled the behavior of the tufts on the upper surface of the wing. At speed in excess of 30 fps the predominance of the inlet sink effect decreased and the influence of the free stream controlled the recirculation patterns over the top of the wing. The tuft photographs in Figure 33 illustrate this change in the flow pattern over the wing for wind speeds greater than 30 fps. The ground jet gases were peeled in a tight radius (r) and subsequently entrained by the exhaust jets for $V_\infty > 30$ fps. These photographs illustrate why ITR decreased for wind speeds in excess of approximately 30 fps. These flow field characteristics suggest that the ground jet is blown back under the model for those higher wind speeds which result in formation of eddies such as "i" in Figure 28.

Additional information on the behavior of the flow field was obtained from temperatures measured near the under-surfaces of the wing and fuselage. These data provided insight into regions of the flow field where high jet velocities precluded the use of smoke visualization techniques.

The variation with wind speed of temperatures measured near the fuselage under-surface in the vicinity of the "fountain" is shown in Figure 34. The temperatures have been nondimensionalized to the actual exhaust gas temperature ($T_j \approx 1200°F$). The fountain temperatures are excessive and should be considered when selecting fuselage skin material in design of Jet V/STOL. These data also show that inlet location and wing size have a negligible effect on fountain temperature, but that wind speed, direction and exhaust arrangement are important. At $h/D_e = 3$, fountain temperatures gradually

decrease with increasing wind speeds for $\theta = 0°$ and $90°$. A rapid reduction in fountain temperatures occurs for $V_\infty > 25$ fps at $\theta = 45°$. These data further confirm the deduction that the hot exhaust gases in the ground jets are blown back under the model when the energy of the ground jet and $V_\infty$ are such as to promote peeling and the formation of eddy "i". See Figure 28.

The variation of fuselage undersurface temperatures with $h/D_e$ is shown in Figure 35 for zero wind conditions. It is seen that the effect of the fountain on the fuselage reduces rapidly with $h/D_e$. At $h/D_e = 5$, the fountain gases no longer heat the bottom of the fuselage, which suggests that the fountain energy has been nearly dissipated at this height. Figure 35 also indicates that inlet location and wing size do not influence the fountain for all model heights tested.

Figure 36 shows that the temperature of the air underneath the wing varies with wind speed and direction in the same fashion as did the fuselage temperatures. This can be explained by the fact that the ground jet is peeled from the ground plane and hot exhaust gases are blown back under the model (even beneath the level of the wing undersurface). The fact that these temperatures are so high (the order of $300°F$ above ambient) indicates that hot fountain gases are being trapped under the wing. The observance of the eddy "j" and tuft pictures (Figures 28 and 31), and the low wing tip temperature indicate that the hot fountain gases did not flow outboard but were rather redirected in the vicinity of the root chord. These fountain gases were then entrained by the general recirculation patterns about the model. The decay of the wing temperatures to essentially zero at $h/D_e = 5$ (Figure 37) indicate that fountain heating effects become minimal at $h/D_e \approx 5$, and infer that the aerodynamic influences of the fountain can be expected to become small for $h/D_e > 5$.

Wind and scale effects. - Large and small scale ITR is presented in Figures 38 through 41 versus wind speed for both the top inlet and side inlet configurations. Included are the effects of ground height ($h/D_e$), wing size ($S/S_j$) and wind direction ($\theta$). The small scale ITR values were calculated from measurements made after steady state conditions were achieved, and represent the average ITR at each inlet. Electrical average values were used for inlets 1 and 4 of the top inlet configuration. Data points and curves from preliminary NASA, Langley large scale test results are superimposed to show comparison between large and small scale test results. Account is made for the fact that the large scale ITR data was obtained for variations in wind direction $\psi$ (Reference 3), where $\theta = -\psi$. The reader is cautioned to consider the inlet numbering scheme and remember that $\theta = -\psi$ when comparing the data presented herein with that in Reference 3.

Wind velocity: The small scale test results indicate a general increase in ITR with increasing headwinds to a peak value at between 20 and 40 fps for the top inlets and from 10 to 30 fps for the side inlets. ITR decreases for further increase in headwinds. This can be explained by the fact that the peeled ground jets are blown back under the model (not near the inlets) for wind speeds greater than approximately 30 fps.

Due to the rectangular quadrate exhaust arrangement and the resulting summetrical reinforced ground flow jets, the ITR at $0 = 0°$ is generally not significantly different than the ITR at $\theta = 90°$ for the top inlets configuration. This, surprisingly enough was also observed for the side inlets at $h/D_e = 1.6$. At greater heights ($h/D_e = 3$ and $5$) the expected result, i.e. ITR at $\theta = 0°$ is greater than ITR at $\theta = 90°$ was observed for the side inlet configuration.

The upstream inlets of the top inlet configuration ingested hotter gases than the downstream inlets, i.e., inlets 1 and 2 had the highest ITR for headwinds ($\theta = 0$), inlet 2 had the highest ITR when $\theta = 45°$, and inlets 2 and 4 had the highest ITR when $\theta = 90°$.

Wing Area: Comparing the small scale test results in Figure 38 with those in Figure 39 shows that for top inlets at $h/D_e = 3$ increased wing area resulted in reduced ITR at $\theta = 0°$, while wing area had essentially no effect on ITR at $\theta = 45°$ and $90°$. For the side inlet configuration, both the large and small scale test results shown in Figure 40 indicate that wing size had no significant effect on ITR for all conditions of wind speed, direction and $h/D_e$.

Model height: The small scale test results in Figures 38 and 40 indicate that the effect of $h/D_e$ on ITR changes with increasing wind speed. For top inlets and zero winds the intermediate height ($h/D_e = 3$) generally results in the highest ITR and $h/D_e = 5$ results in the lowest ITR at every inlet. This trend of ITR with $h/D_e$ is maintained for headwinds up to approximately 30 fps. At higher wind speeds ITR varies inversely with $h/D_e$. These same observations may be made of the large scale ITR results, and not withstanding the limited range of wind speeds tested, may also be generally made (both large and small scale) of the $\theta = 45°$ and $\theta = 90°$ wind direction cases.

For side inlets and zero wind speeds, ITR varies inversely with $h/D_e$. This trend of ITR with $h/D_e$ is maintained with very few exceptions for all wind speeds and directions for both wing sizes ($S/S_j = 43$ and $86$) and for both large scale and small scale test results. This result for the side inlet configuration was expected because the inlets were located near the high temperature reinforced ground jet and were unprotected by any wing surface.

Scale effects: ITR scale effects have been obtained by comparing large and small scale data. The data were examined for similarity in trends and general conclusions and then were analyzed in more detail to determine a scale factor. These comparisons are discussed in the following.

Large and small scale ITR is presented versus wind speed in Figures 38 through 41 for various wind directions and model heights. It can be seen that trends of ITR with $V_\infty$, $\theta$, $h/D_e$, $S/S_j$ and inlet location are generally the same for large and small scale. In those instances where small scale trends apparently differ from large scale (generally $\theta = 45°$ and $90°$), an insufficient amount of large scale data was available for comparison.

19

It is important to mention that four of the five pertinent conclusions published in Reference 3 were reached by independently examining the small scale results. The exception, which is of little consequence to the designer, was that full scale tests indicated that "with headwinds greater than about 30 knots (50 fps) the hot-gas ingestion was virtually eliminated". The small scale data indicated that relatively significant (however less than the maximum) levels of ingestion (40°F) persisted in some cases at these high wind speeds.

Especially good agreement in ITR magnitude was found most often for tests at $h/D_e$ = 3 and 5, and for wind speeds up to 30 fps . See Figures 38 through 41. The agreement for the side inlet configuration was generally better than the top inlet configuration, and for both configurations the large wing($S/S_j$ = 86) resulted in better agreement than the small wing.

A summary of comparisons between large and small scale data is presented in Table I. Here the comparative agreement is presented in qualitative terms; excellent (E), good (G), fair (F), and poor (P), and reflect ITR agreements within 20°F over 1/3, 2/3, and the entire wind speed range. If the absolute difference between large and small scale ITR is greater than 20°F, the agreement is marked poor. To further illustrate the generally good agreement between large and small scale ITR results, the average ITR values (arithmetic average of ITR at each inlet) are presented in Figures 42 and 43 for both configurations and both wing sizes. This method of comparison provides a measure of total configuration ITR scale effects. Generally good agreement exists for headwinds up to approximately 30 fps especially for $h/D_e$ = 3 and 5.

Because large and small scale data describe similar trends, conclusions, ITR magnitude, and configuration effects, it may be concluded that small scale data may be used by the V/STOL aircraft designer to assess gross design effects due to configuration, $h/D_e$, $V_\infty$, $\theta$, and $S/S_j$.

To assist in determining a small scale ITR scale factor, samples of both sets of data were first reduced to a comparable basis for comparison. The basis used was the velocity parameter $\left[ \frac{\rho_\infty}{\rho_j} \left( \frac{V_\infty}{V_j} \right)^2 \right]^{1/2}$ rather than $V_\infty$ , which was necessary to account for the fact that the large scale exhaust conditions were dependent on ITR because an actual jet engine was used and thus a "closed loop" test condition existed. As a result, the large scale ITR data was collected at changing jet exhaust conditions (jet velocity and temperature). The velocity parameter improved the agreement between the large and small scale data over the range of velocities tested, however the improvement was slight, and deemed to be within the "noise level" of the combined test results. Therefore, the empirical correlations presented herein were based on $V_\infty$ rather than the more precise velocity parameter.

Large scale ITR was plotted versus small scale ITR. Due to the many interdependent variables ($V_\infty$ , $h/D_e$, $\theta$ , $S/S_j$ and configuration) many plots were required where one, two or three variables were held fixed while the others were allowed to vary.

The ITR data did not neatly collapse on a one to one correlation line, and an example of the only significant trends which resulted is shown in Figure 44, where configuration, wind direction and wing size are held constant while wind speed and model height are allowed to vary. Second order curves were faired through the data points (note that the accuracy of the combined large and small scale data is approximately $\pm 10°F$) and it can be seen that for levels of ingestion within practical design limits (ITR $<40°F$) the small scale ITR scale factor for top inlets is approximately 1.0 for $20 < V_\infty < 35$ fps, greater than 1.0 for $V_\infty < 20$ fps and less than 1.0 for $V_\infty > 35$ fps for side inlets, the scale factor is approximately 1.0 for $V_\infty < 30$ fps and less than 1.0 for $V_\infty > 30$ fps.

It is difficult, at this time, to rationalize the observed variation of scale factor with wind speed, however, since the highest levels of ingestion occurred at $10 < V_\infty < 30$ where the scale factor is nearly one it may be concluded that small scale test data may be used to directly predict full scale ingestion for the purpose of assessing gross effects for design.

# CONCLUSIONS

Small scale hot gas recirculation studies conducted at the Bell Aerosystems Jet Impingement Test Facility have indicated the following conclusions:

1.  The hot exhaust gases are redirected by ground winds and the reinforced ground jets have a predominant influence on ingestion for ground winds up to 30 fps.

        a.  For top inlet configurations, hot gases drawn from the field above the model contribute to ITR.

        b.  For wind speeds in excess of approximately 30 fps most of the hot exhaust gases are blown back underneath the model and result in reduced ITR.

        c.  Inlets located upstream to the relative wind experience the highest ingestion.

2.  The effect of fountain instability on ITR is generally suppressed by ground winds, except when a reinforced ground jet propogates directly into the wind.

        a.  The effect of fountain instability on ITR is effectively damped by the presence of a wing.

        b.  Fountain effects (especially fuselage surface heating) become small at a model height of approximately 5 equivalent diameters.

        c.  Fountain characteristics are determined by exhaust arrangement, and are independent of wing size and inlet location.

3.  Geometric variations such as increased height above ground, increased wing area, proper inlet location and exhaust arrangement, increased outward exhaust deflection and proper wind heading all result in reduced levels of ITR.

4.  Small scale ITR data based on full scale exhaust conditions may be used to assess full scale ITR trends due to configuration, $h/D_e$, $V_\infty$, $\theta$, and $S/S_j$ and the results may be used to assess gross design effects.

5.  For levels of ingestion within practical design limits (ITR $< 40°F$) the small scale ITR scale factor for top inlets is approximately 1.0 for $20 < V_\infty < 35$ fps, greater than 1.0 for $V_\infty < 20$ fps and less than 1.0 for $V_\infty > 35$ fps for side inlets, the scale factor is approximately 1.0 for $V_\infty < 30$ fps and less than 1.0 for $V_\infty > 30$ fps.

TABLE I

COMPARISON OF LARGE AND SMALL SCALE ITR DATA

| TOP INLET CONFIGURATION | | | | | | | |
|---|---|---|---|---|---|---|---|
| FIGURE NO. | $S/S_j$ | $h/D_e$ | $\theta$ DEG | COMPARISON RATING | | | |
| | | | | INLET NUMBER | | | |
| | | | | 1 | 2 | 3 | 4 |
| 38 (a) | 43 | 1.2 | 0 | F | P | F | G |
| 38 (b) | 43 | 1.2 | 45 | F | P | P | P |
| 38 (c) | 43 | 1.2 | 90 | F | P | F | F |
| 38 (a) | 43 | 3 | 0 | P | G | E | G |
| 38 (b) | 43 | 3 | 45 | P | P | G | G |
| 38 (c) | 43 | 3 | 90 | P | F | E | E |
| 38 (a) | 43 | 5 | 0 | F | F | F | F |
| 38 (b) | 43 | 5 | 45 | P | P | E | E |
| 38 (c) | 43 | 5 | 90 | E | P | G | P |
| 39 (a) | 86 | 3 | 0 | G | G | E | E |
| 39 (b) | 86 | 3 | 45 | P | P | F | F |
| 39 (c) | 86 | 3 | 90 | F | F | F | F |

| SIDE INLET CONFIGURATION | | | | | |
|---|---|---|---|---|---|
| FIGURE NO. | $S/S_j$ | $h/D_e$ | $\theta$ DEG. | COMPARISON RATING | |
| | | | | INLET NO. | |
| | | | | 1 | 2 |
| 40 (a) | 43 | 1.6 | 0 | G | G |
| 40 (b) | 43 | 1.6 | 45 | G | P |
| 40 (c) | 43 | 1.6 | 90 | E | F |
| 40 (a) | 43 | 3 | 0 | F | F |
| 40 (b) | 43 | 3 | 45 | E | E |
| 40 (c) | 43 | 3 | 90 | F | G |
| 40 (a) | 43 | 5 | 0 | E | E |
| 40 (b) | 43 | 5 | 45 | E | E |
| 40 (c) | 43 | 5 | 90 | E | E |
| 41 (a) | 86 | 1.6 | 0 | G | P |
| 41 (b) | 86 | 1.6 | 45 | N/A | N/A |
| 41 (c) | 86 | 1.6 | 90 | F | F |

LEGEND

P - Poor
F - Fair, Within 20°F Over 1/3 $V_\infty$ Range
G - Good, Within 20°F Over 2/3 $V_\infty$ Range
E - Excellent, Within 20°F Over Entire $V_\infty$ Range
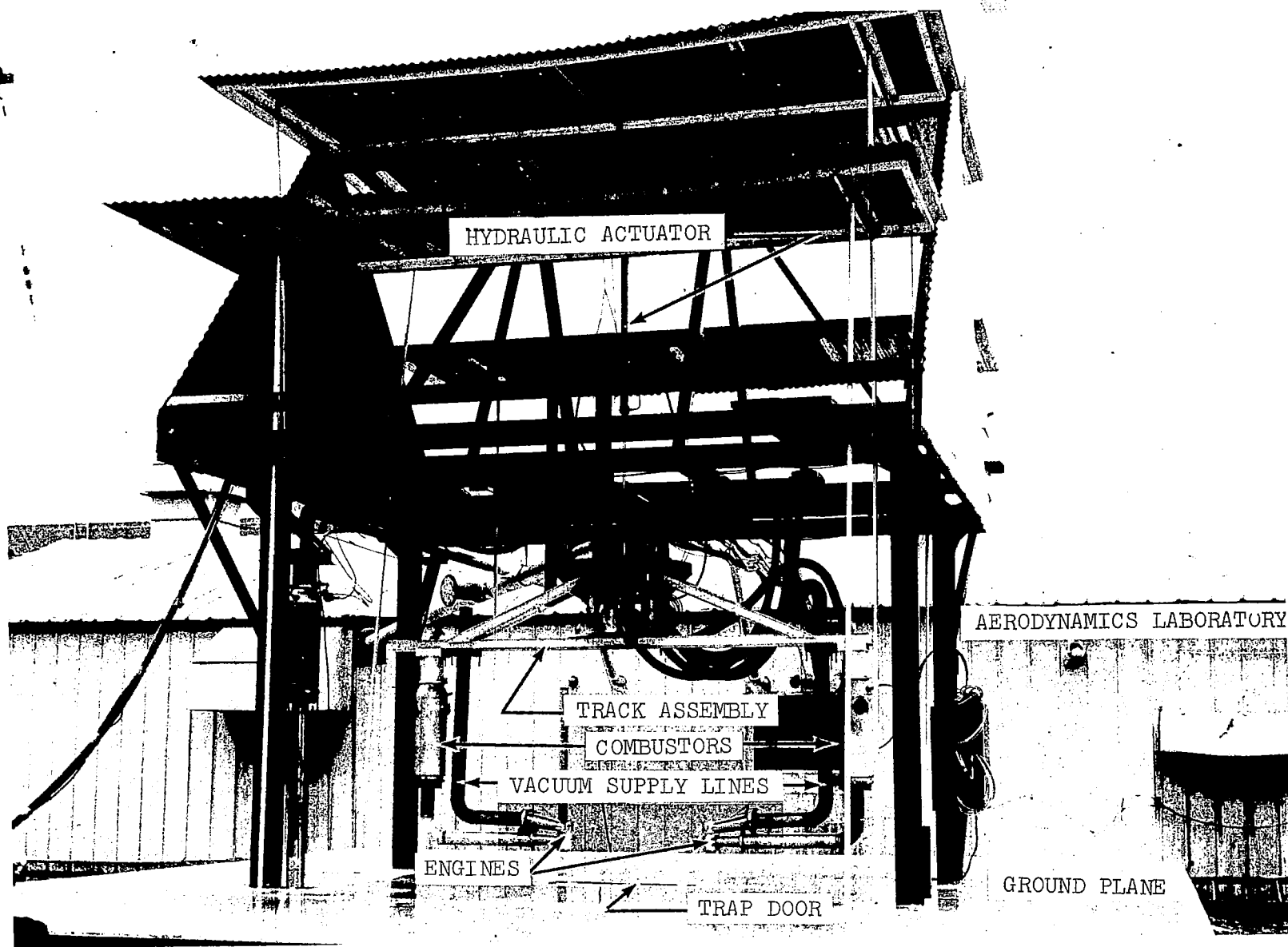
FIGURE 1. - JET IMPINGEMENT TEST FACILITY.

INLET SUCTION PIPE

SUCTION TUBES

INLET A
INLET B
INLET C

ENGINE NO. 2

ENGINE NO. 1

TAPERED EXHAUST SUPPLY TUBE

WING ($S/S_j = 30$)
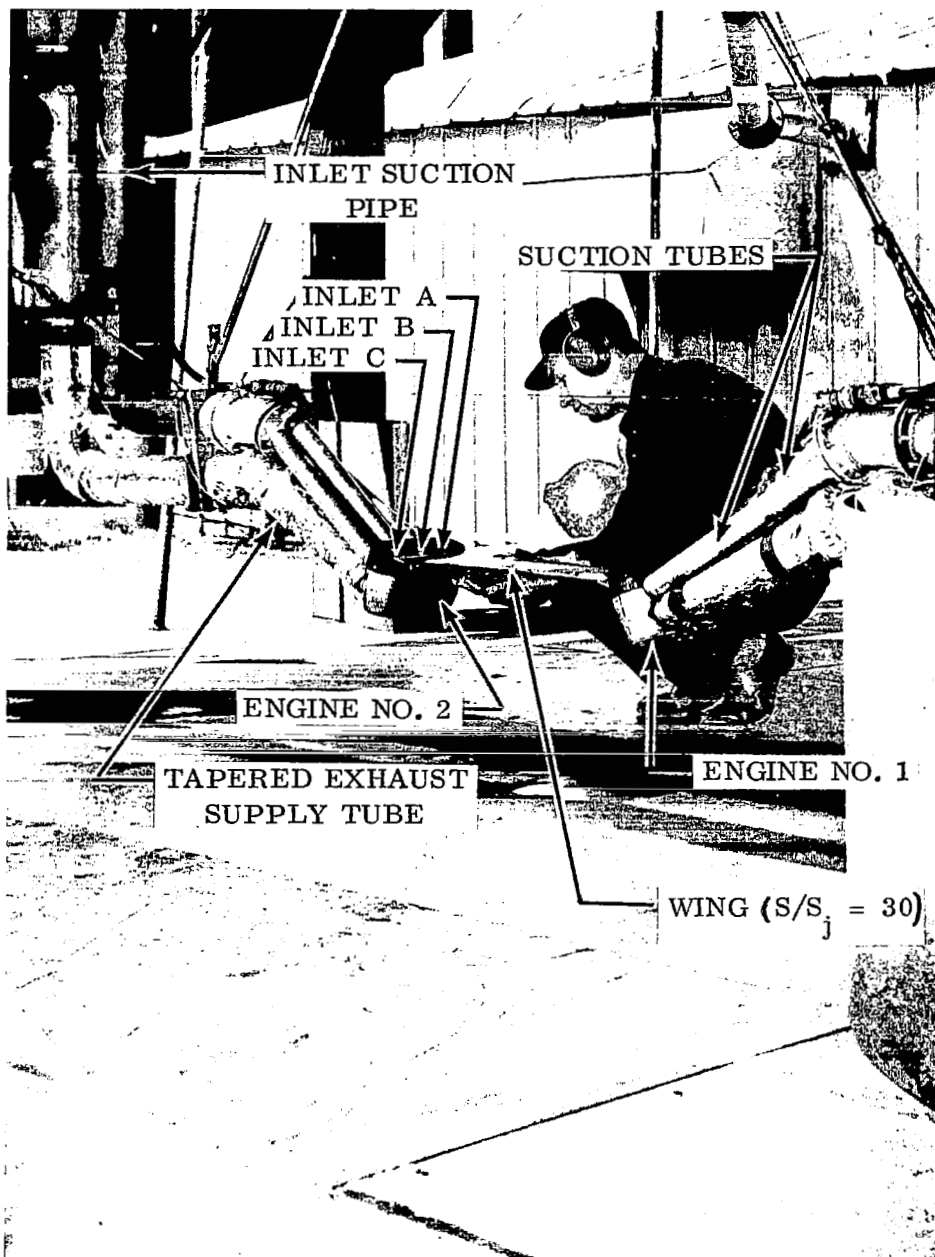
FIGURE 2. - POD (CIRC) MODEL, EDA = 20.

FLANGES

BELLMOUTH INLET

INLET CHAMBER

INSULATION

EXHAUST CHAMBER

ENGINE NO. 1

ENGINE NO. 2

TRAP DOOR
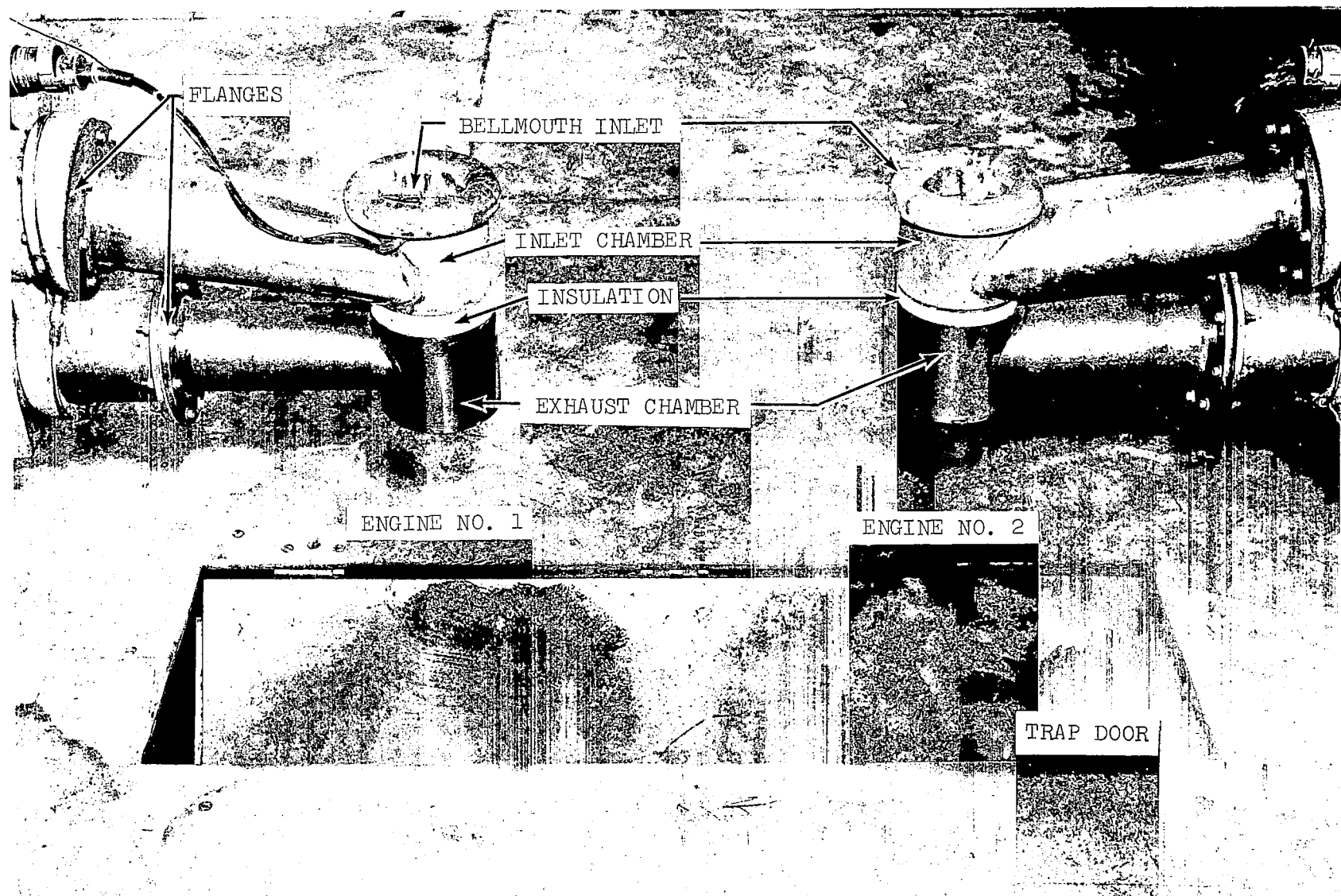
FIGURE 3. - DUAL (CIRC) MODEL, LESS COWLINGS.

AUXILIARY
GROUND
BOARD

SLIDING
TRAP
DOOR
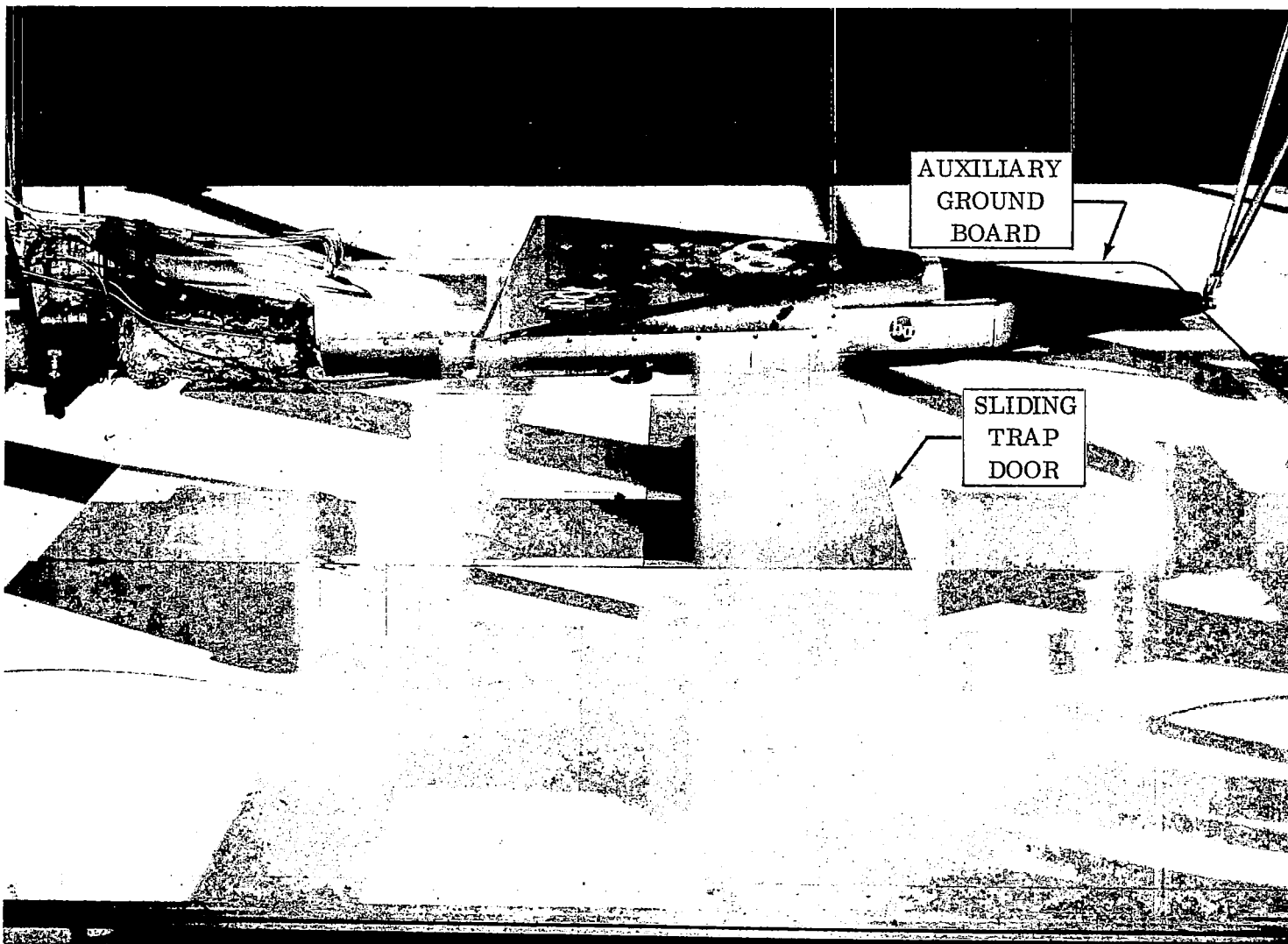
FIGURE 4. - SCALED NASA MODEL, TOP INLET CONFIGURATION
WITH AUXILIARY GROUND BOARD INSTALLED

27

_____ BELL MODEL, 4 TIMES SIZE

— — — — — NASA, LRC
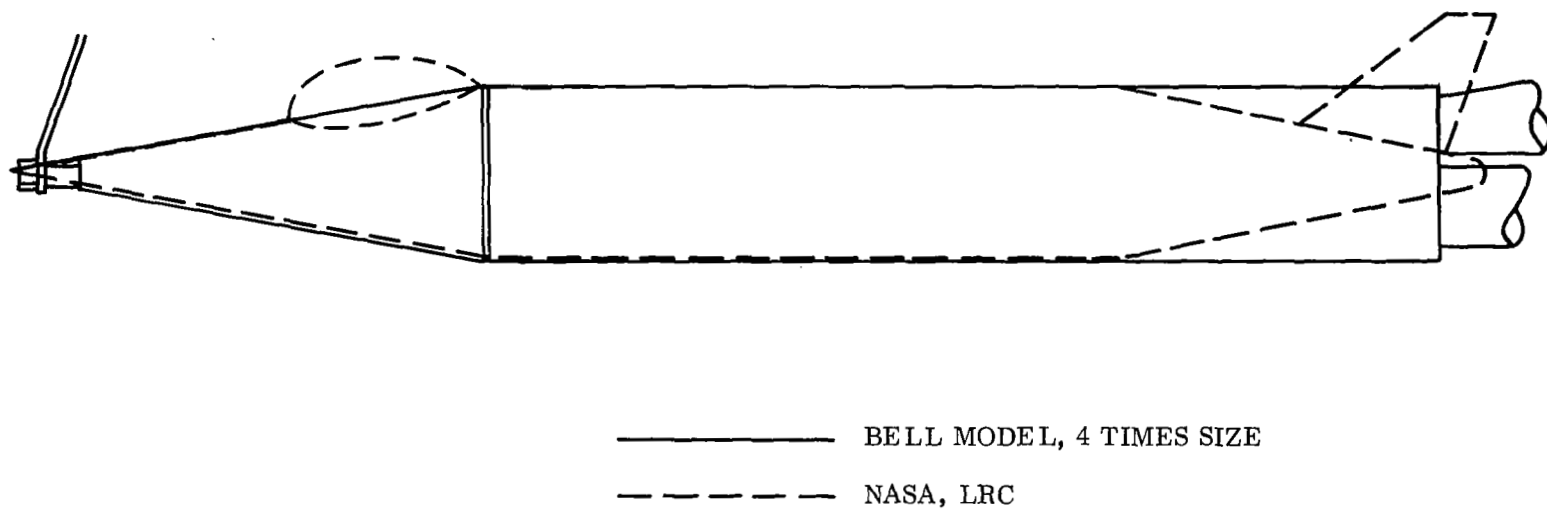
FIGURE 5. - GEOMETRIC SIMILARITY OF TEST CONFIGURATIONS.
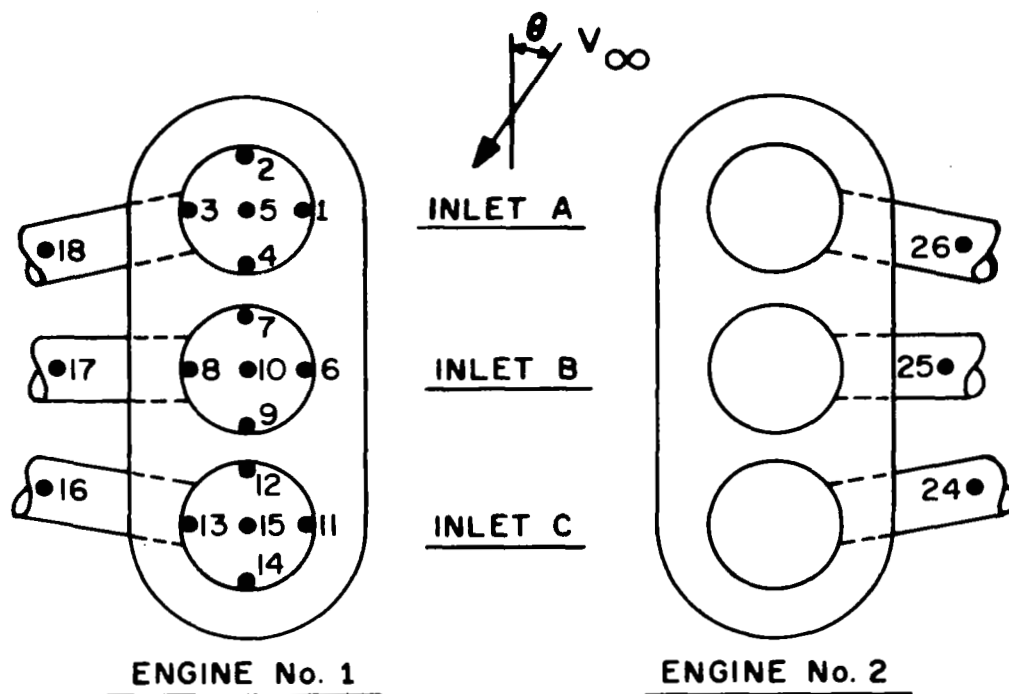
FIGURE 6. - INLET THERMOCOUPLE ARRANGEMENT, POD (CIRC) MODEL.
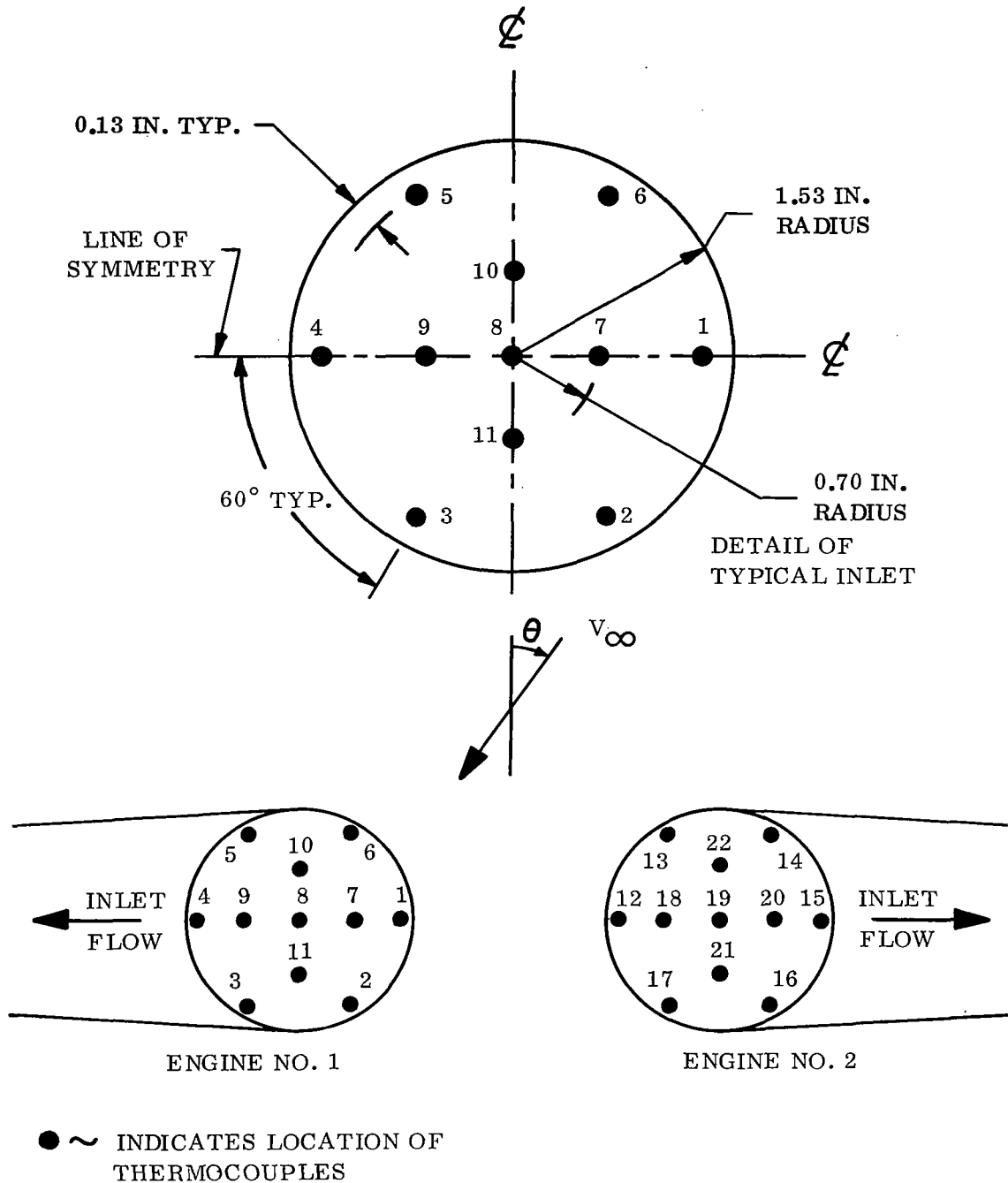
FIGURE 7. - INLET THERMOCOUPLE ARRANGEMENT, DUAL (CIRC) MODEL.

**FIELD THERMOCOUPLES**
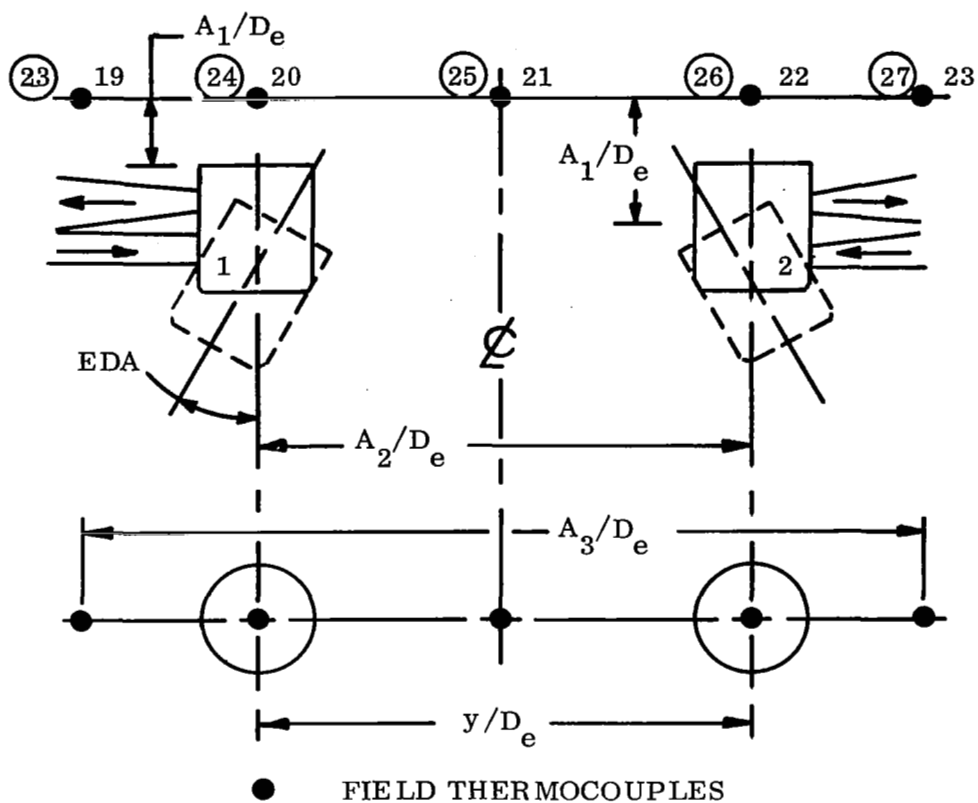
| MODEL | /EDA | 0° | 10° | 20° |
|-------|------|----|-----|-----|
| POD (CIRC.) | $A_1/D_e$<br>$A_2/D_e$<br>$A_3/D_e$ | 2.08<br>8.60<br>12.45 | 1.96<br>8.60<br>12.45 | 1.84<br>8.60<br>12.45 |
| DUAL (CIRC.) | $A_1/D_e$<br>$A_2/D_e$<br>$A_3/D_e$ | 1.44<br>10.00<br>13.85 | 1.60<br>9.50<br>13.85 | 1.28<br>9.01<br>13.85 |

$$D_e = 3.13 \text{ in.}$$

NOTE: Thermocouple Identification Numbers Are Uncircled For The Pod Model And Circled For The Dual (Circ) Model.

FIGURE 8. - FIELD THERMOCOUPLE LOCATIONS.

TOP VIEW OF
INLET SYSTEM

21 IN.

2   4
1   3

TRANSITION
SECTIONS

63 IN.

⊗ TOTAL TEMPERATURE; TOTAL AND STATIC PRESSURE
◯ TOTAL AND STATIC PRESSURE

FLANGED ATTACHMENT
TO TEST FACILITY

13 IN.

BOTTOM VIEW OF
EXHAUST SYSTEM

1   3
2   4
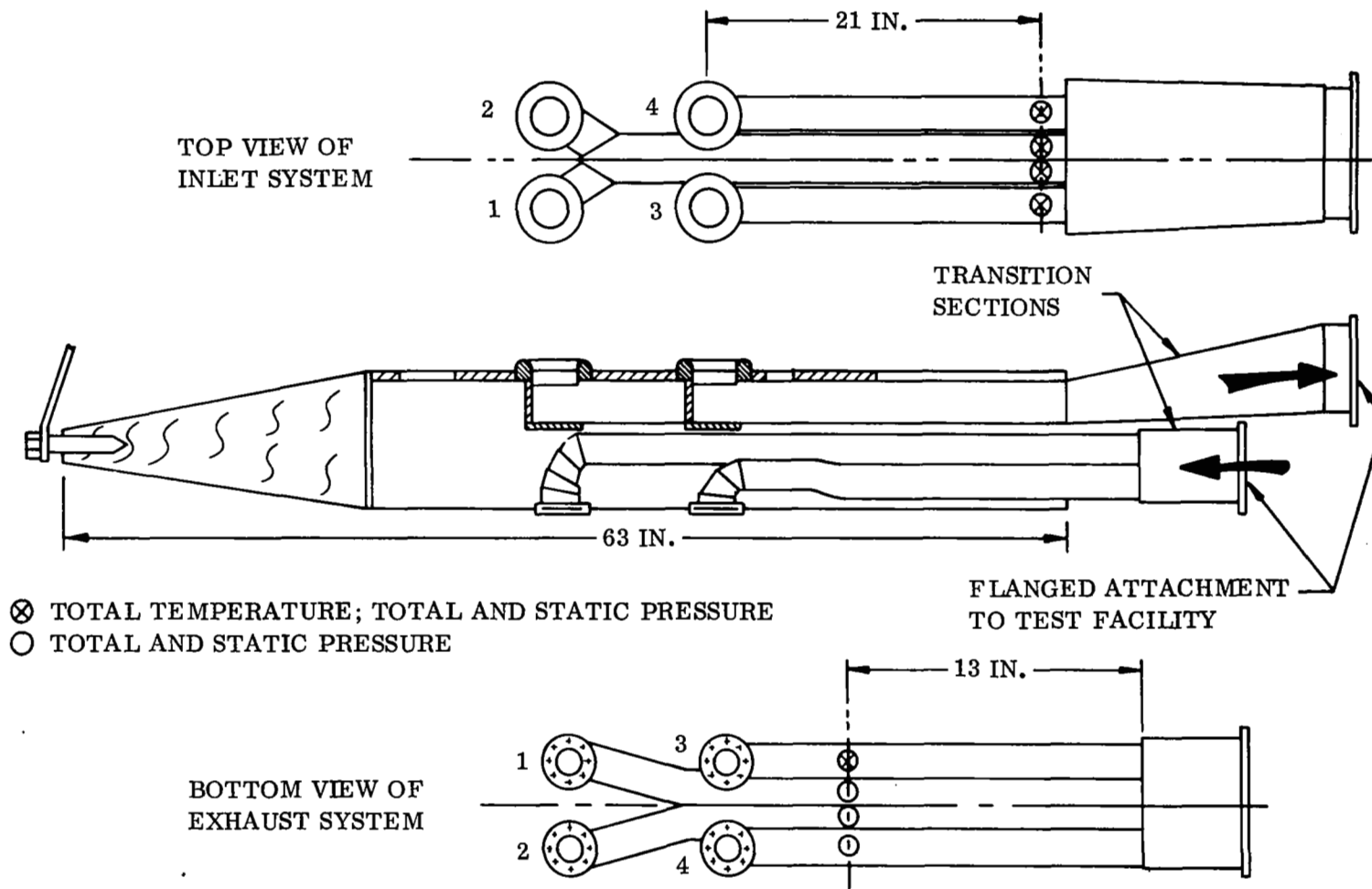
(a)  Top Inlet Configuration

FIGURE 9. - SCALED NASA MODEL INSTRUMENTATION.

INLET NO. 2 →

TOP VIEW OF
INLET SYSTEM

INLET NO. 1 →

32 IN.

TRANSITION
SECTIONS

FLANGED ATTACHMENT
TO TEST FACILITY

63 IN.

⊗  TOTAL TEMPERATURE; TOTAL AND STATIC PRESSURE
○  TOTAL AND STATIC PRESSURE

BOTTOM VIEW OF
EXHAUST SYSTEM

13 IN.

1

3

2

4

(b)  Side Inlet Configuration

FIGURE 9. - CONCLUDED.

θ V∞

S/S_j = 43

● - THERMOCOUPLE LOCATION

FORWARD

INLET DETAIL, TYPICAL

0.79 IN.
RADIUS

0.96 IN.
RADIUS

0.24 IN.
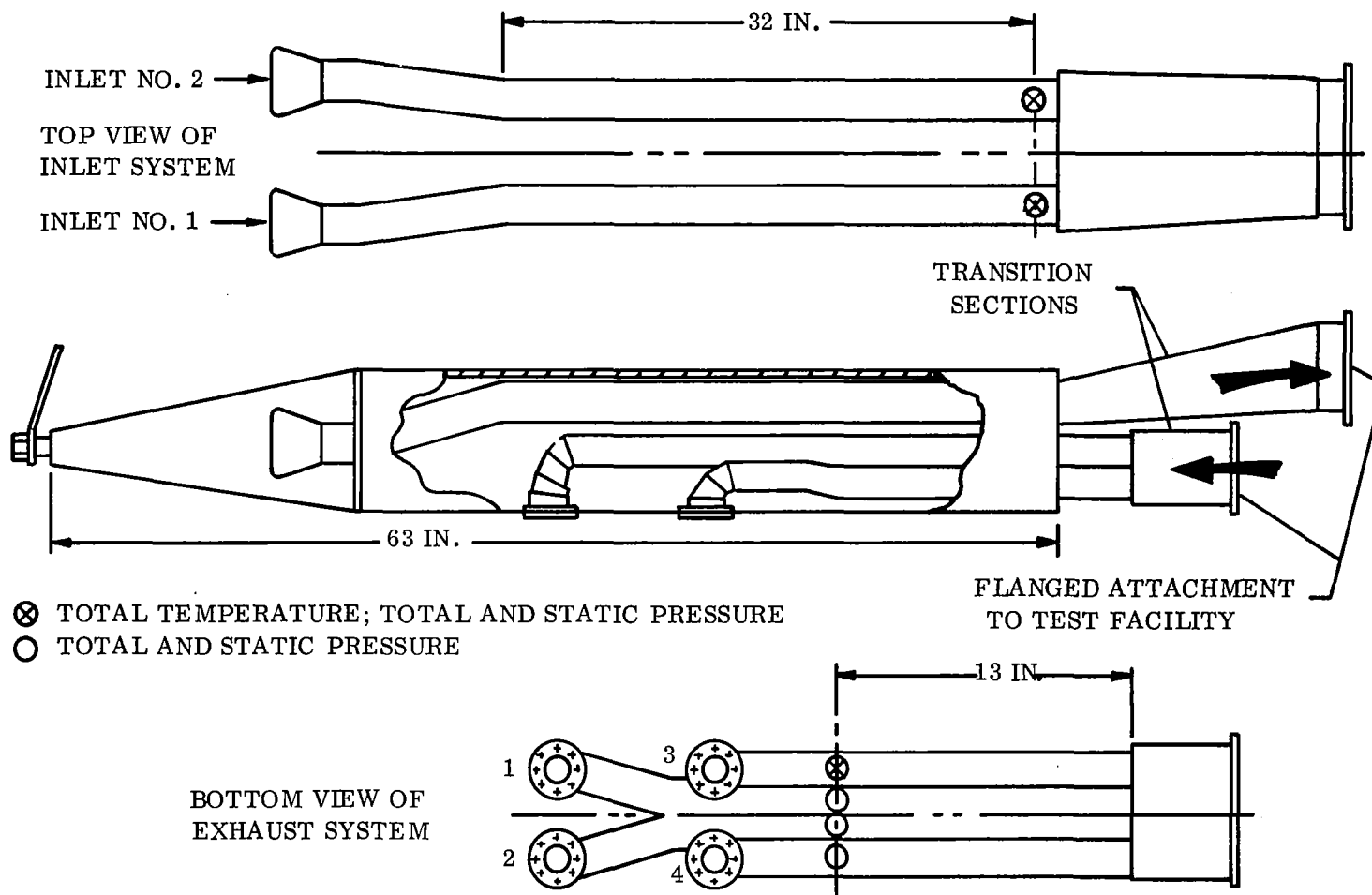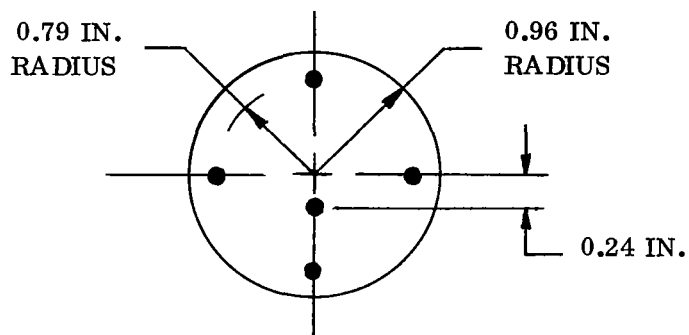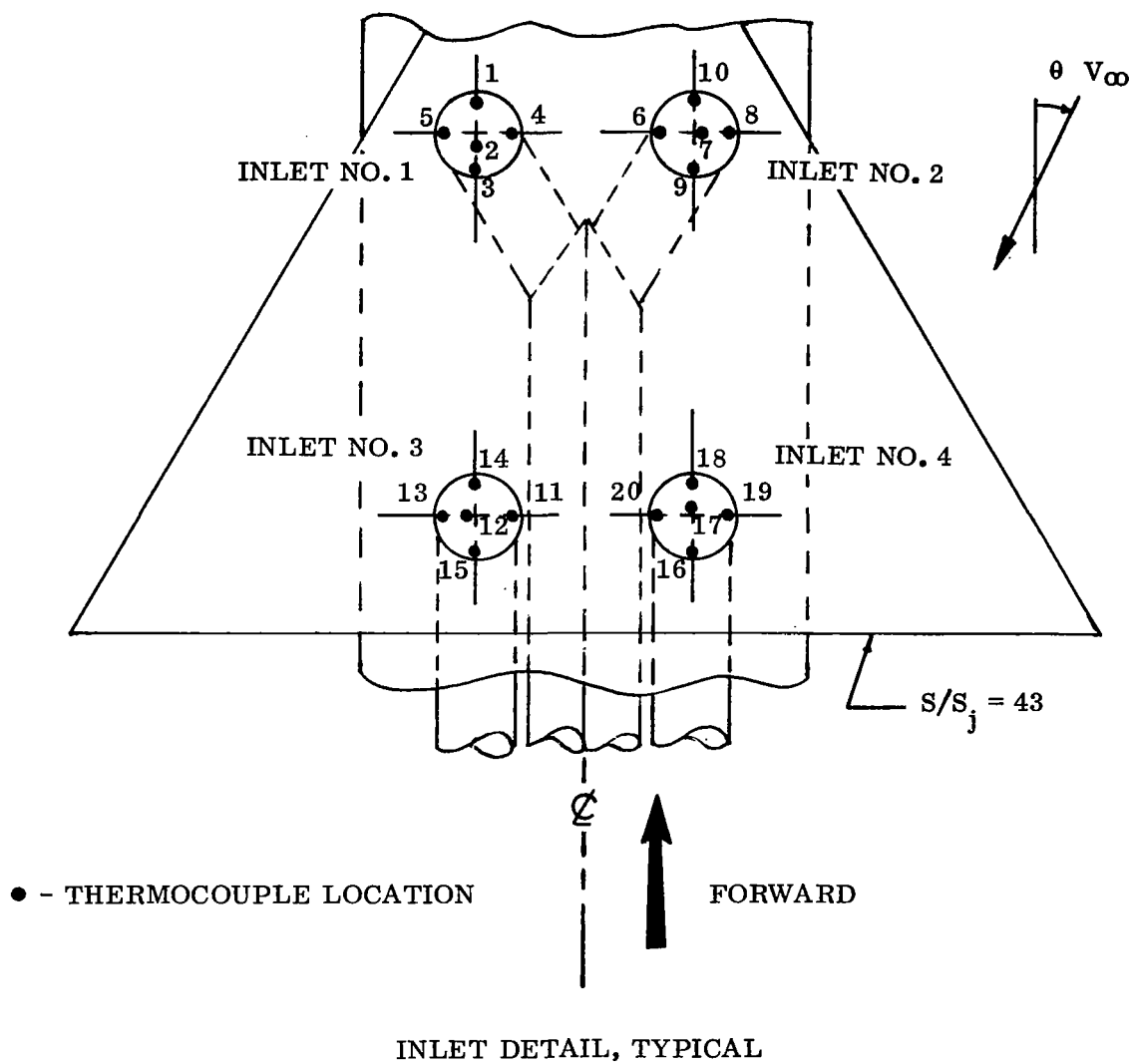
FIGURE 10. - INLET THERMOCOUPLES, TOP INLET CONFIGURATION.

VIEW LOOKING AFT INTO LEFT INLET

PLANE OF PROBES

Notes: (1) Scale Drawing: Location of Thermocouples May Be Scaled.

(2) Thermocouple Identification Numbers Indicate Inlet 1 (Uncircled) And Inlet 2 (Circled).

1 IN.    SCALE

1 IN.
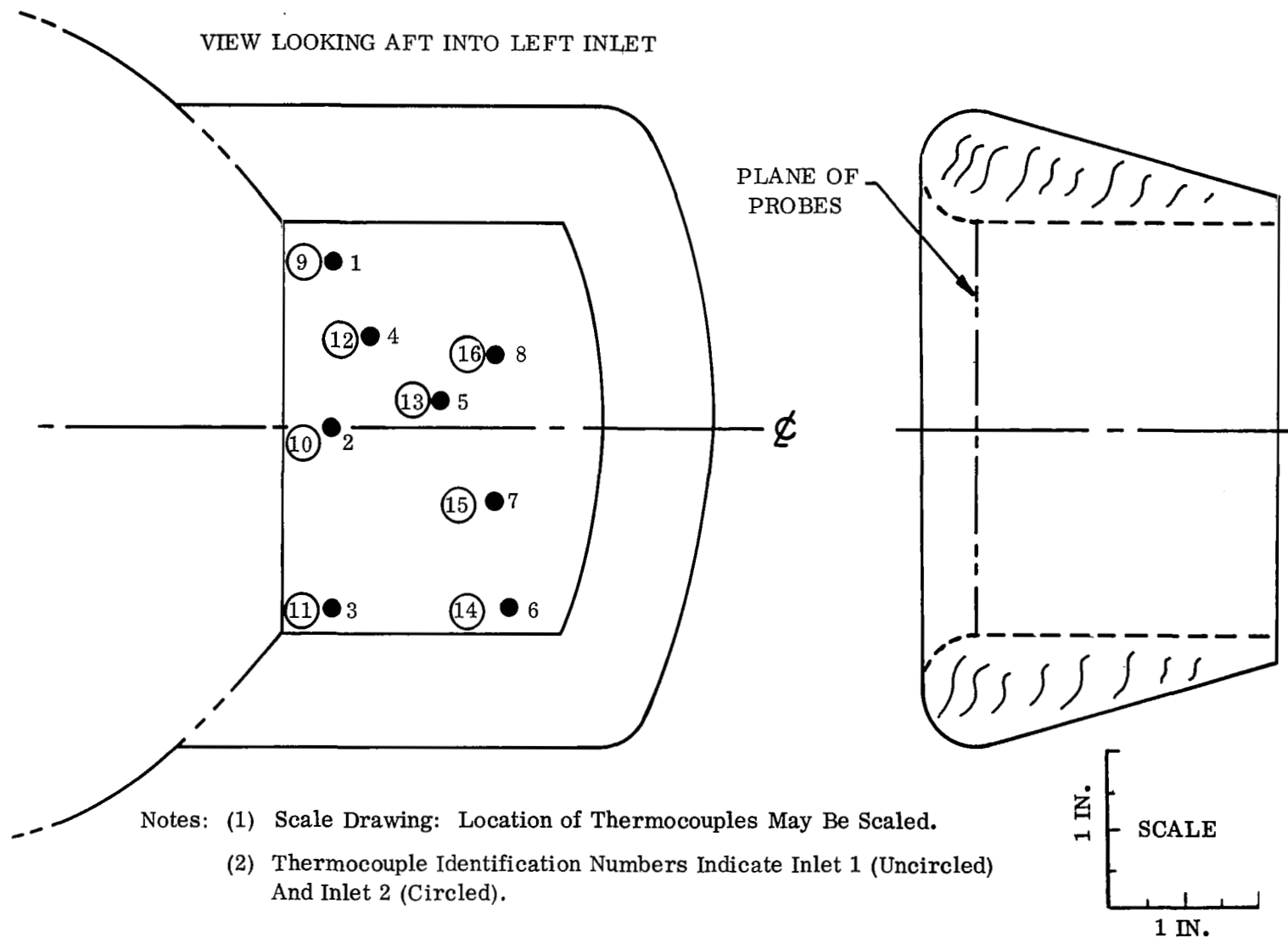
FIGURE 11. - LOCATION OF INLET THERMOCOUPLES, SIDE INLET CONFIGURATION.

RIGHT WING THERMOCOUPLES

$S/S_j = 86$

$S/S_j = 43$

34

18.0 IN.

TOP
VIEW

31

32

33

5.2
IN.

4.4 IN.

12.3 IN.

22.0 IN.

FORWARD

●- THERMOCOUPLE LOCATION

4.3 IN.

FUSELAGE THERMOCOUPLES

EXH. NO. 2

EXH. NO. 4

2.3 IN.

29

25

26

27

BOTTOM
VIEW

2.3 IN.

28

EXH. NO. 1

EXH. NO. 3
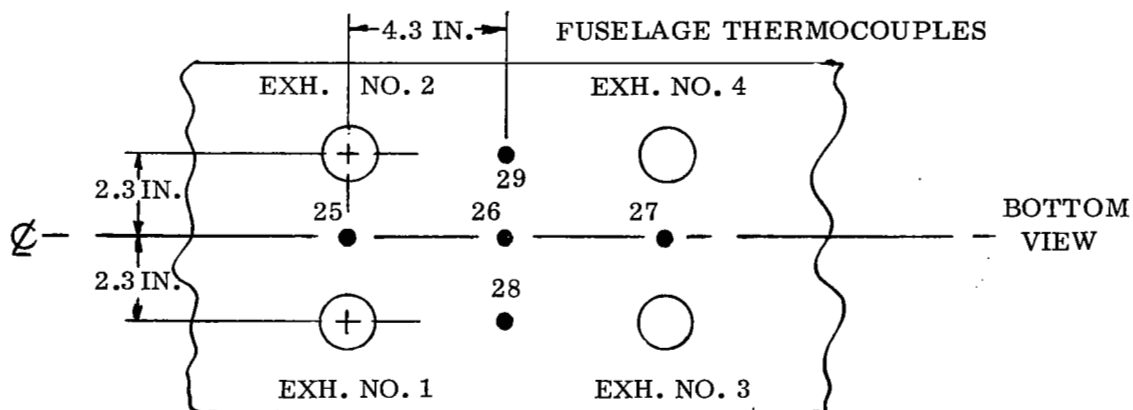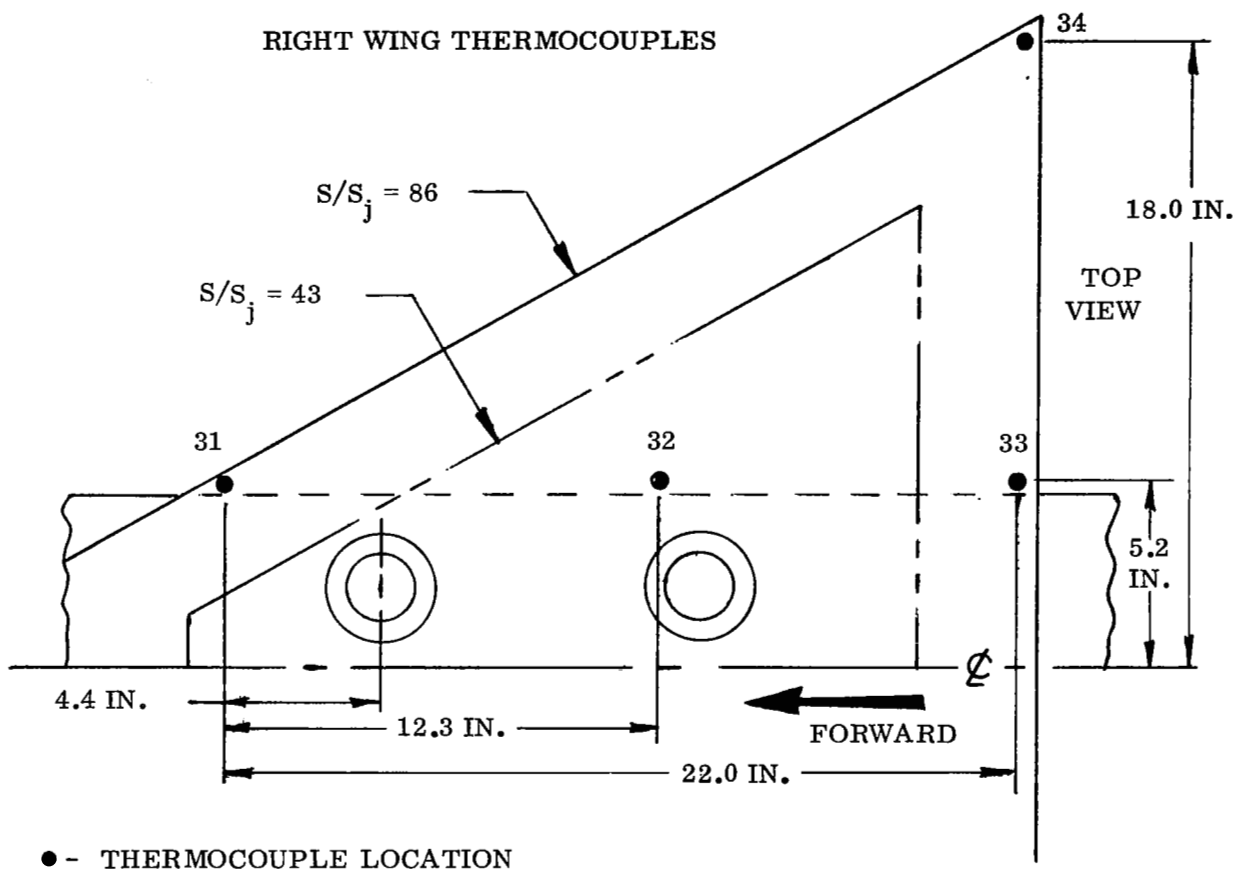
FIGURE 12. - FIELD THERMOCOUPLES, SCALED NASA MODEL.

36

FOR ZERO WIND
SEPARATION OCCURS AT
$50 < R/d_e < 70$

WIND

$R/d_e = 20$    $R/d_e = 50$

DUAL (CIRC) MODEL AT $h/D_e = 1$, $y/D_e = 6.0$

ELEMENTS

a   JET EXHAUST PLUME
b   RADIAL GROUND FLOW JET
c   REINFORCED GROUND FLOW JET
d   FAR FIELD
e   FOUNTAIN
f   JET INDUCED FLOW
g   INLET SINK
h   WIND
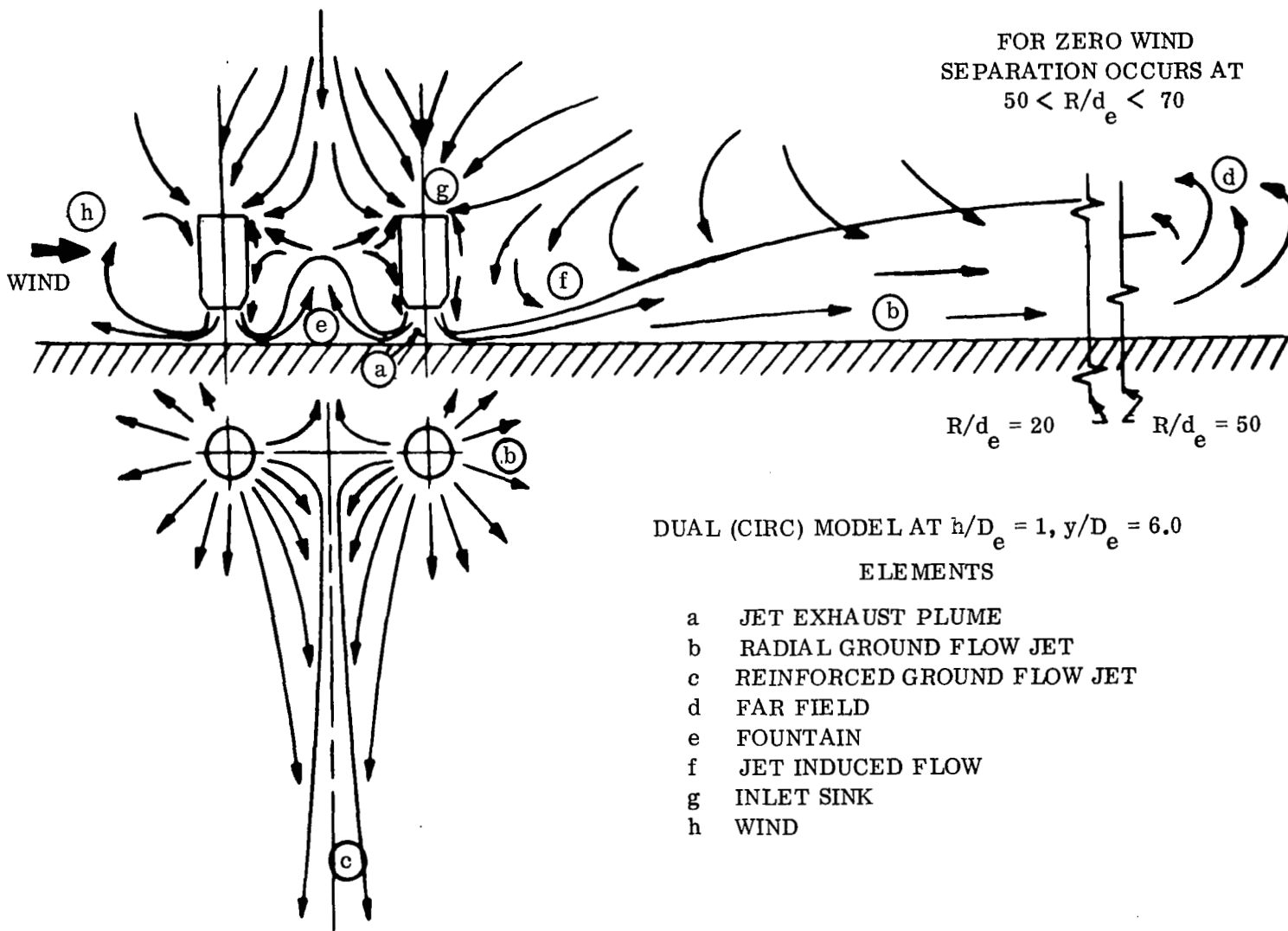
FIGURE 13. – GENERAL FLOW FIELD ELEMENTS.

37

i  PEELING LINE
J  EDDY AT PEELING LINE
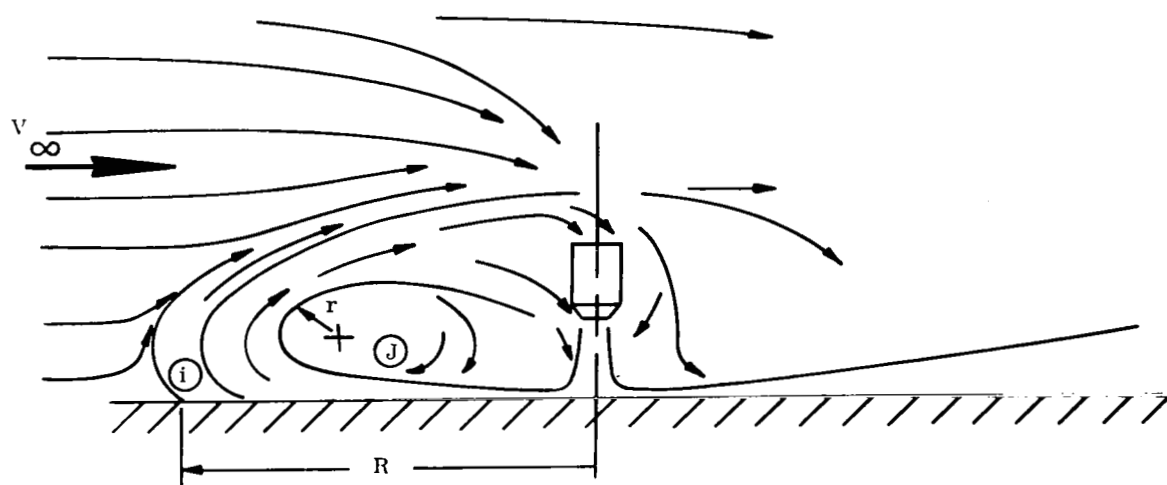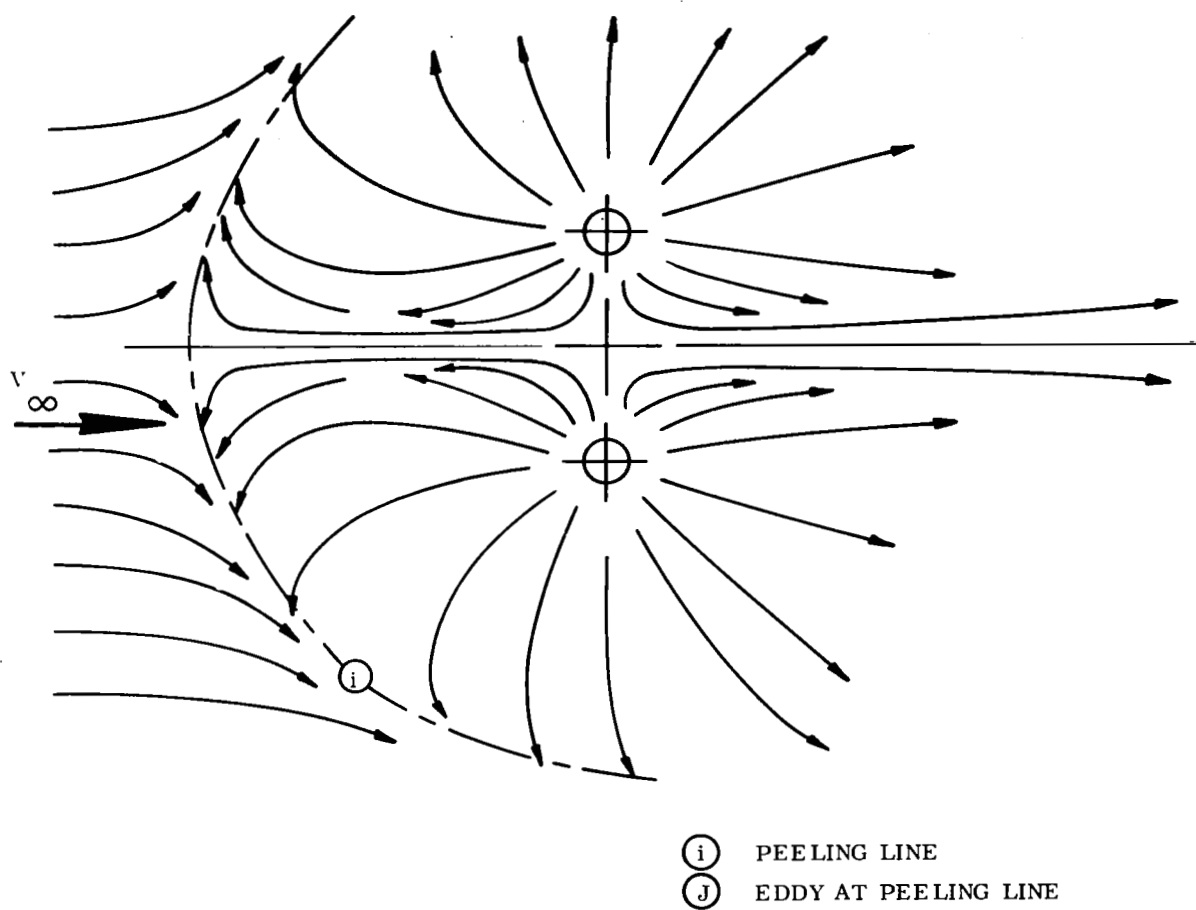
FIGURE 14. – EFFECT OF WIND ON REINFORCED GROUND JET.

38

Distance of Peeling Line From Center of Exhaust Pattern $R/D_e$

$V_\infty$ , FPS

$\theta$

$\bigcirc$ = $0°$  
$\square$ = $-30°$  $\Big\}$ DUAL (CIRC) MODEL $h/D_e$ = 2, $y/D_e$ = 10  
$\triangle$ = $-60°$

$\diamond$ = $0°$ POD (CIRC) MODEL $h/D_e$ = 3, $y/D_e$ = 8.6  
$\sigma$ = $0°$ DUAL (CIRC) MODEL $h/D_e$ = 2, $y/D_e$ = 10 (REF. 2)

PEELING REGION
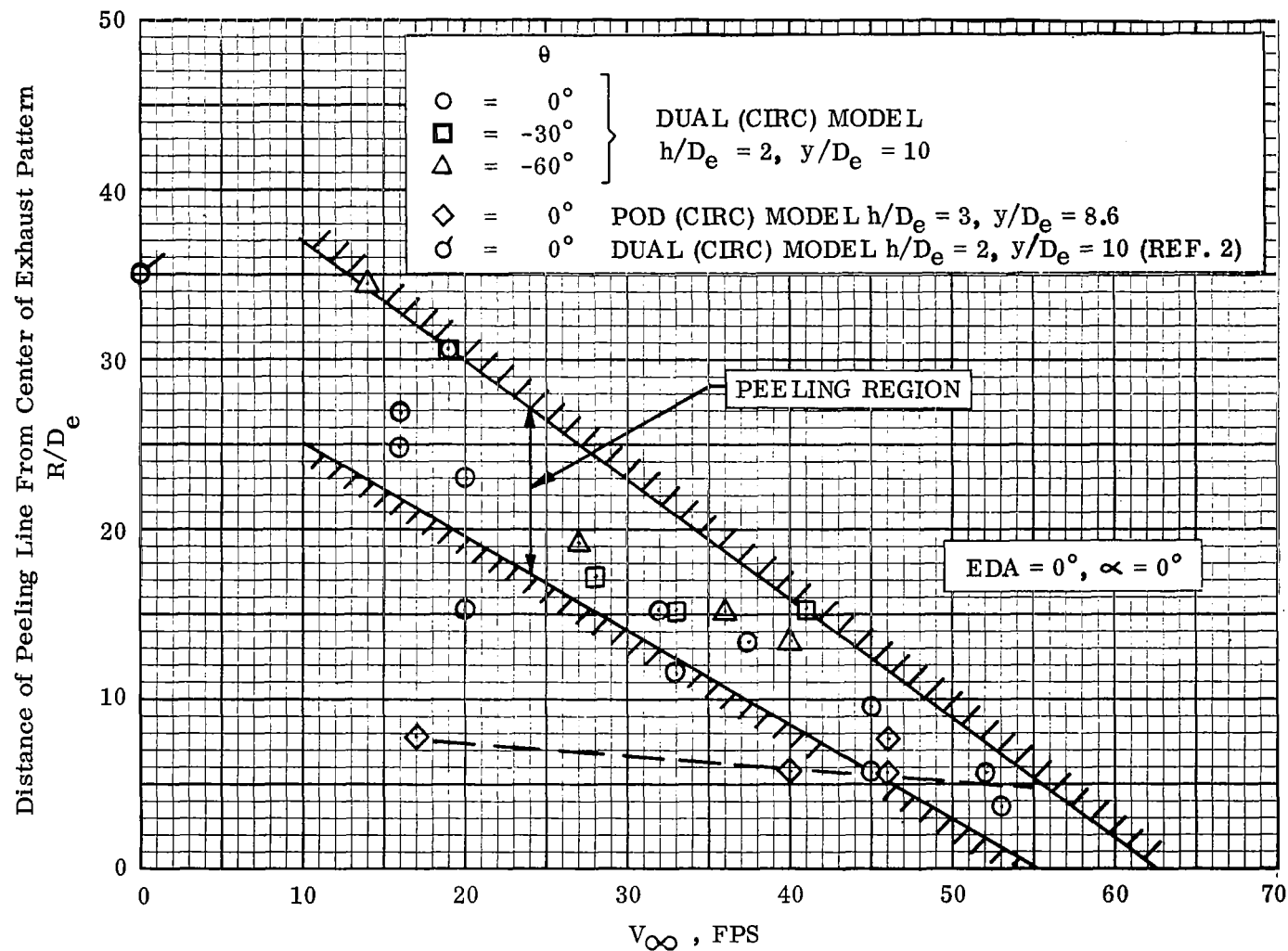
EDA = $0°$, $\alpha = 0°$

FIGURE 15. - VARIATION OF GROUND JET PEELING RADIUS WITH $V_\infty$ FOR POD AND DUAL MODELS.
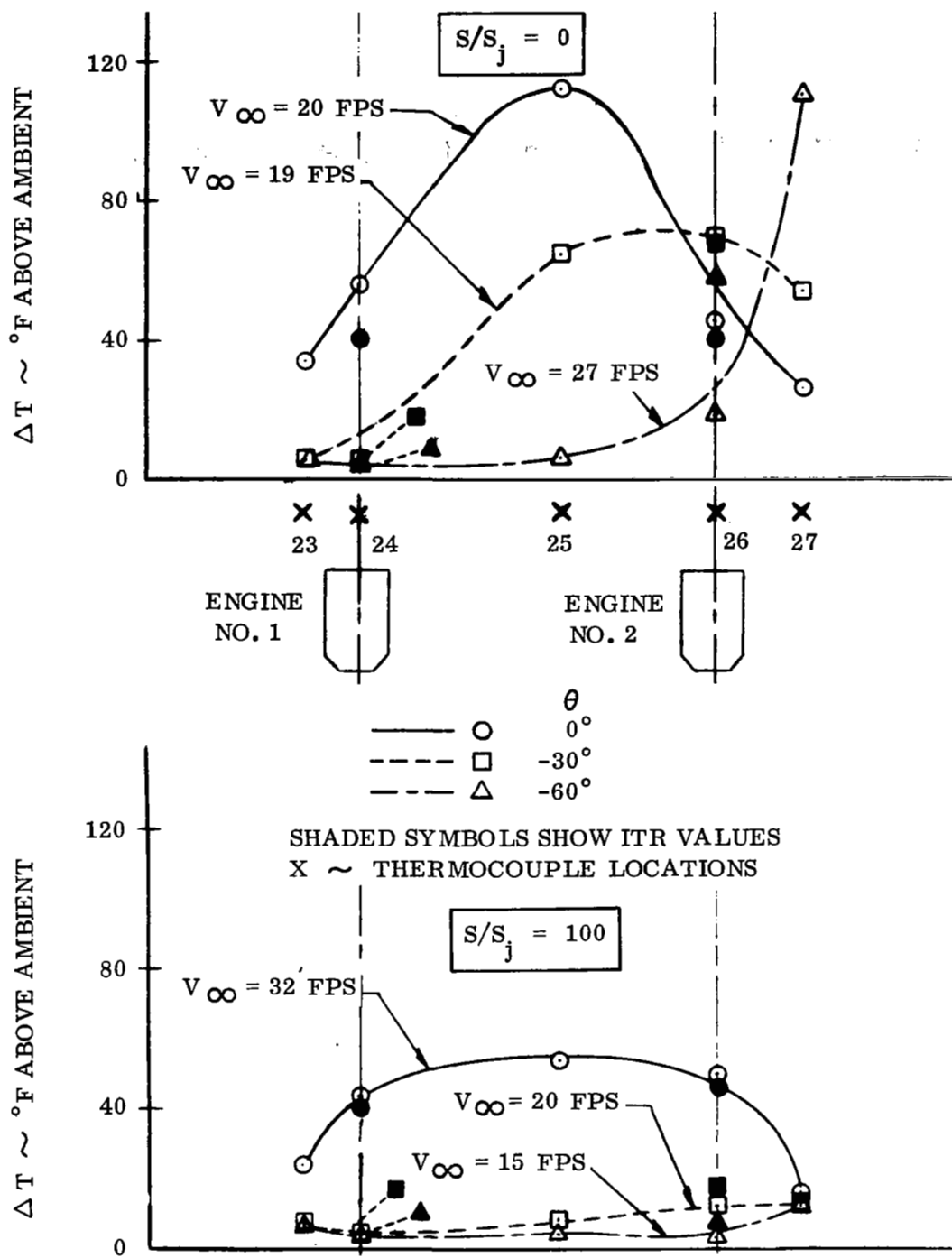
Figure 16. – Temperature Gradients In The Field Above The Dual (circ) Model For Various $\theta$.    $h/D_e = 2$, EDA $= 0°$, $\alpha = 0°$, And $V_\infty$ For ITR$_{MAX}$.
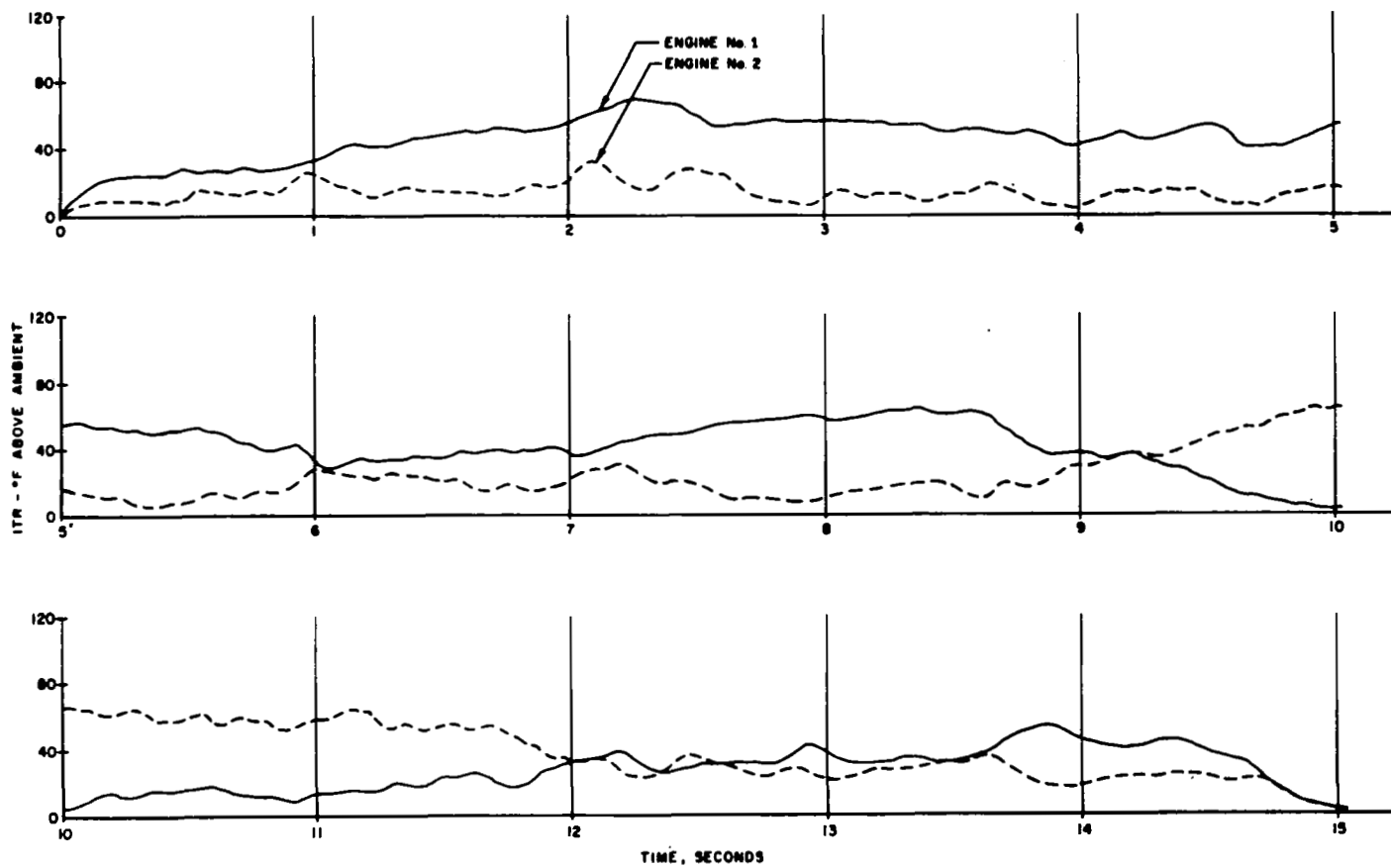
FIGURE 17. – TEMPERATURE TIME HISTORY, DUAL (circ) MODEL, WING OFF, $h/D_e = 2$, $V_\infty = 11$ FPS, $\theta = 0°$.
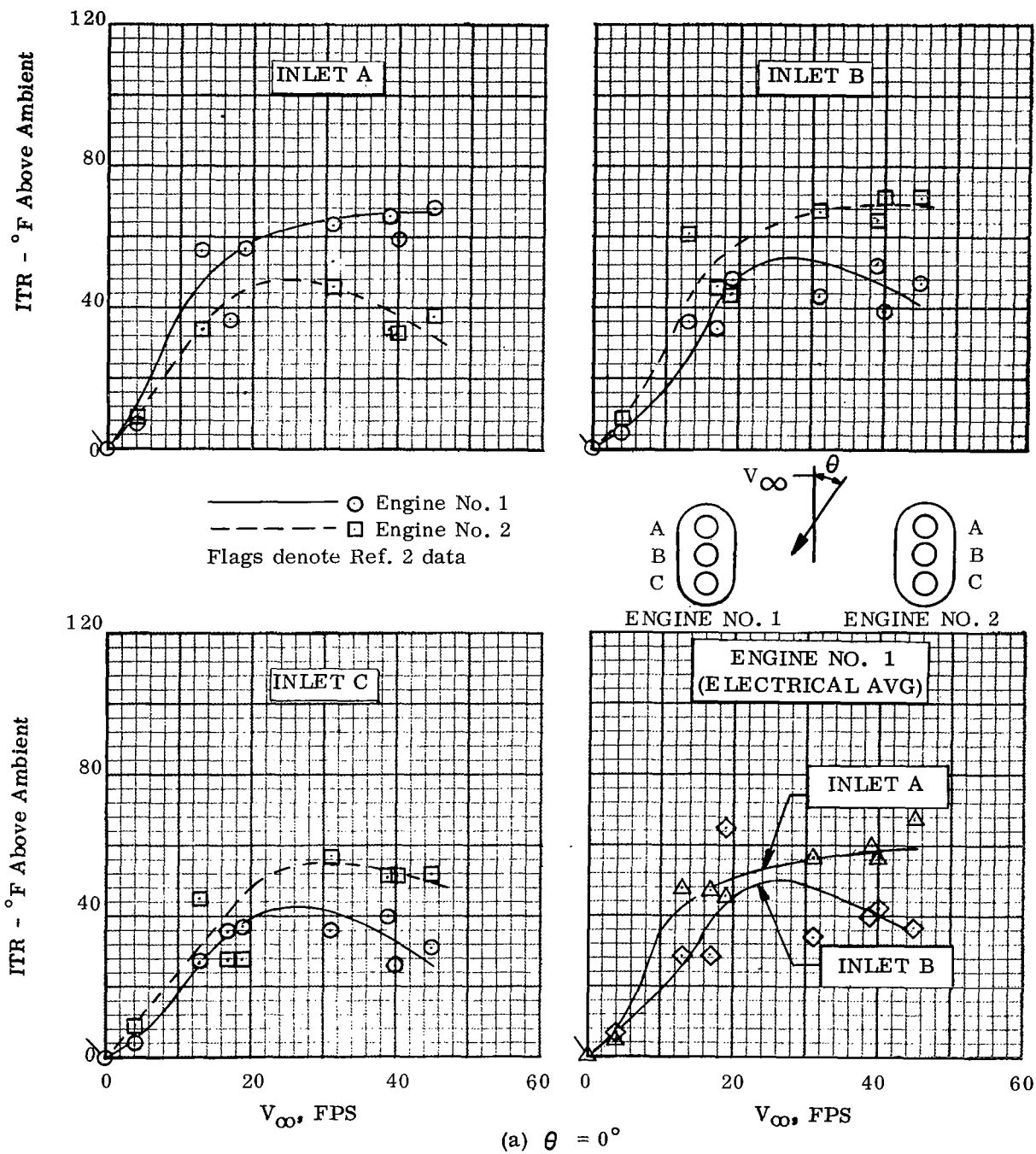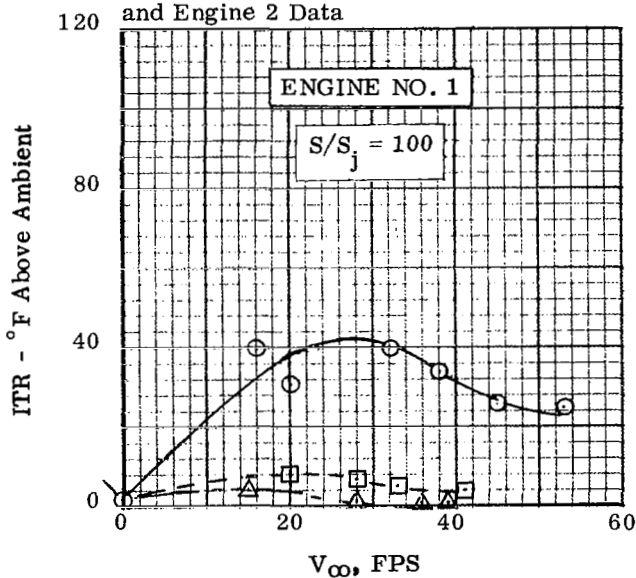
Figure 18. – Variation of ITR With $V_\infty$ For Pod (circ)
Model At $h/D_e = 3$, EDA = $0°$, and $\alpha = 0°$. $S/S_j = 100$.

(a) $\theta = 0°$

(b) $\theta = -30°$
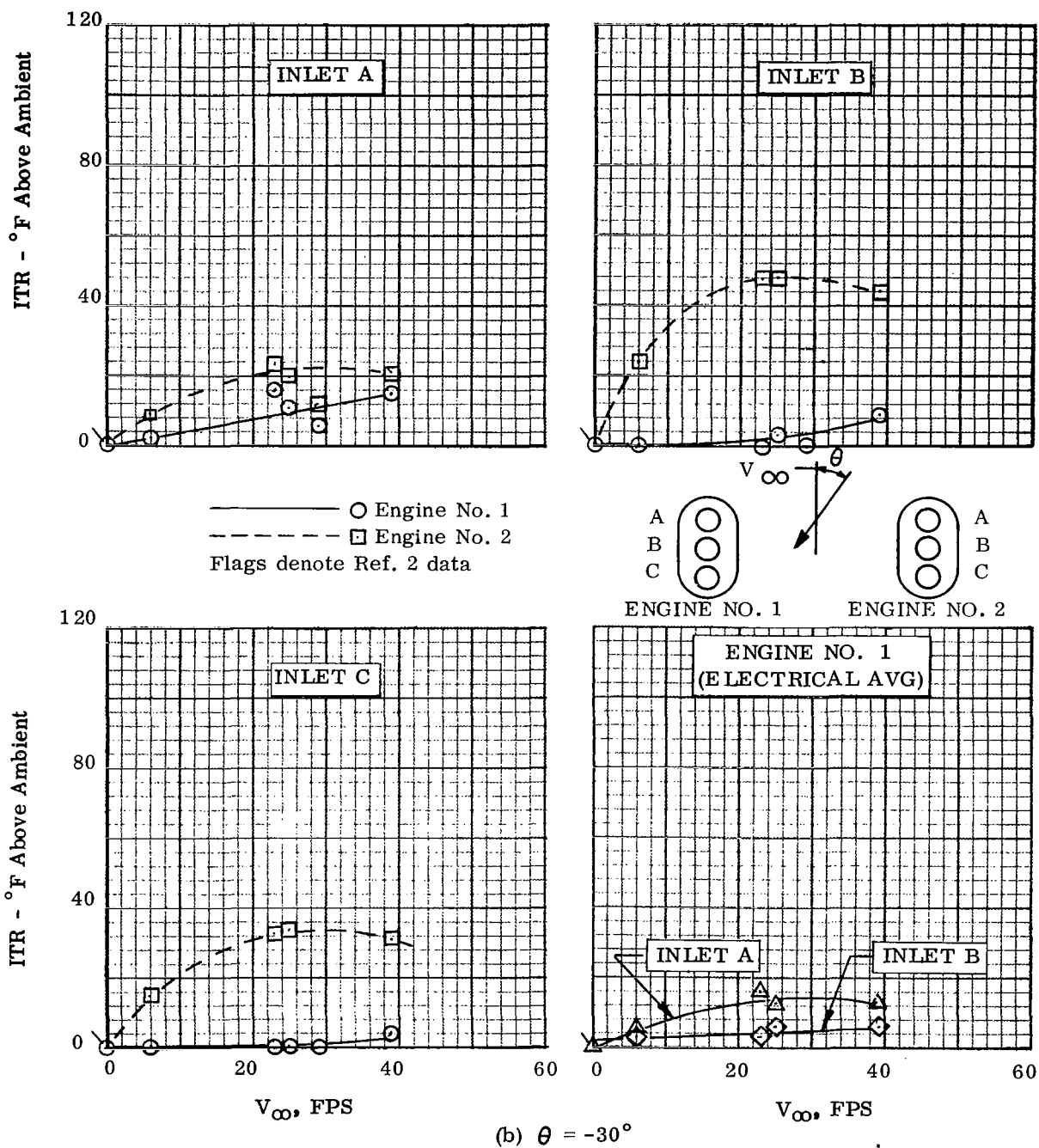
Figure 18.—Continued.
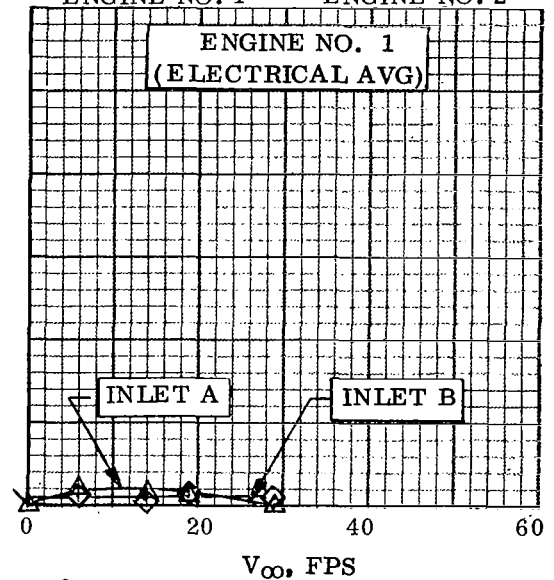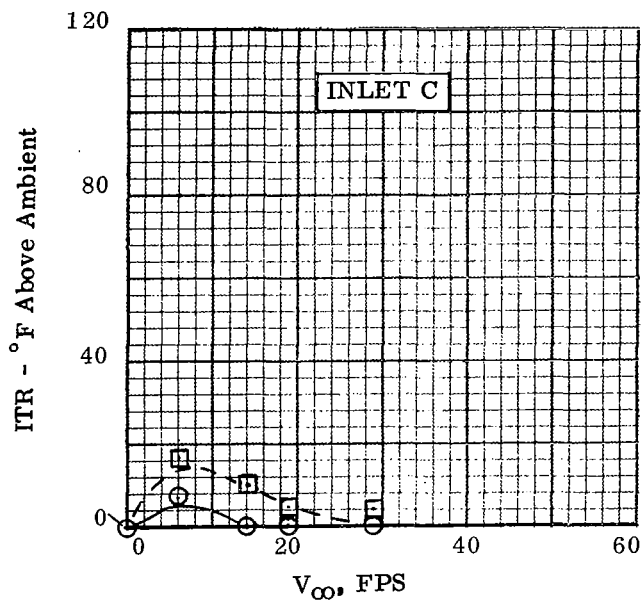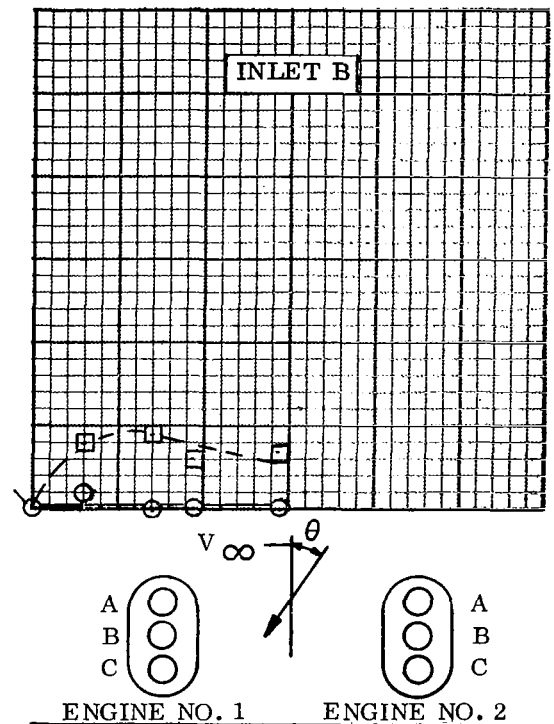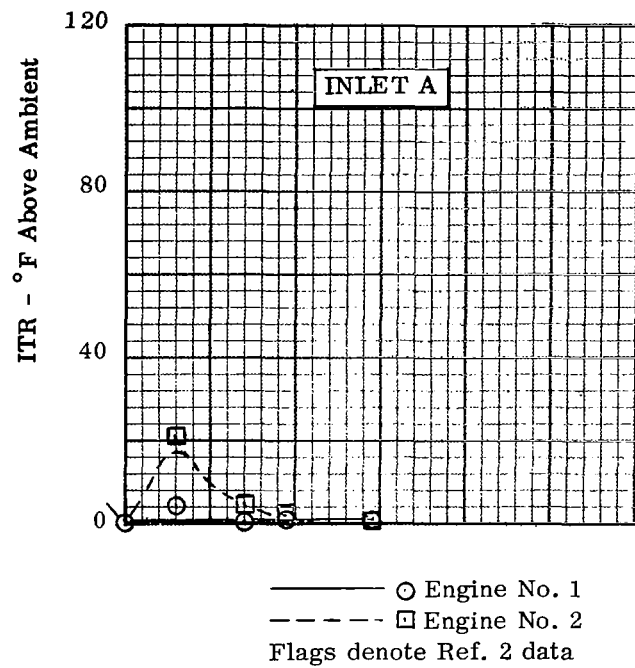
(c) $\theta = -60°$

Figure 18.—Concluded.
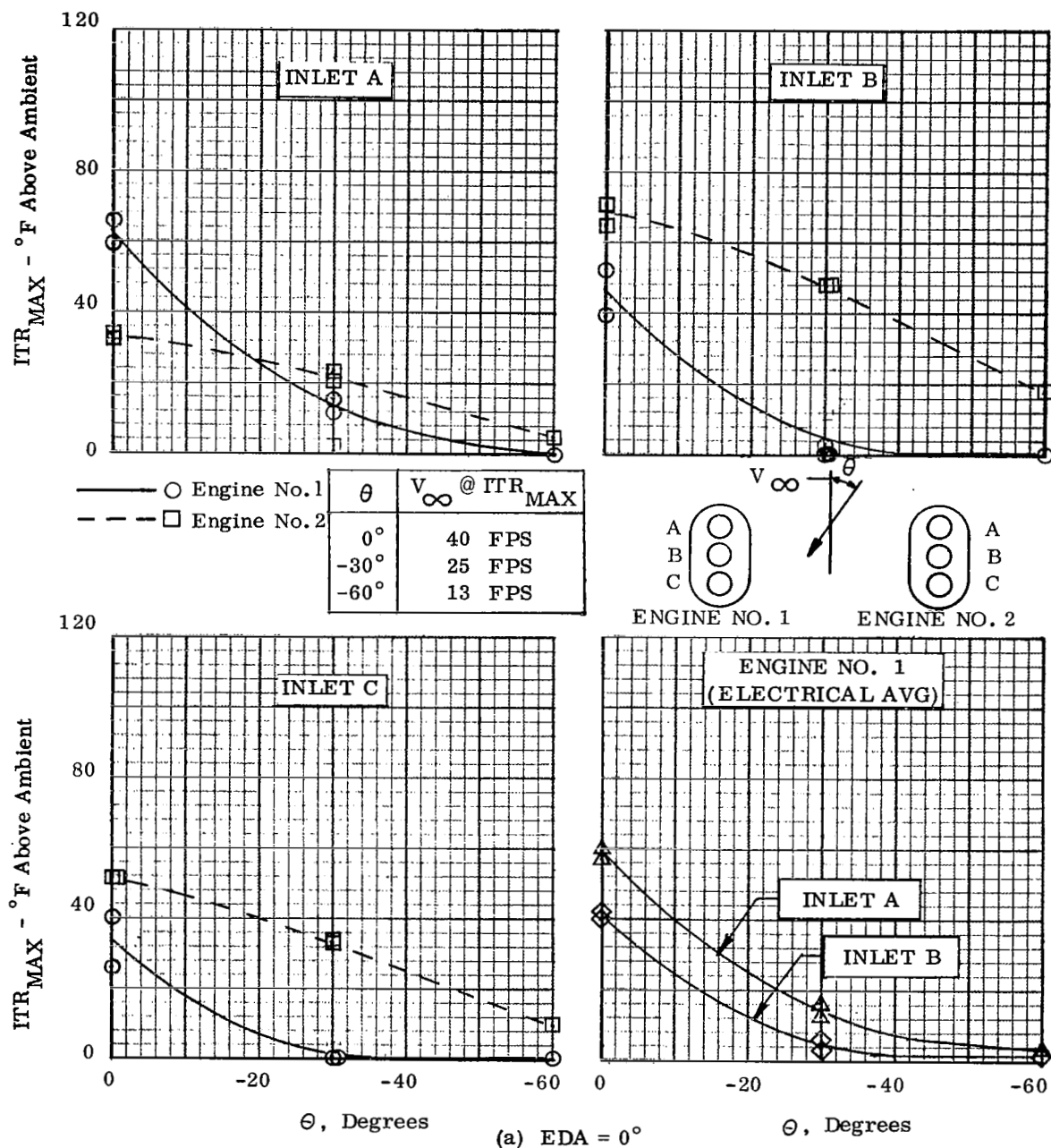
Figure 19. - Variation of $ITR_{MAX}$ With $\theta$ For Pod (circ) Model At $h/D_e = 3$, $\alpha = 0°$ and $V_\infty$ For $ITR_{MAX}$.
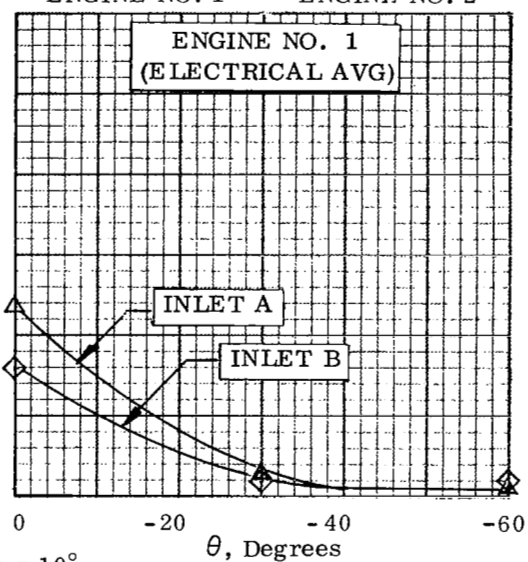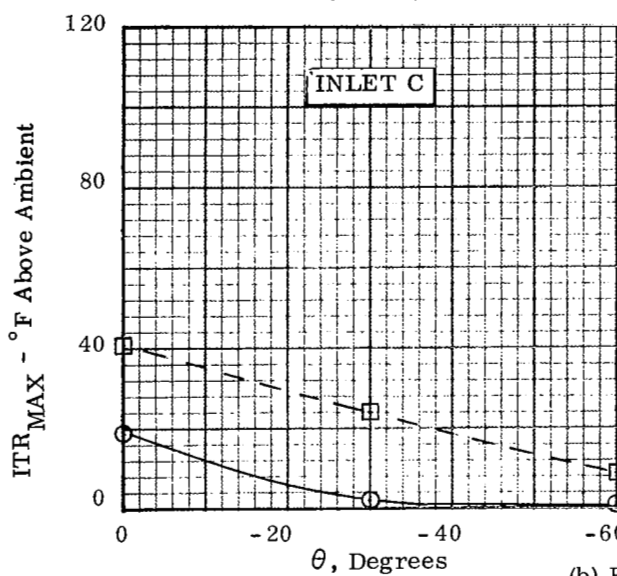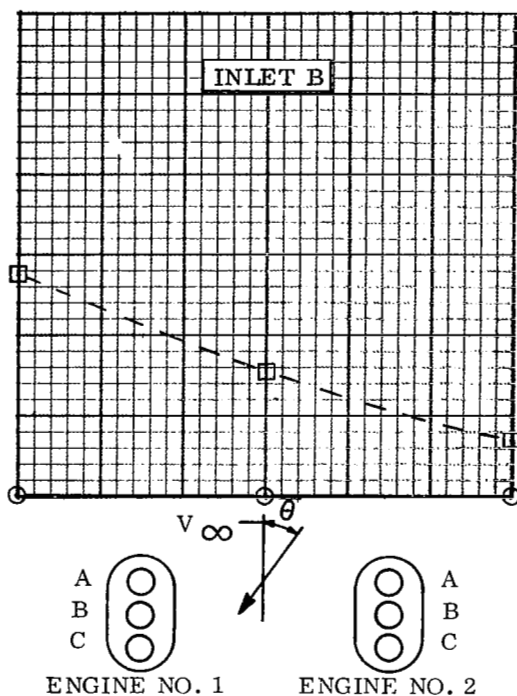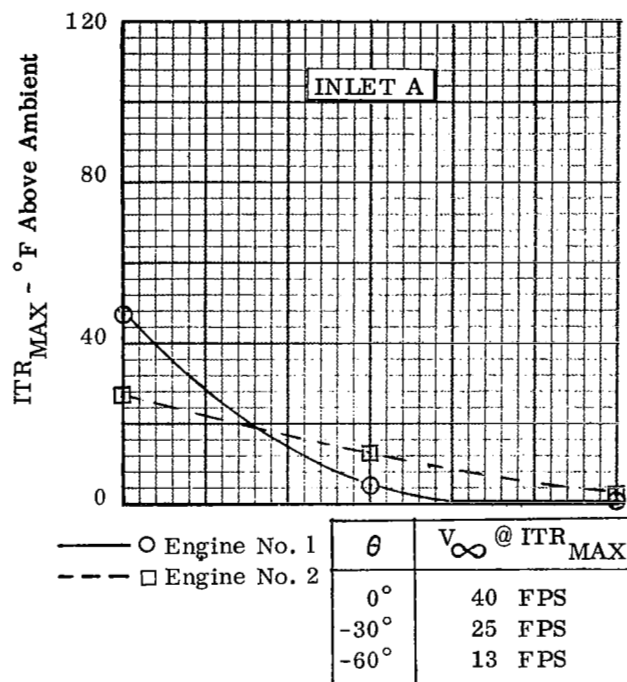
(b) EDA = $10°$

Figure 19. Continued.
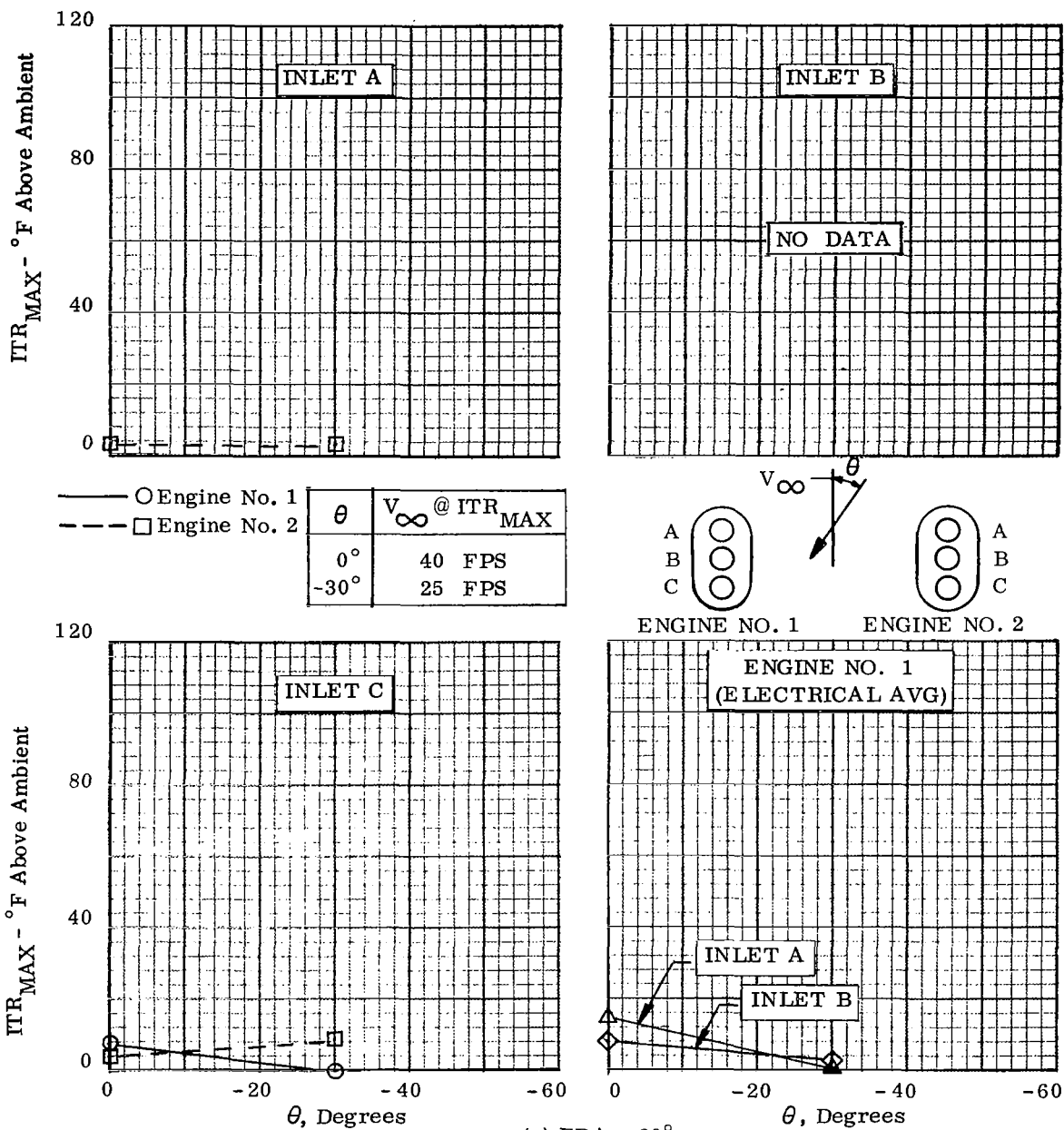
(c) EDA = 20°

Figure 19.—Concluded.
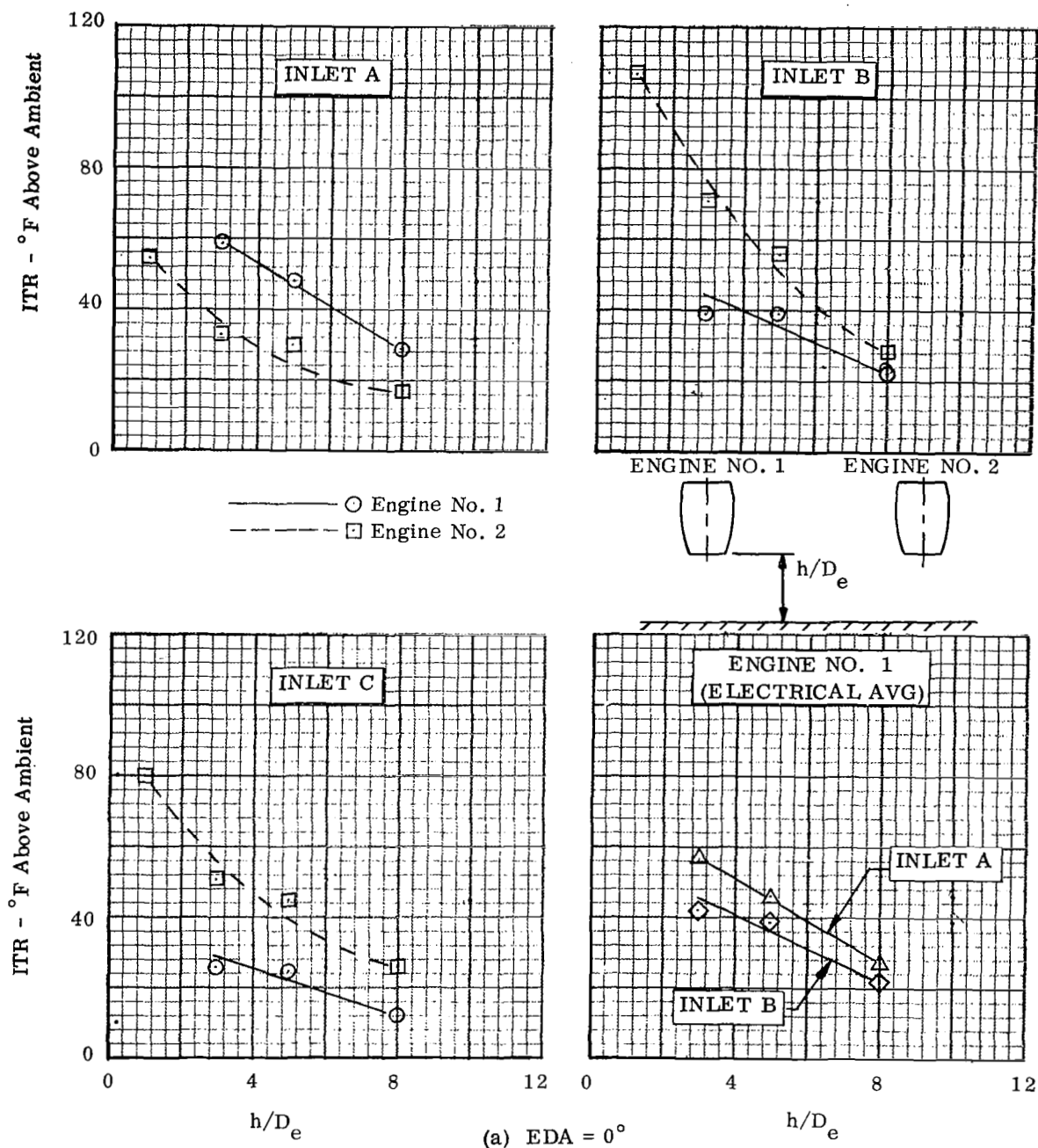
Figure 20. – Variation of ITR With $h/D_e$ For Pod (circ) Model At $\theta = 0°$, $\alpha = 0°$, and $V_\infty = 40$ fps, $S/S_j = 100$.

48
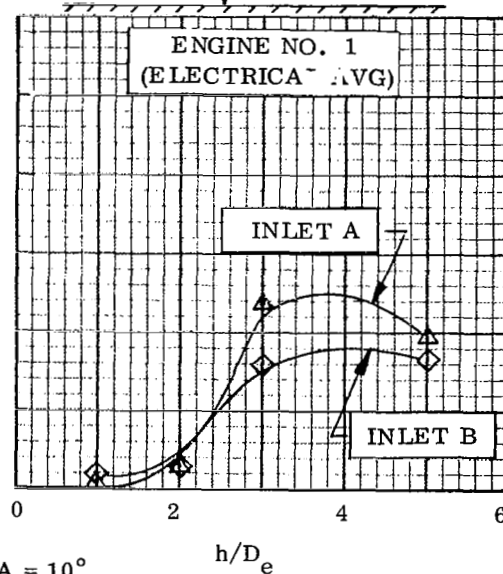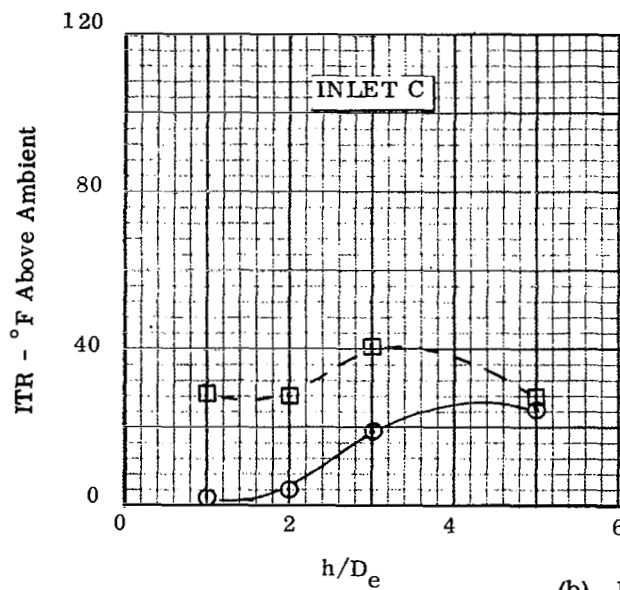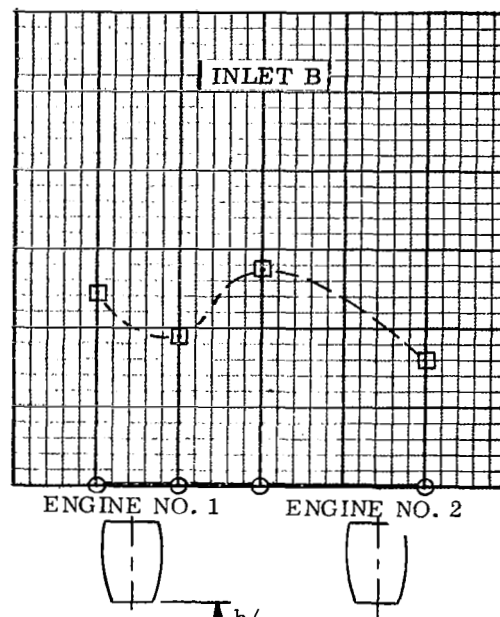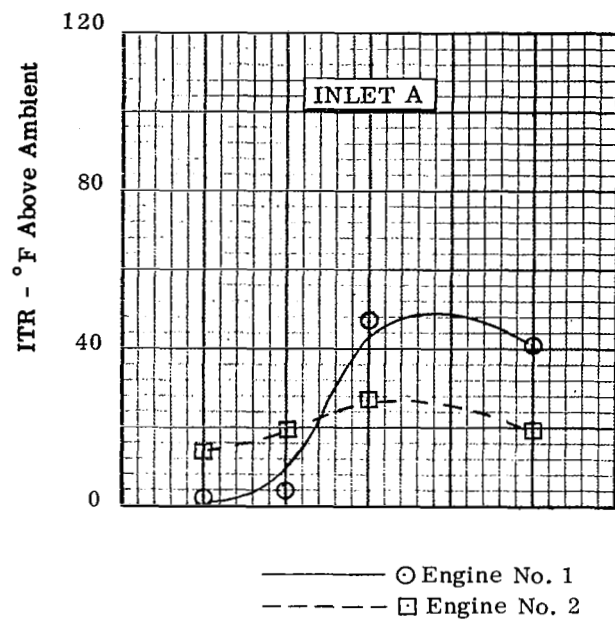
(b)  EDA = 10°

Figure 20.-Continued.

49
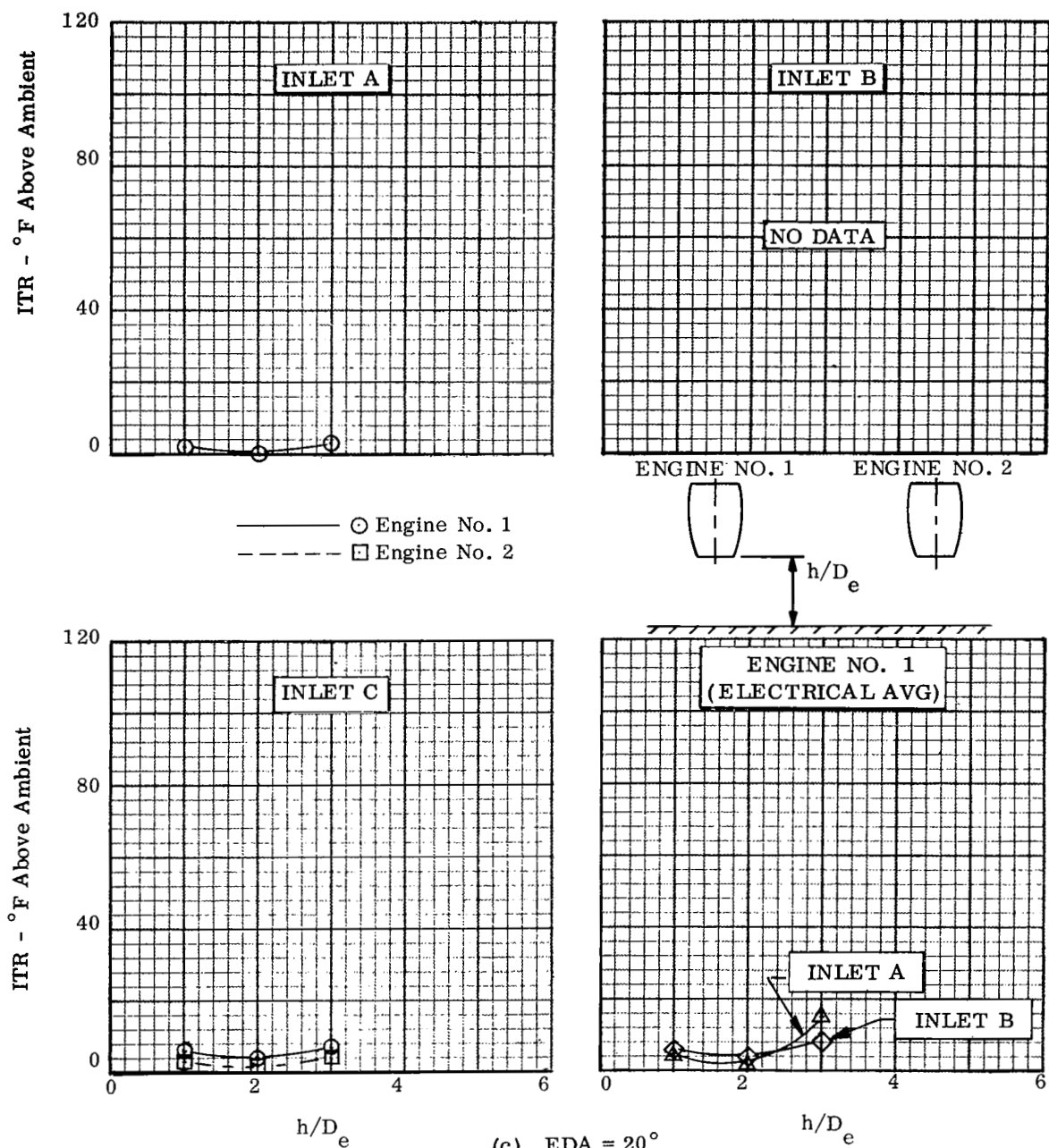
(c)   EDA = $20°$

Figure 20.—Concluded·

50
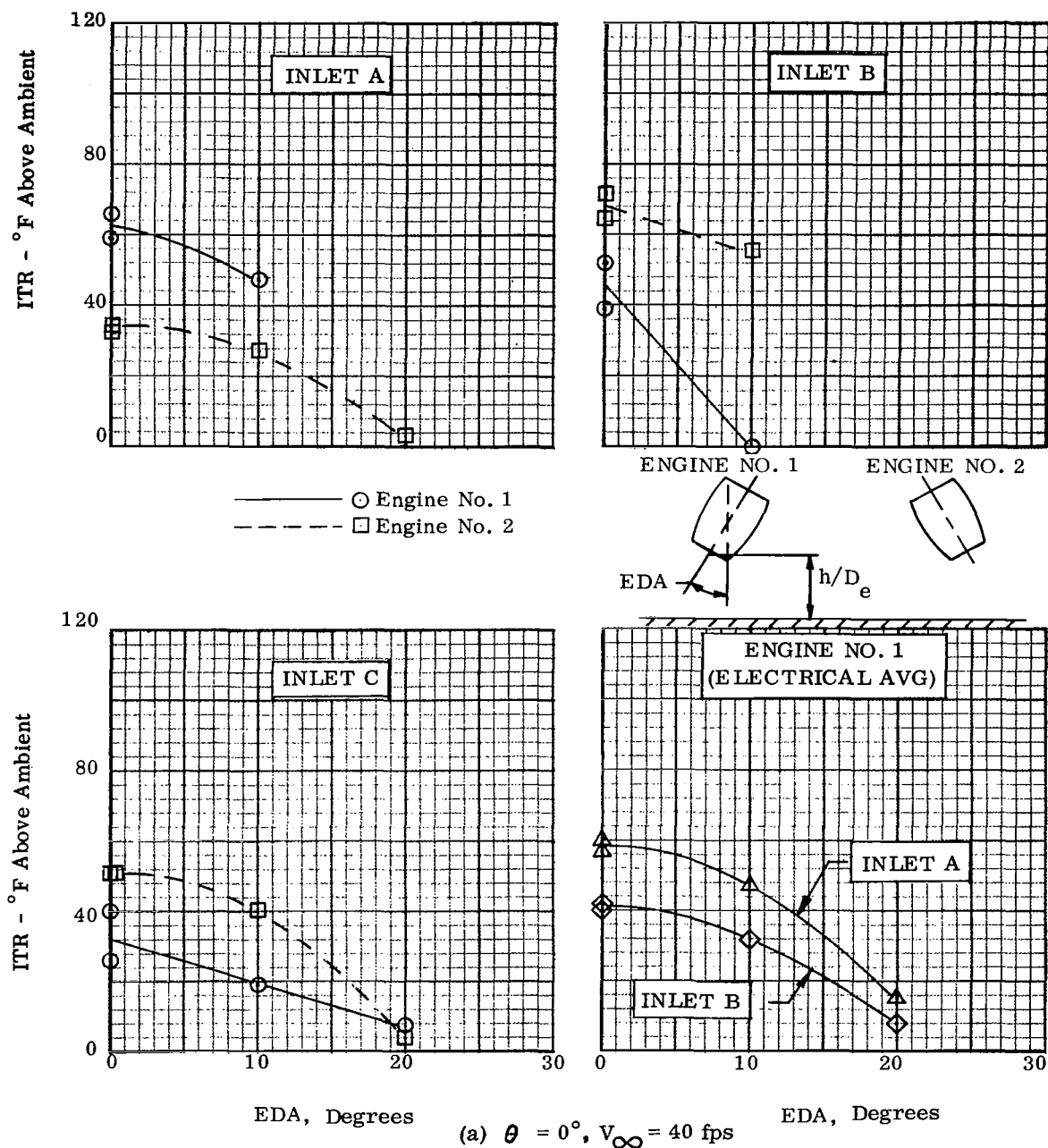
Figure 21. – Variation Of ITR With EDA For Pod (circ) Model At $h/D_e = 3$, $\alpha = 0°$, and $V_\infty$ For $ITR_{MAX}$. $S/S_j = 100$.

51

ITR - °F Above Ambient

INLET A

INLET B

————○ Engine No. 1
— — — □ Engine No. 2

ENGINE NO. 1        ENGINE NO. 2

EDA

h/D$_e$

INLET C

ENGINE NO. 1
(ELECTRICAL AVG)

INLET A

INLET B

EDA, Degrees

EDA, Degrees
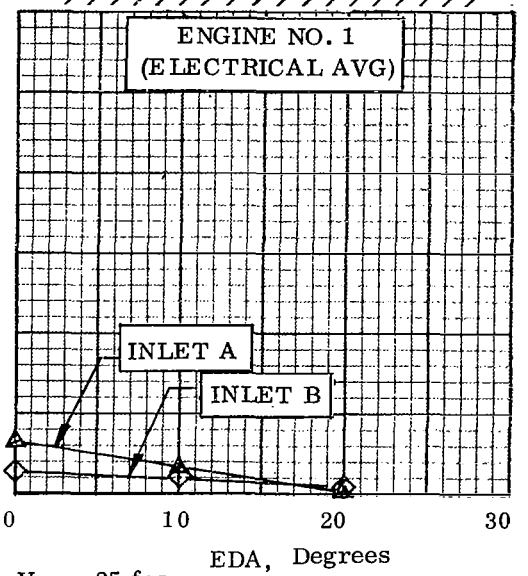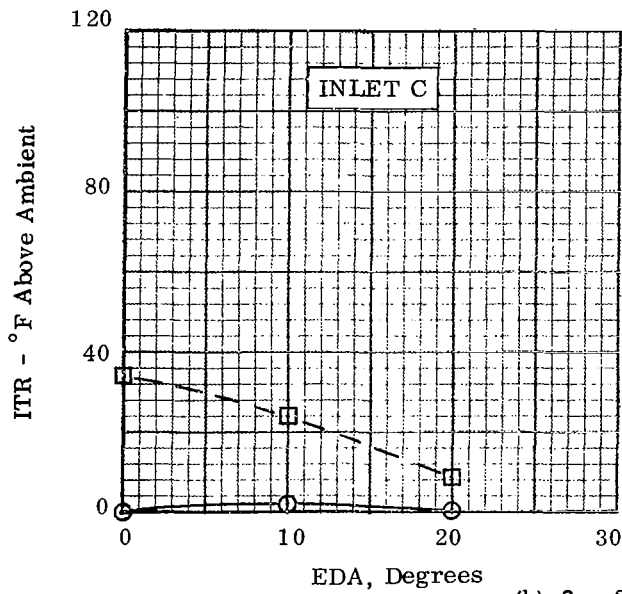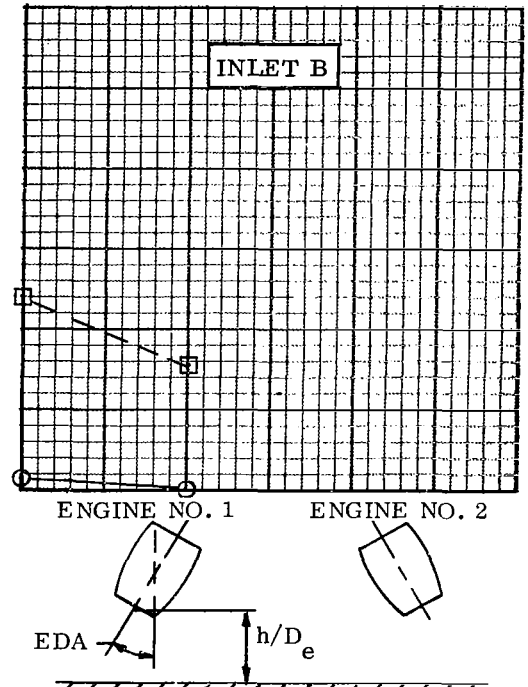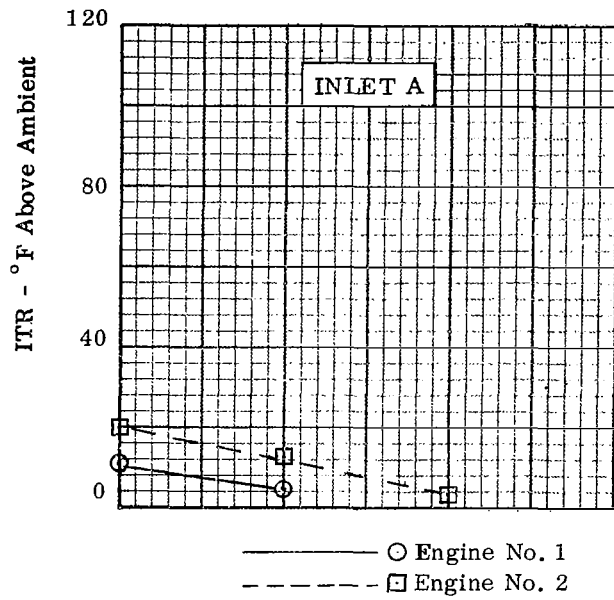
(b) $\theta = -30°$, $V_\infty = 25$ fps

Figure 21.-Concluded.
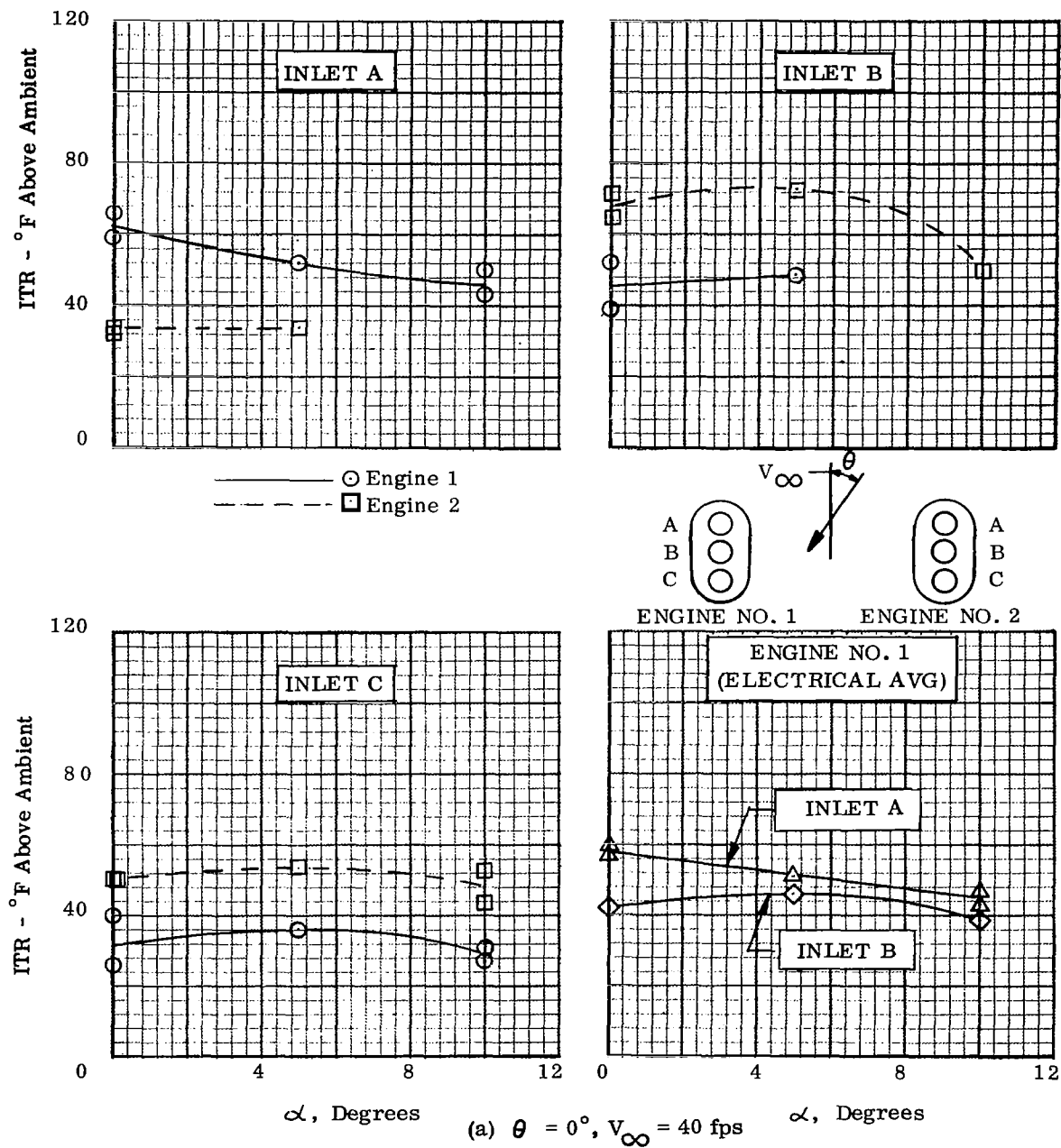
Figure 22. - Variation Of ITR With  θ  For Pod (circ) Model At h/D$_e$ = 3,
EDA = 0°, And V$_\infty$  For ITR$_{MAX}$. S/S$_j$ = 100.
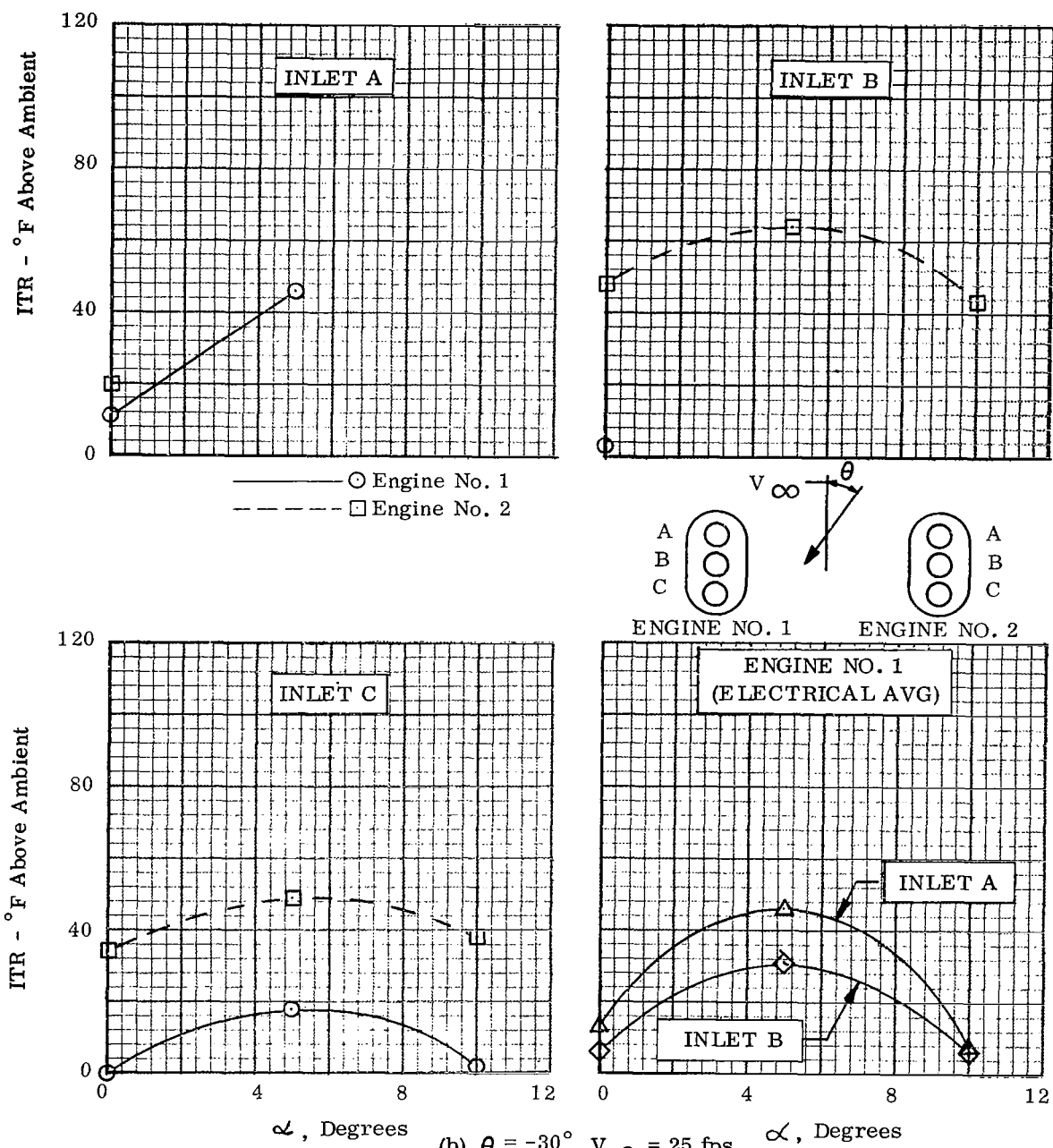
(b) $\theta = -30°$, $V_\infty = 25$ fps

Figure 22.-Concluded.

54
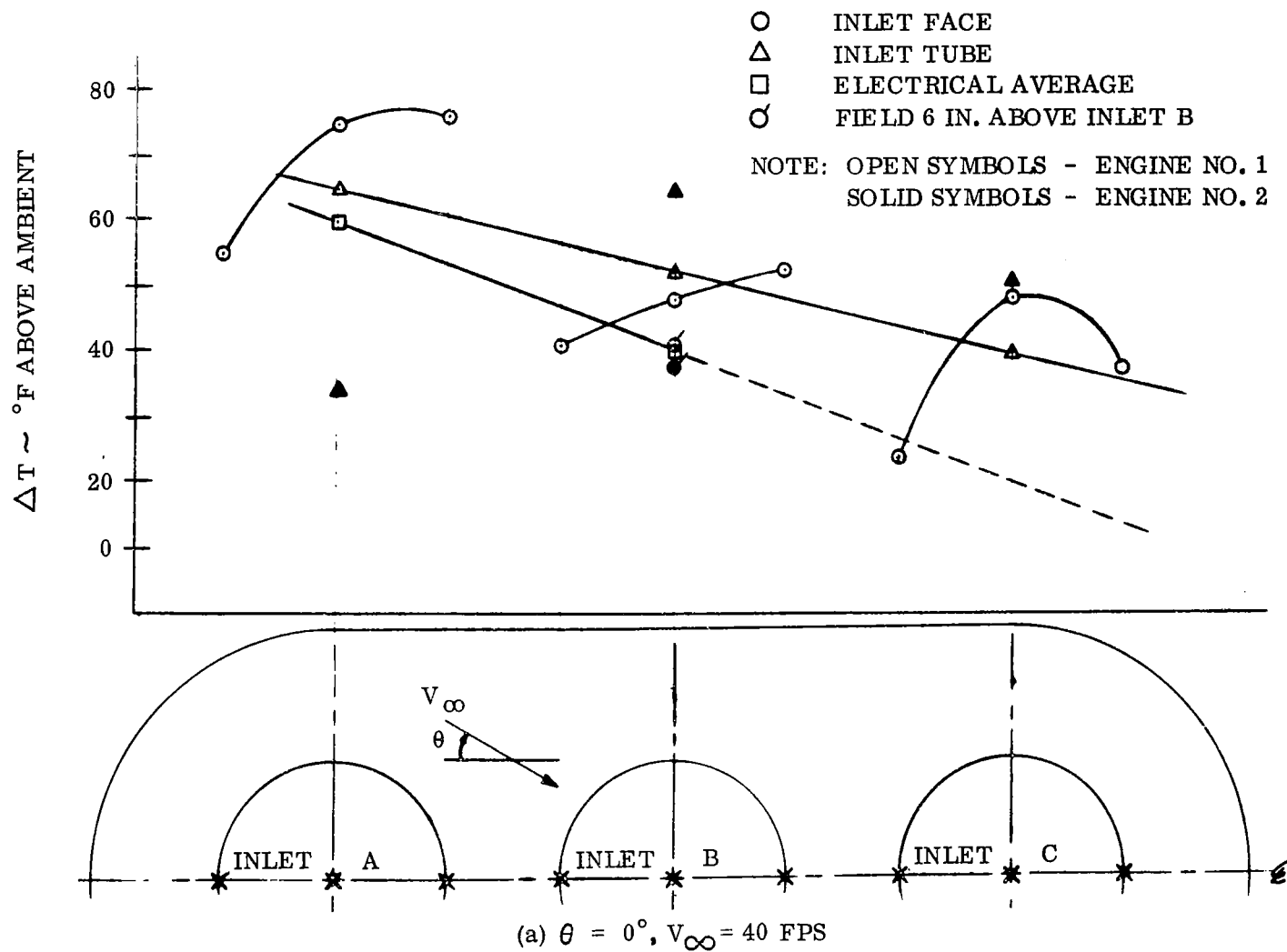
Figure 23. – Variation Of ITR With Length Along The Pod (circ) Model At $h/D_e$ = 3, EDA = 0°
$\alpha$ = 0°, And $V_\infty$ For $ITR_{MAX}$.

(b) $\theta = -30°$, $V_\infty = 25$ FPS
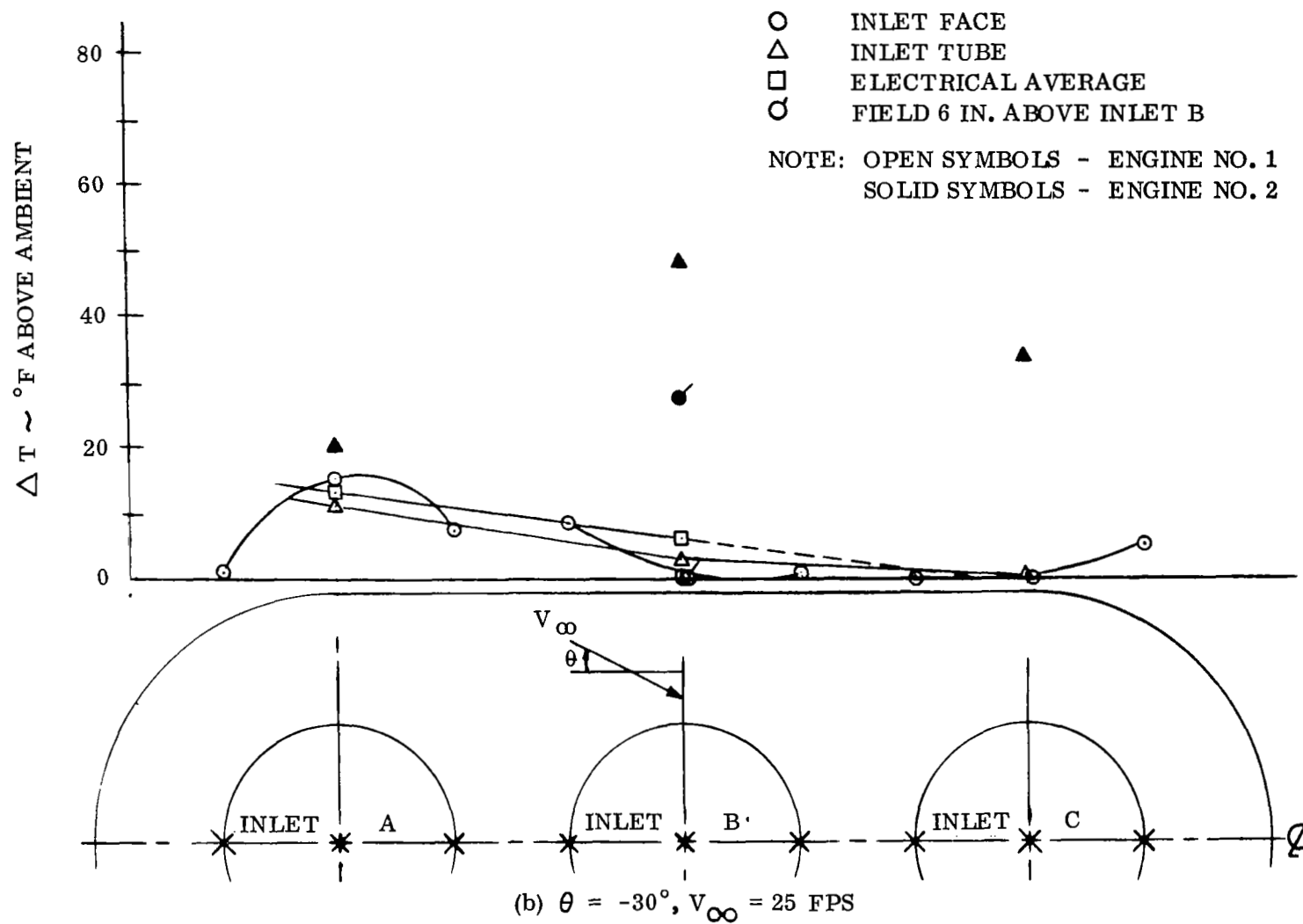
Figure 23. - Concluded.
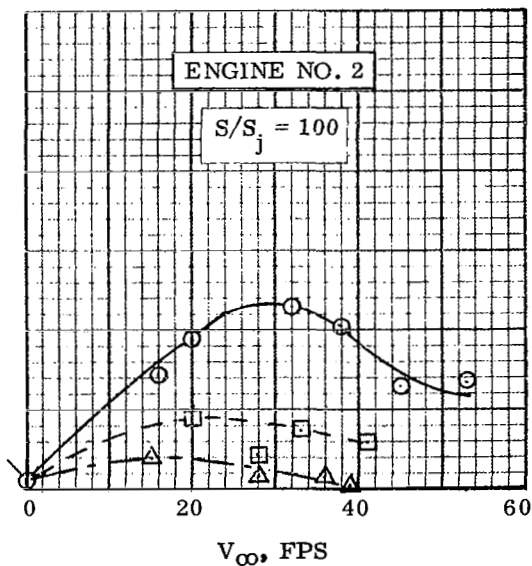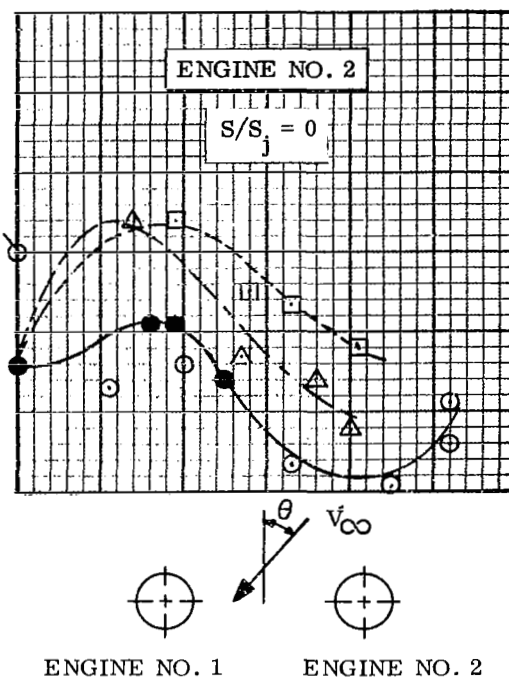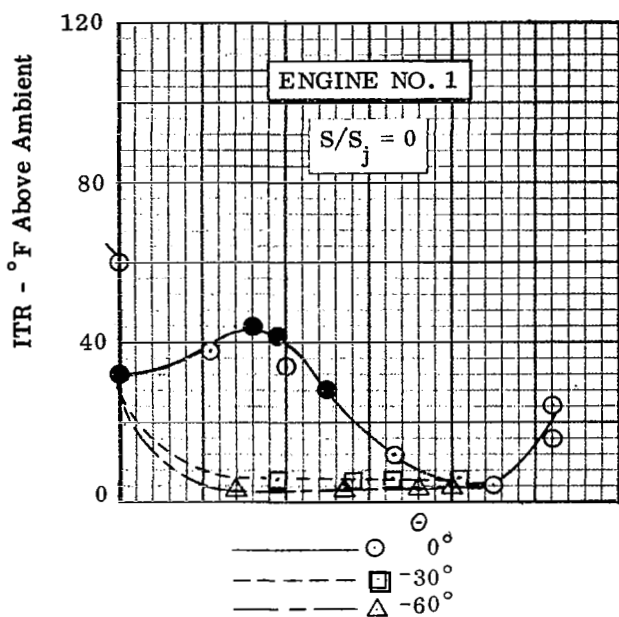
Figure 24. – Variation Of ITR With $V_\infty$ For Dual (circ) Model.
$h/D_e = 2$, EDA = 0, and $\alpha = 0°$.
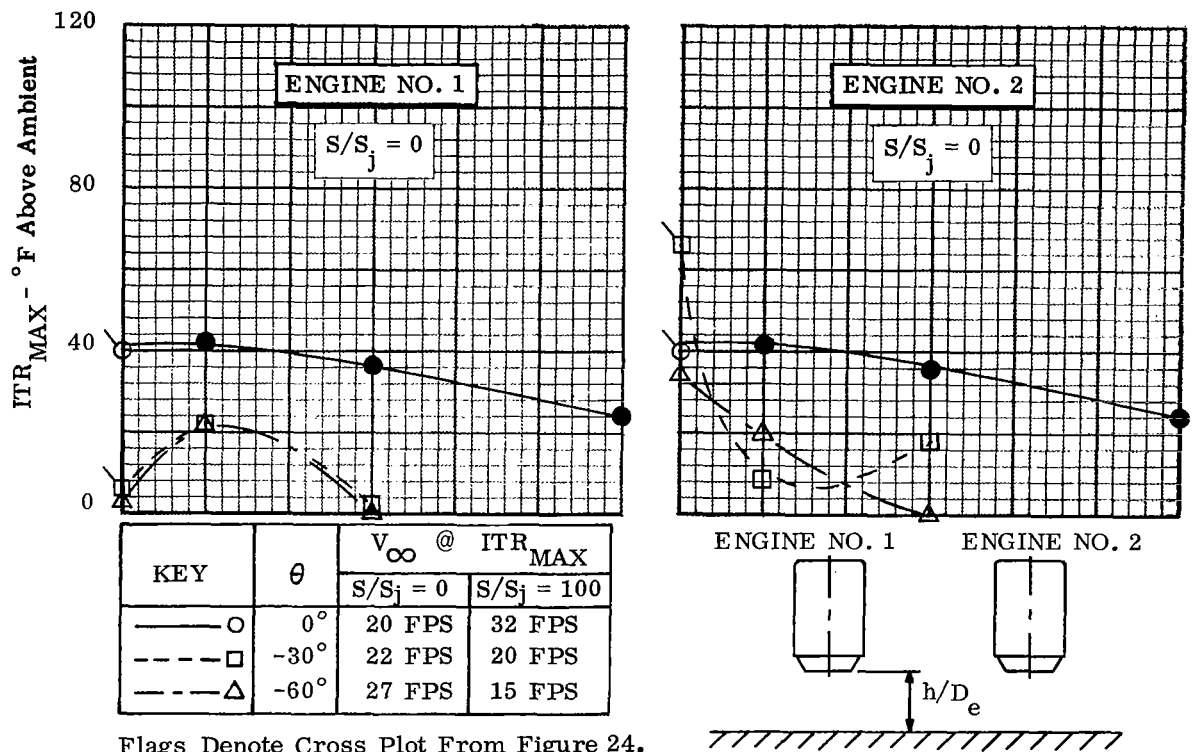
57
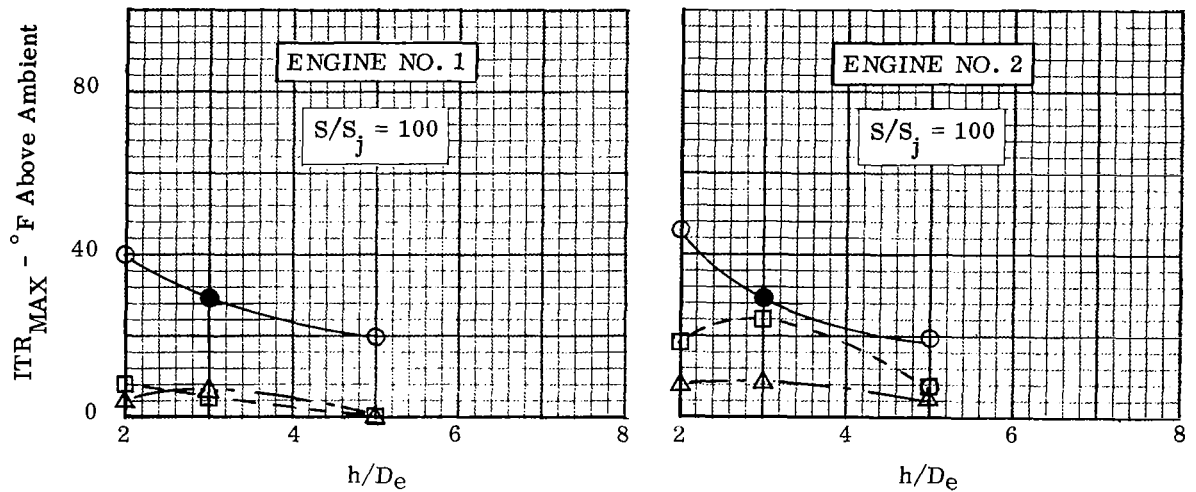
Figure 25. - Variation of $ITR_{MAX}$ With $h/D_e$ For Dual (circ) Model. EDA = 0°, $\alpha$ = 0°, And $V_\infty$ For $ITR_{MAX}$.
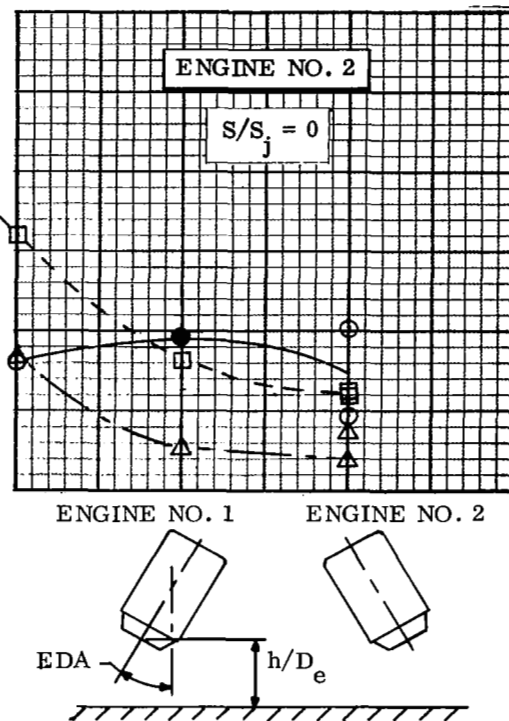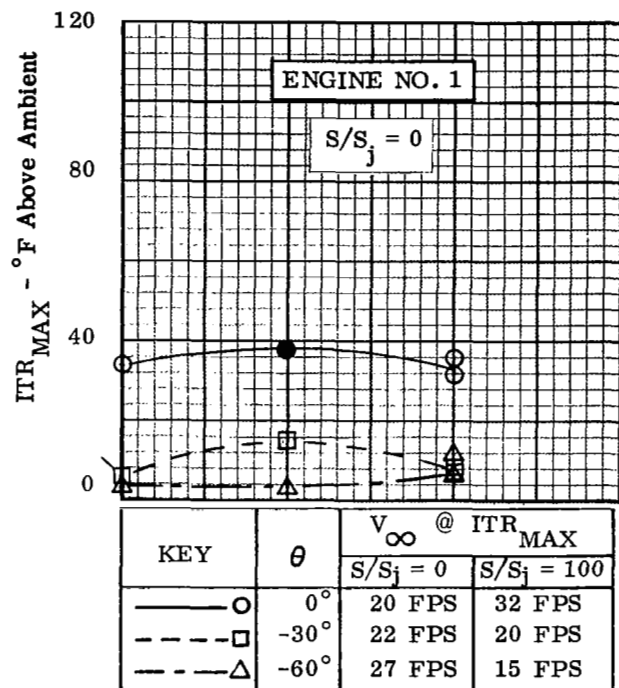
KEY table:

| KEY | $\theta$ | $V_\infty$ @ $ITR_{MAX}$ | |
|---|---|---|---|
| | | $S/S_j = 0$ | $S/S_j = 100$ |
| ──○ | $0°$ | 20 FPS | 32 FPS |
| ────□ | $-30°$ | 22 FPS | 20 FPS |
| ──·──△ | $-60°$ | 27 FPS | 15 FPS |

Flags Denote Cross Plot From Figure 24.

Shaded Symbol Denotes Average of Engine No. 1 and Engine No. 2
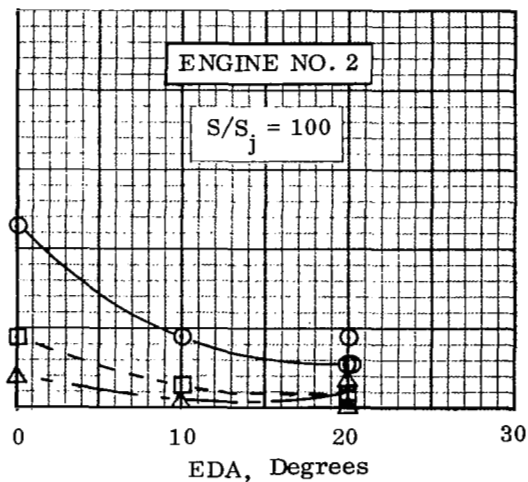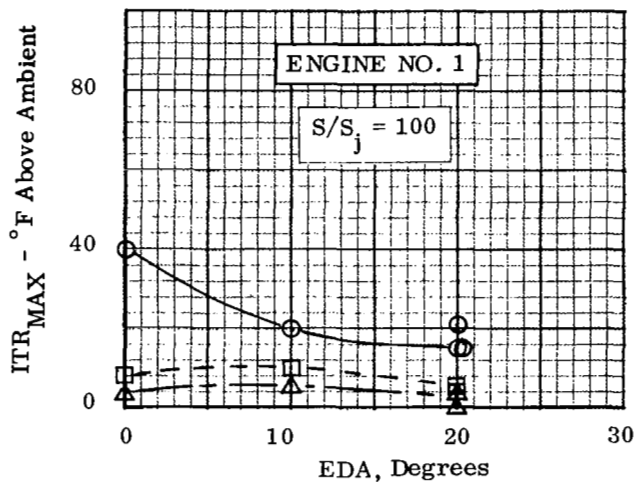
Figure 26. – Variation of $ITR_{MAX}$ With EDA For Dual (circ) Model. $h/D_e = 2$, $\alpha = 0°$, And $V_\infty$ For $ITR_{MAX}$.
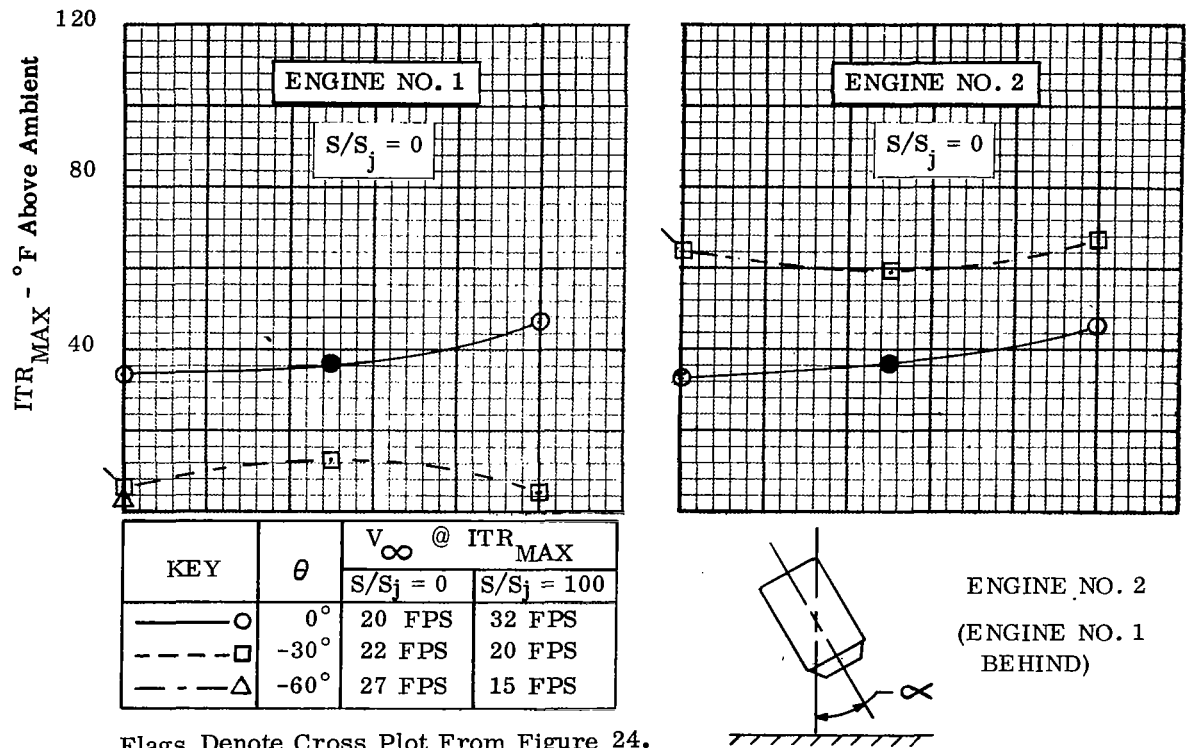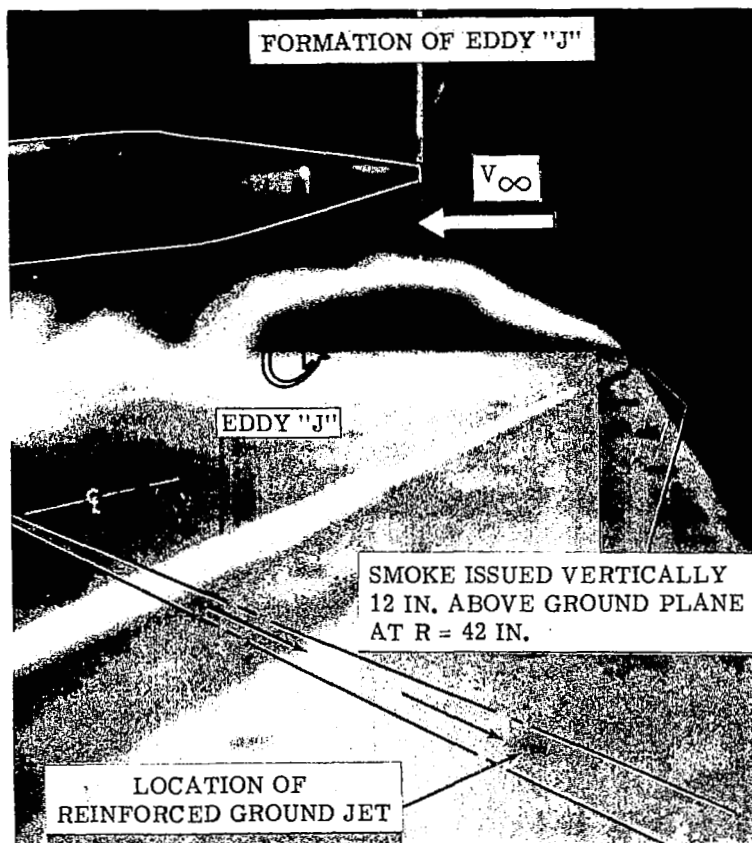
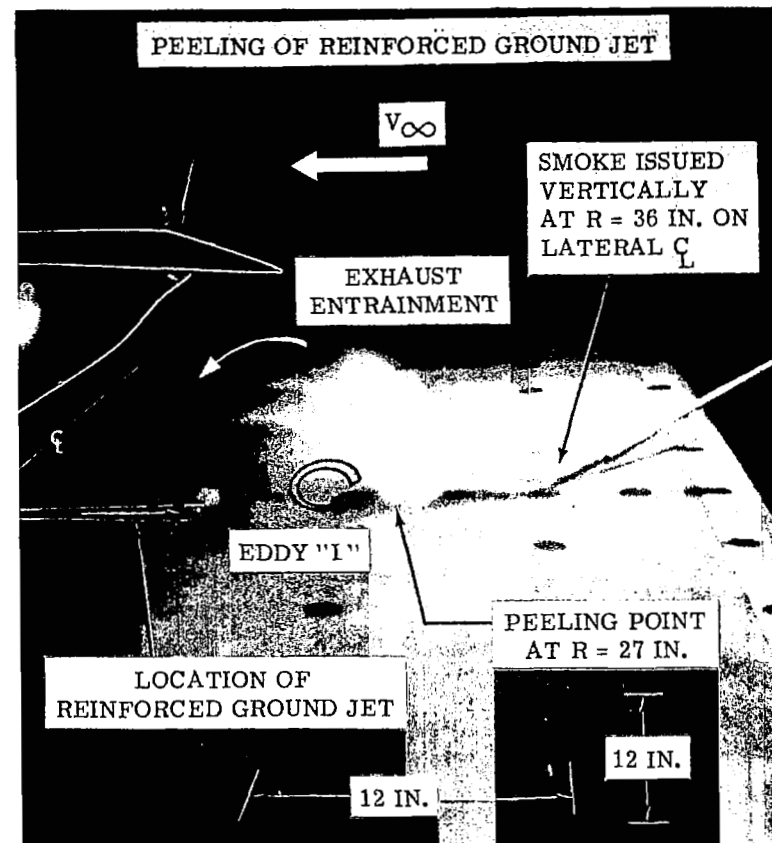| KEY | $\theta$ | $V_\infty$ @ ITR$_{MAX}$ | |
|---|---|---|---|
| | | $S/S_j = 0$ | $S/S_j = 100$ |
| ——○ | 0° | 20 FPS | 32 FPS |
| ----□ | -30° | 22 FPS | 20 FPS |
| —·—△ | -60° | 27 FPS | 15 FPS |

ENGINE NO. 2

(ENGINE NO. 1 BEHIND)

Flags Denote Cross Plot From Figure 24.
Shaded Symbol Denotes Average of Engine No. 1 and Engine No. 2
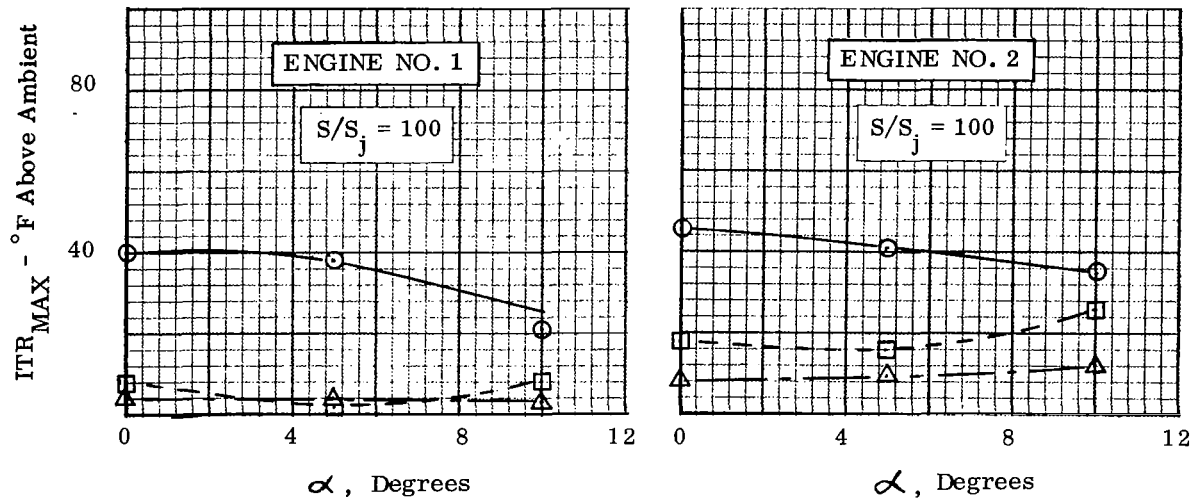
Figure 27. - Variation Of ITR$_{MAX}$ With $\alpha$ For Dual (circ) Model.

h/D$_e$ = 2, EDA = 0°, And V$_\infty$ For ITR$_{MAX}$.

60

PEELING LINE

(i)  PEELING POINT EDDY
(J)  EDDY TRAPPED UNDER WING
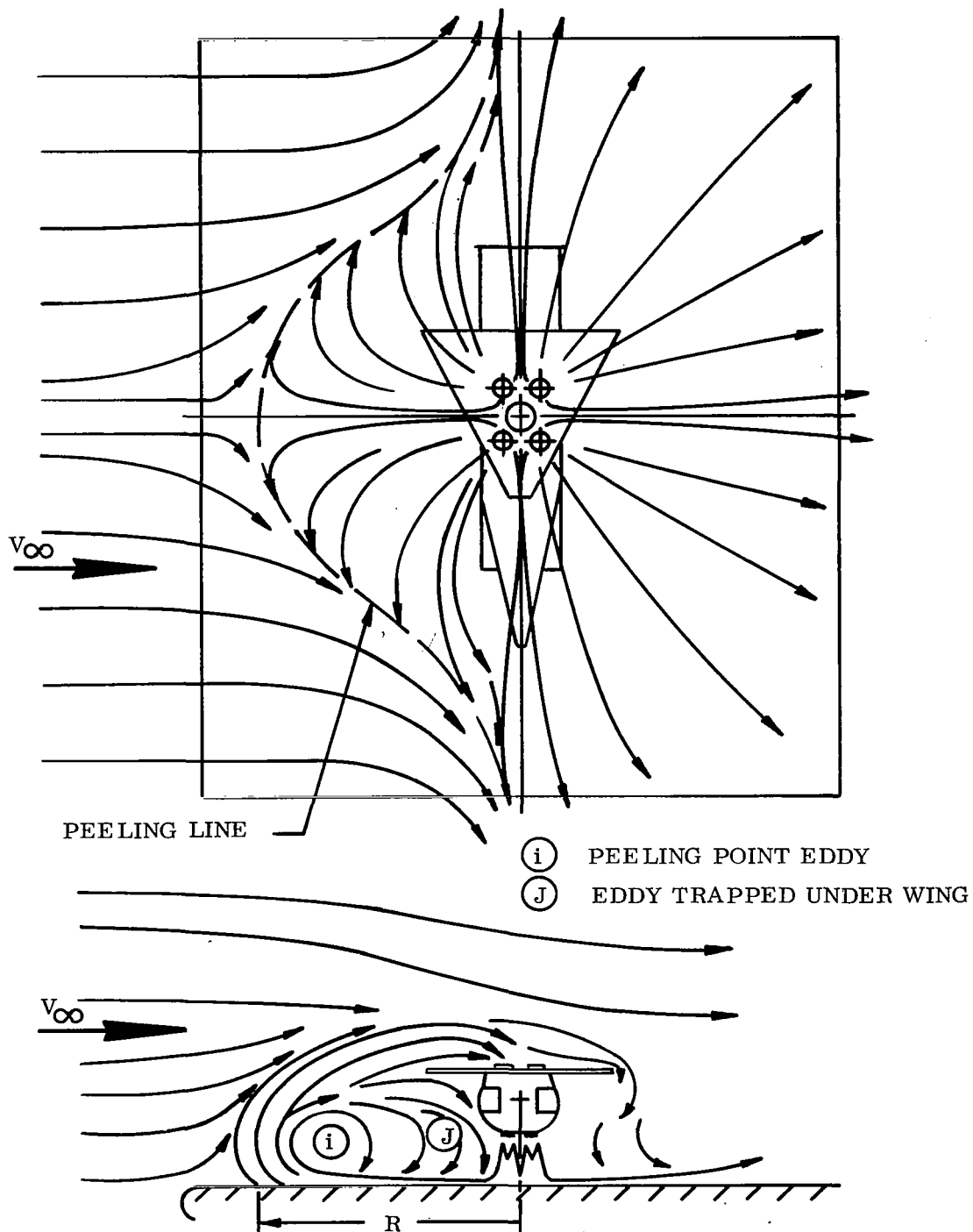
FIGURE 28. - EFFECT OF WIND ON RECIRCULATION.

61

Top Inlets, $S/S_j = 43$, $h/D_e = 5$,
$V_\infty = 29$ FPS, $\theta = 45°$
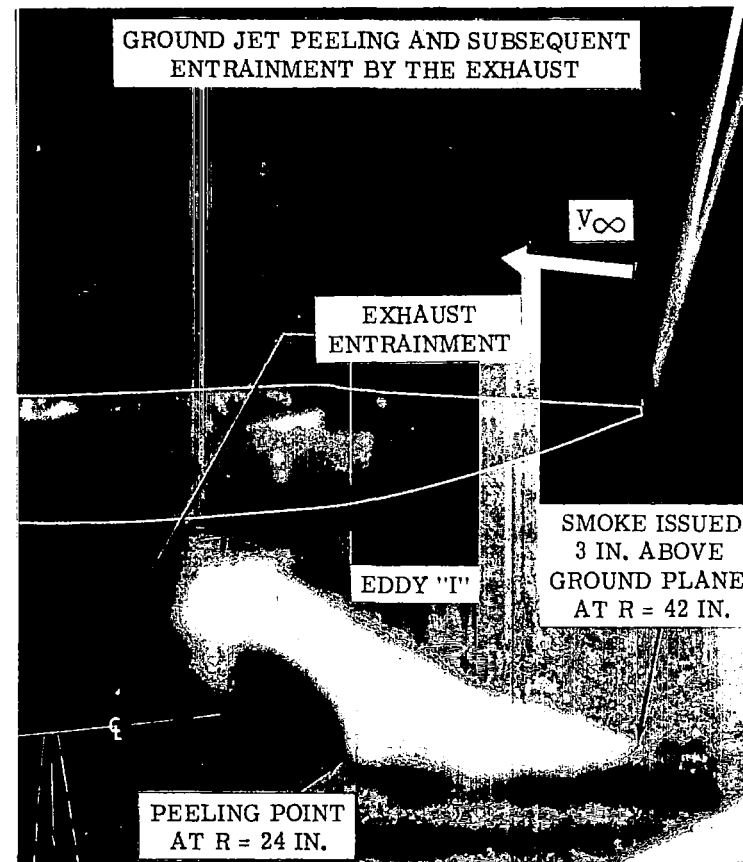
Top Inlets, $S/S_j = 86$, $h/D_e = 3$,
$V_\infty = 39$ FPS, $\theta = 90°$

(a) Top Inlet Configuration

Figure 29. - Examples of Ground Jet Peeling.

GROUND JET PEELING AND SUBSEQUENT
ENTRAINMENT BY THE EXHAUST

$V_\infty$

SMOKE ISSUED ON
GROUND PLANE AT R = 36 IN.

SIDE
INLETS

EDDY "I"

EXHAUST
ENTRAINMENT

PEELING POINT AT R = 21 IN.

LOCATION OF
REINFORCED GROUND JET
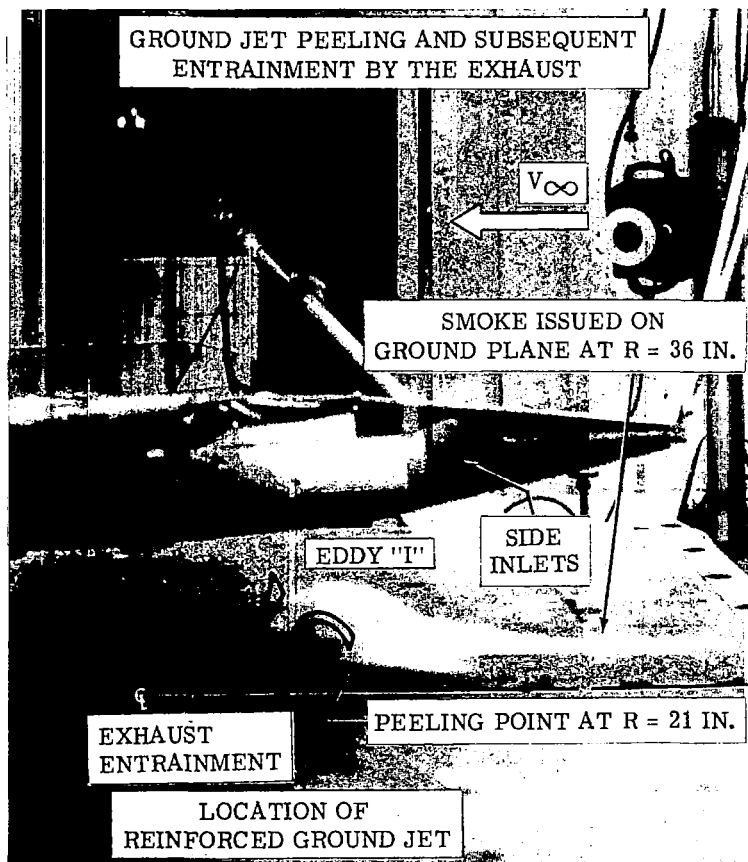
Side Inlets, $S/S_j$ = 43, $h/D_e$ = 3,

$V_\infty$ = 39 FPS, $\theta = 0°$

GROUND JET PEELING AND SUBSEQUENT
ENTRAINMENT BY THE EXHAUST

$V_\infty$

EXHAUST
ENTRAINMENT

SMOKE ISSUED
3 IN. ABOVE
GROUND PLANE
AT R = 42 IN.

EDDY "I"

PEELING POINT
AT R = 24 IN.

Side Inlets, $S/S_j$ = 43, $h/D_e$ = 3,

$V_\infty$ = 23 FPS, $\theta = 45°$

(b) Side Inlet Configuration

Figure 29. - Concluded.

63
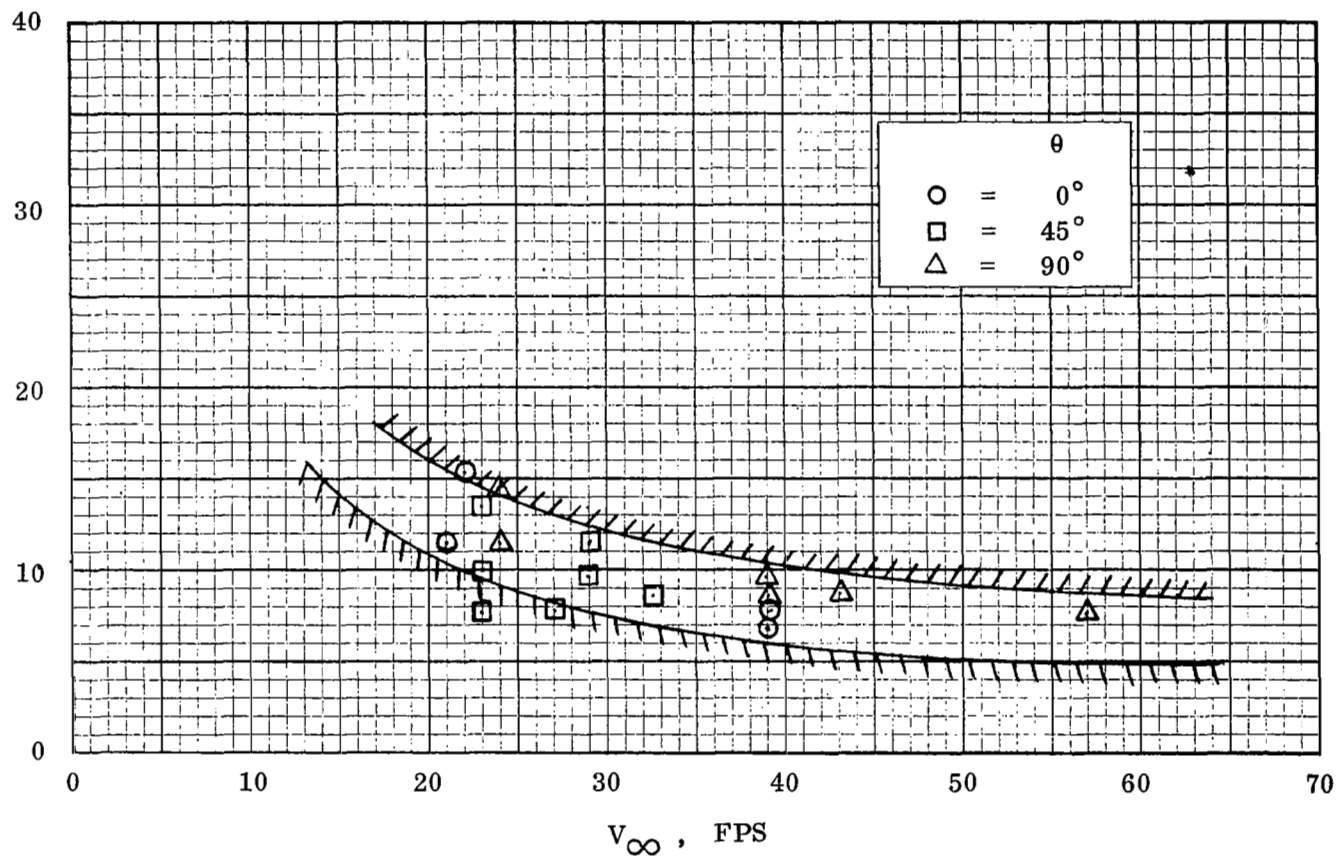
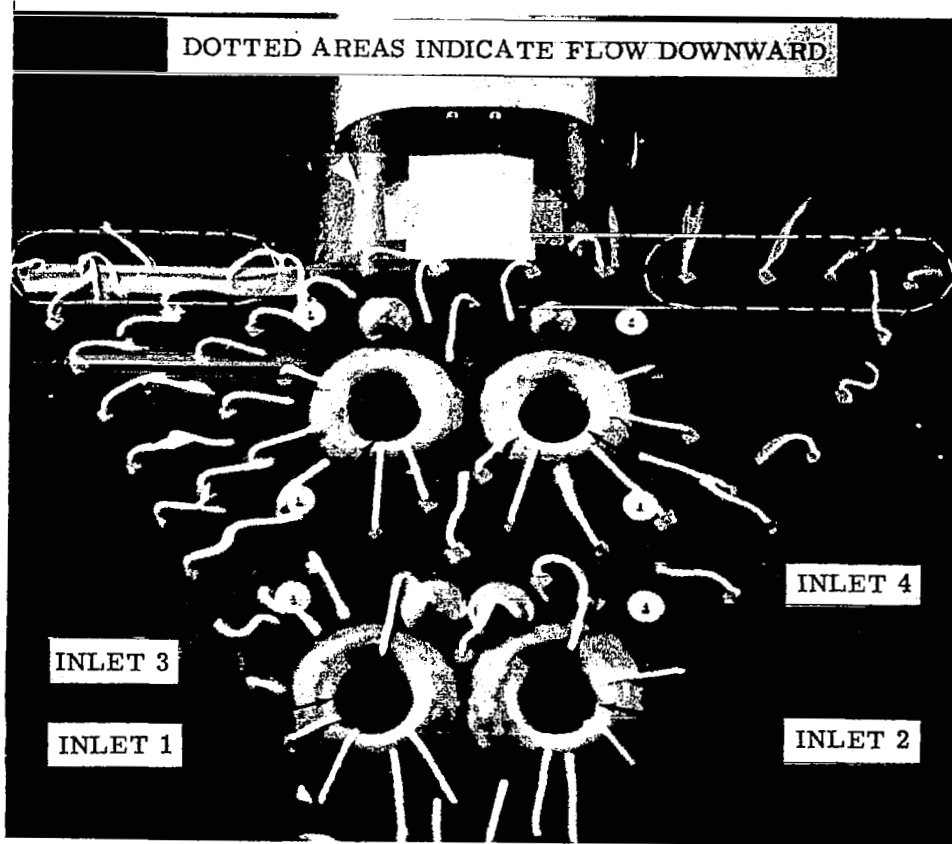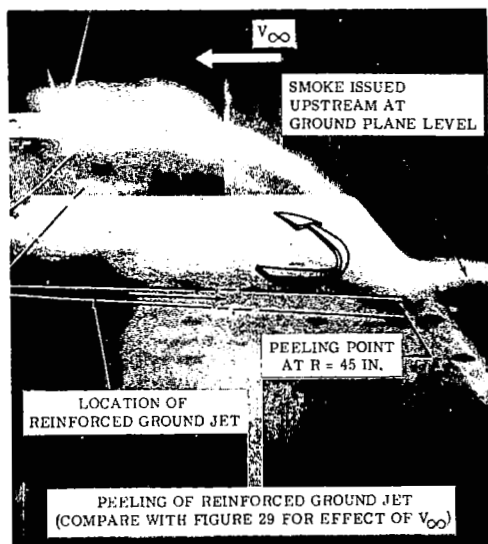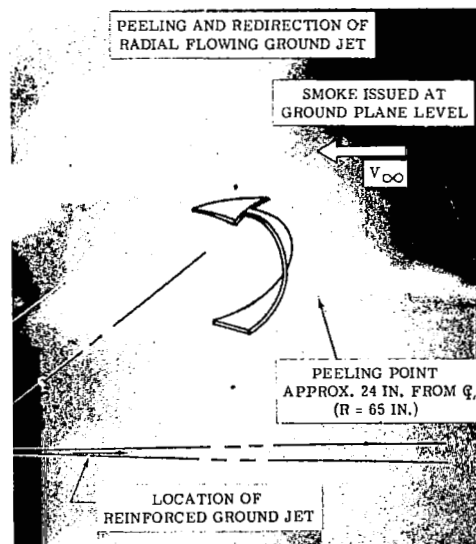Figure 30. – Variation Of Ground Jet Peeling Radius With $V_\infty$ For Scaled NASA Model.

Figure 31. - Wing Upper Surface Flow Characteristics of Top Inlet Configuration.
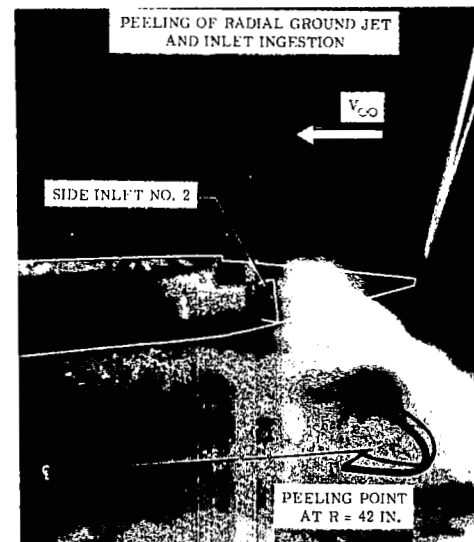$h/D_e = 3$, $V_\infty = 0$, $S/S_j = 86$.
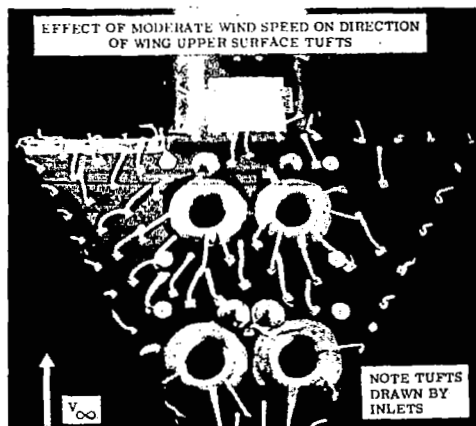
Top Inlets, $V_\infty$ = 24 FPS,
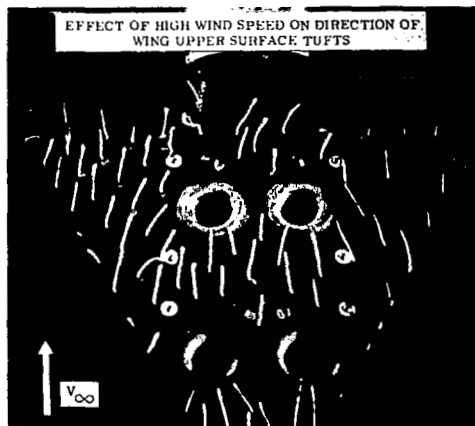$\theta$ = 90°

Side Inlets, $V_\infty$ = 26 FPS,
$\theta$ = 90°

Side Inlets, $V_\infty$ = 23 FPS,
$\theta$ = 45°

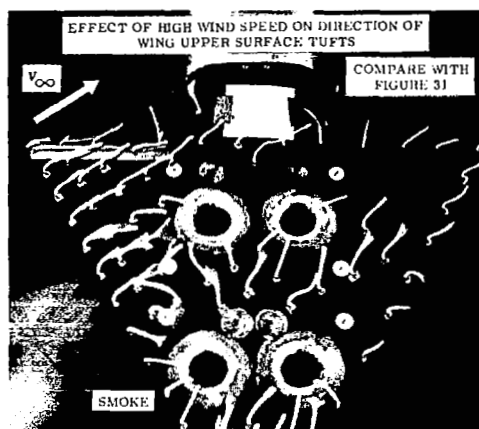Figure 32. - Examples of Recirculation From the Peeled Ground Jets.
$S/S_j$ = 43, $h/D_e$ = 3.

$V_{\infty} = 24$ FPS, $\theta = 0^{\circ}$



$V_{\infty} = 51$ FPS, $\theta = 0^{\circ}$

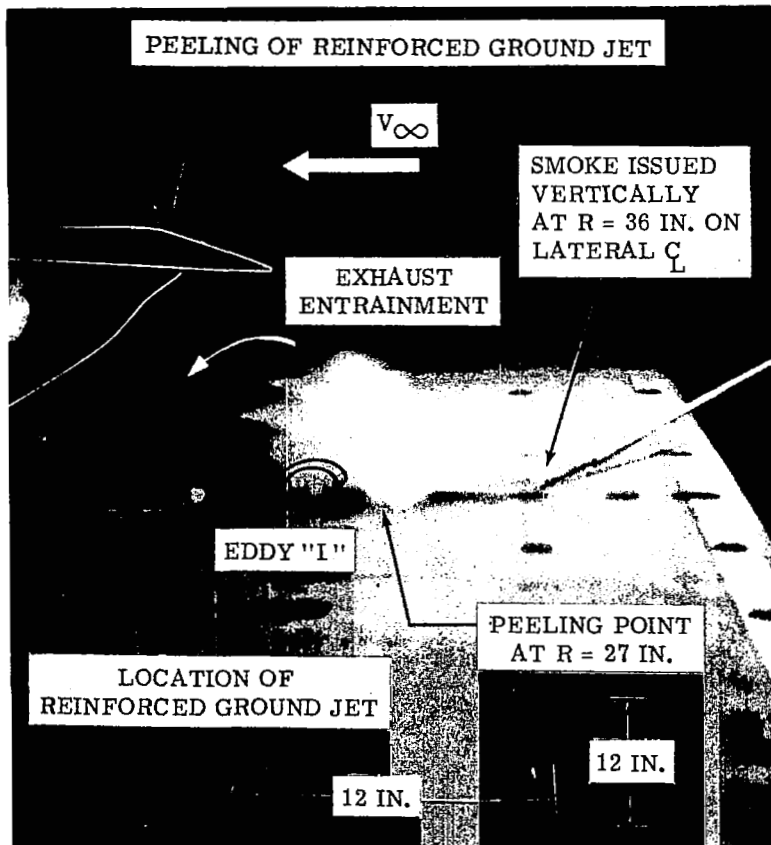Influence of Wind Speed on Tufts, $S/S_j = 43$, $h/D_e = 1.2$



$V_{\infty} = 27$ FPS, $\theta = 45^{\circ}$

Tufts Directed By Wind and Smoke Blown Back Under Model
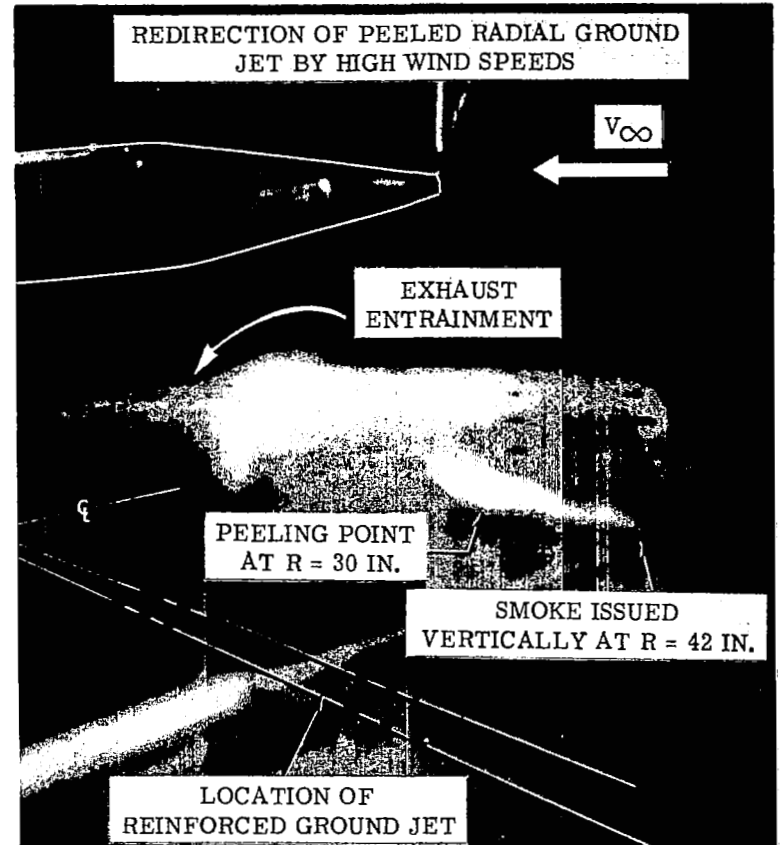$S/S_j = 43$, $h/D_e = 3$

(a) Wing Upper Surface Tufts

Figure 33. - Effect of High Wind Speed On Recirculation Flow
Characteristics of Top Inlet Configuration .

67

Examples of Smoke Blown Back Underneath
Model Due to High Wind Speed

PEELING OF REINFORCED GROUND JET

$V_\infty$

SMOKE ISSUED
VERTICALLY
AT R = 36 IN. ON
LATERAL $C_L$

EXHAUST
ENTRAINMENT

EDDY "I"

LOCATION OF
REINFORCED GROUND JET

PEELING POINT
AT R = 27 IN.

12 IN.

12 IN.

REDIRECTION OF PEELED RADIAL GROUND
JET BY HIGH WIND SPEEDS

$V_\infty$

EXHAUST
ENTRAINMENT

$C_L$

PEELING POINT
AT R = 30 IN.

SMOKE ISSUED
VERTICALLY AT R = 42 IN.

LOCATION OF
REINFORCED GROUND JET

$S/S_j = 86$,  $h/D_e = 3$,  $V_\infty = 39$ FPS, $\theta = 90°$

$S/S_j = 43$,  $h/D_e = 5$,  $V_\infty = 29$ FPS, $\theta = 45°$
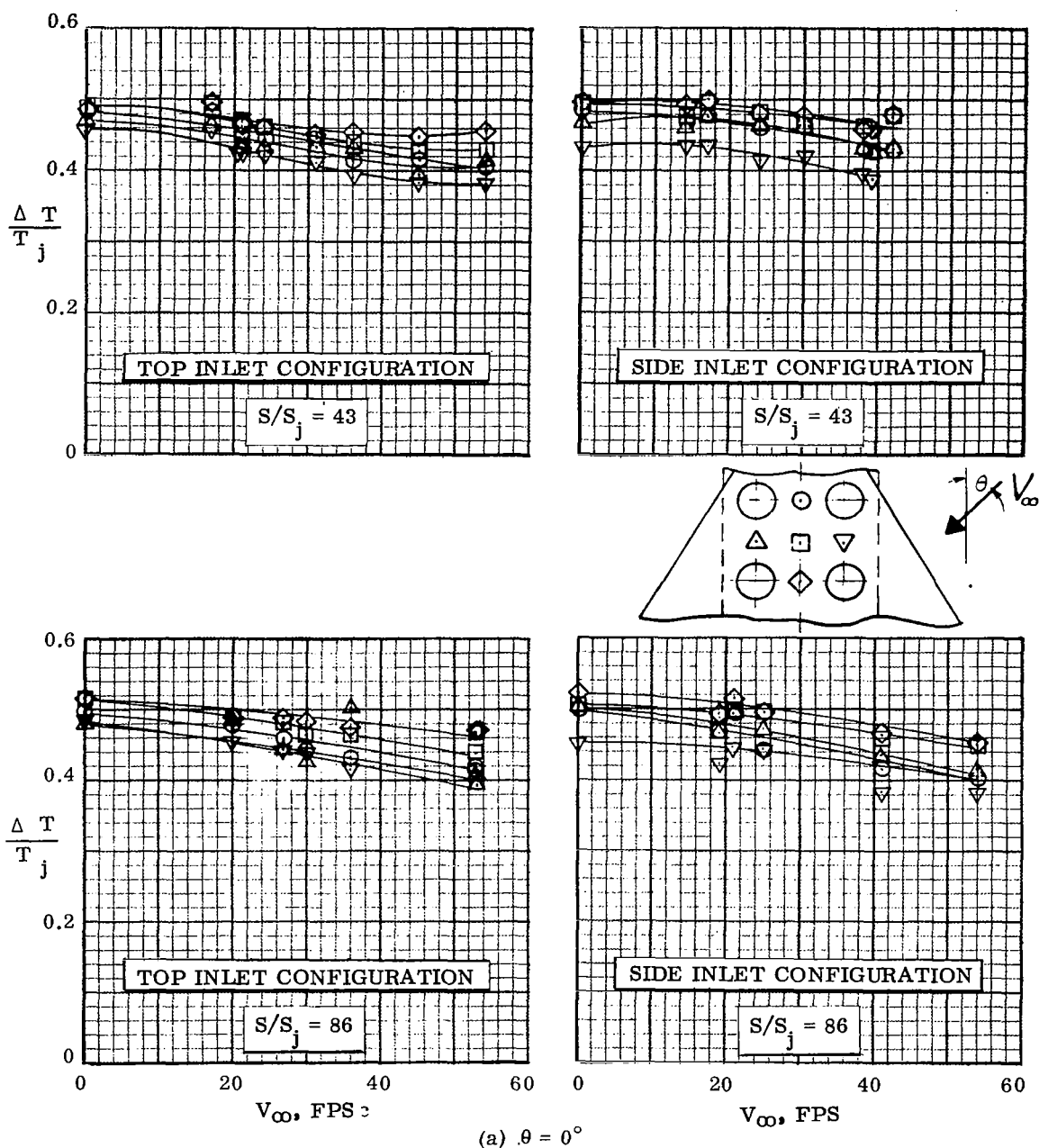
(b)  Ground Jet Smoke Pattern

Figure 33. - Concluded.
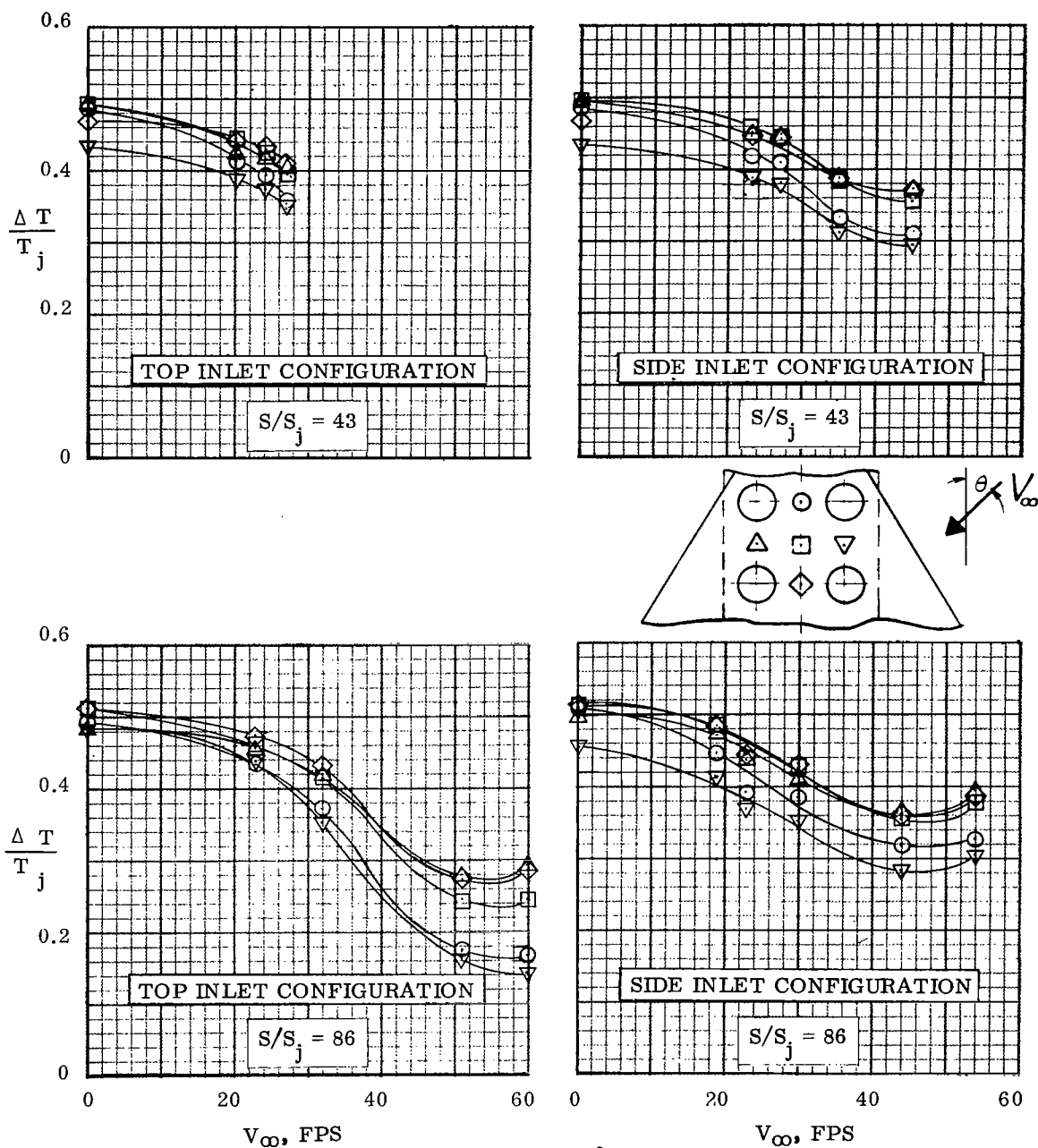
Figure 34. – Variation Of Fuselage Temperature With $V_\infty$ At $h/D_e = 3$, Scaled NASA Model.

69

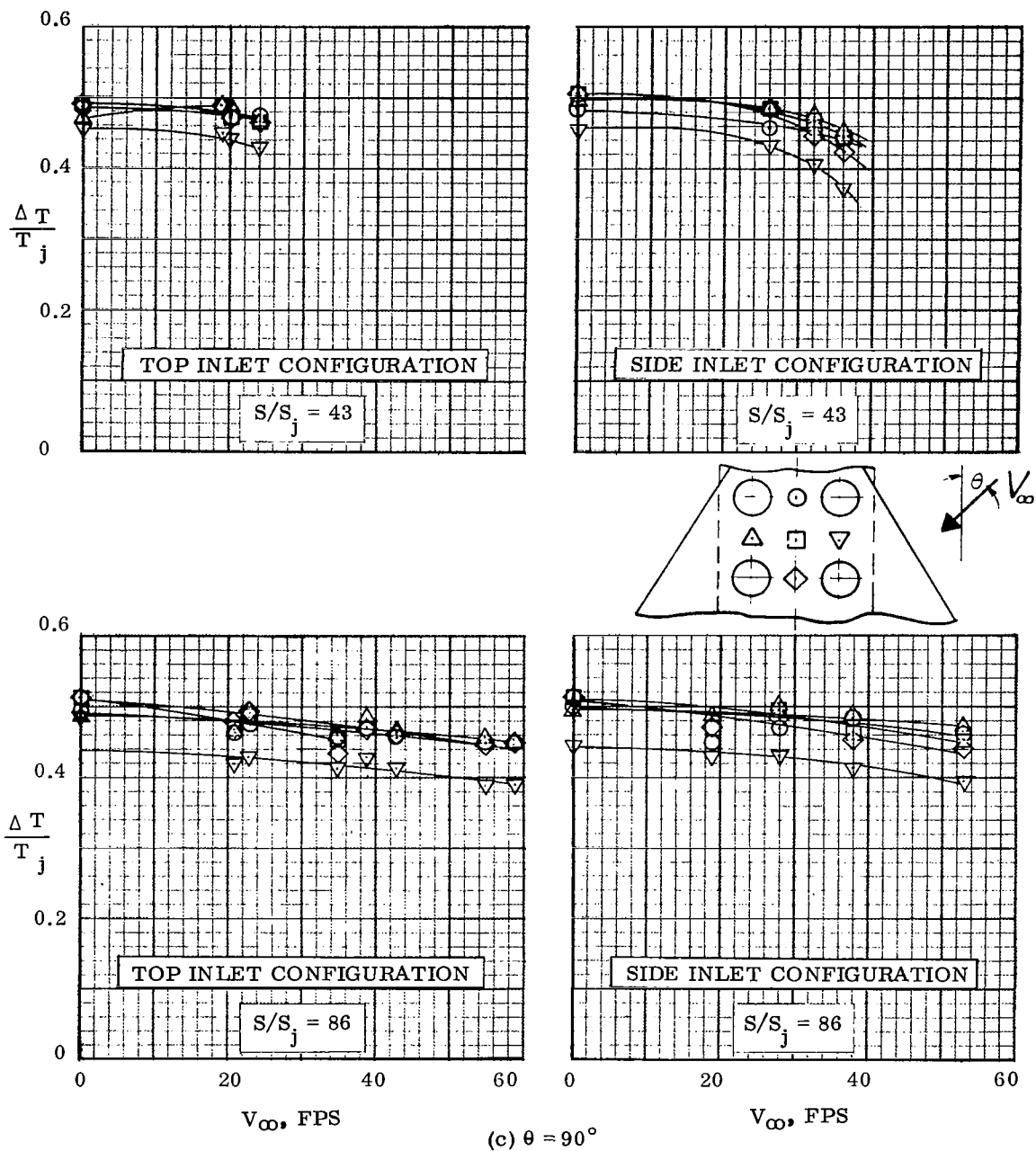(b) θ = 45°

Figure 34.-Continued.

70

(c) $\theta = 90°$

Figure 34. – Concluded.

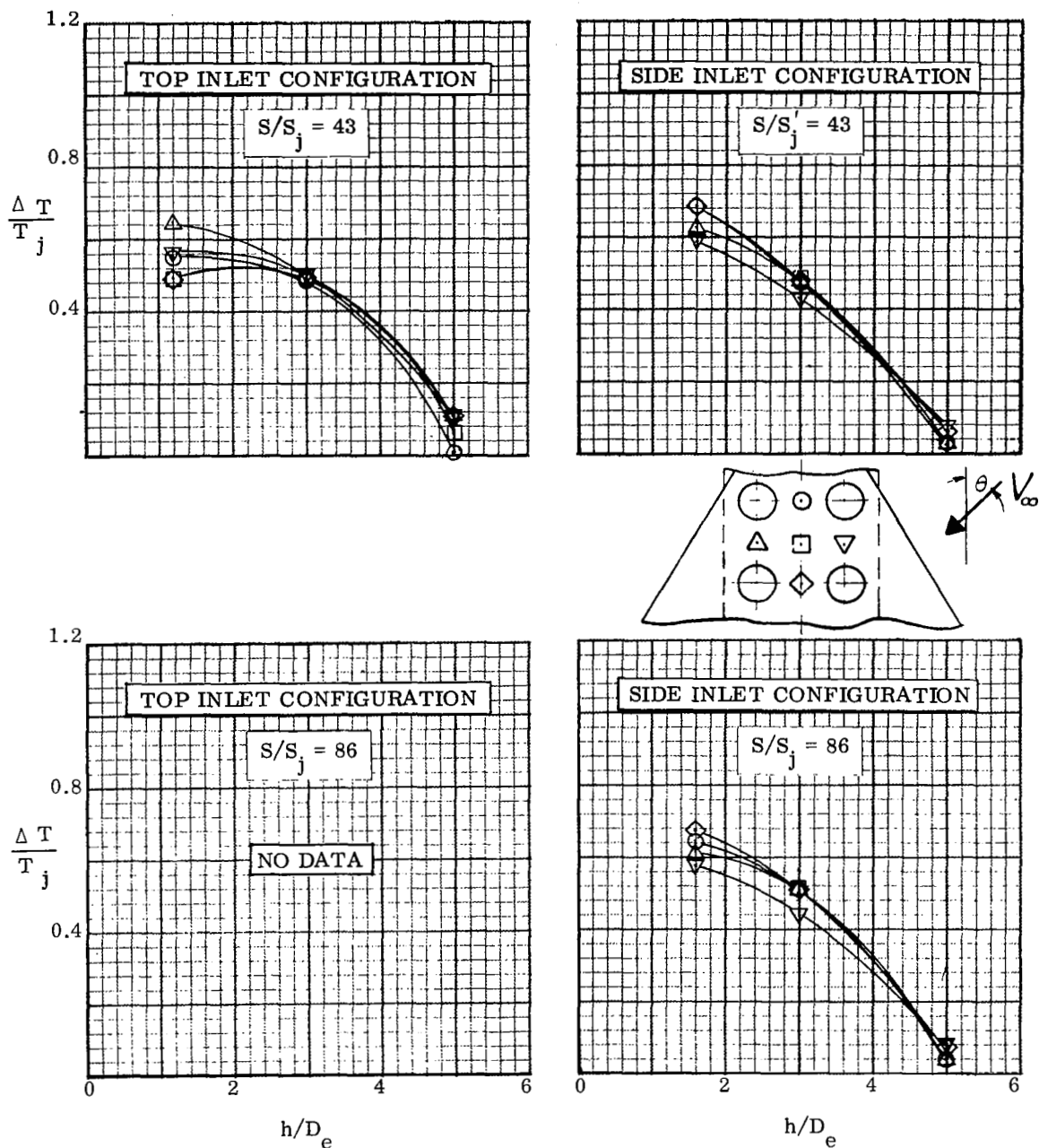Figure 35. – Variation Of Fuselage Temperature With $h/D_e$ For $V_\infty$ = 0, Scaled NASA Model.
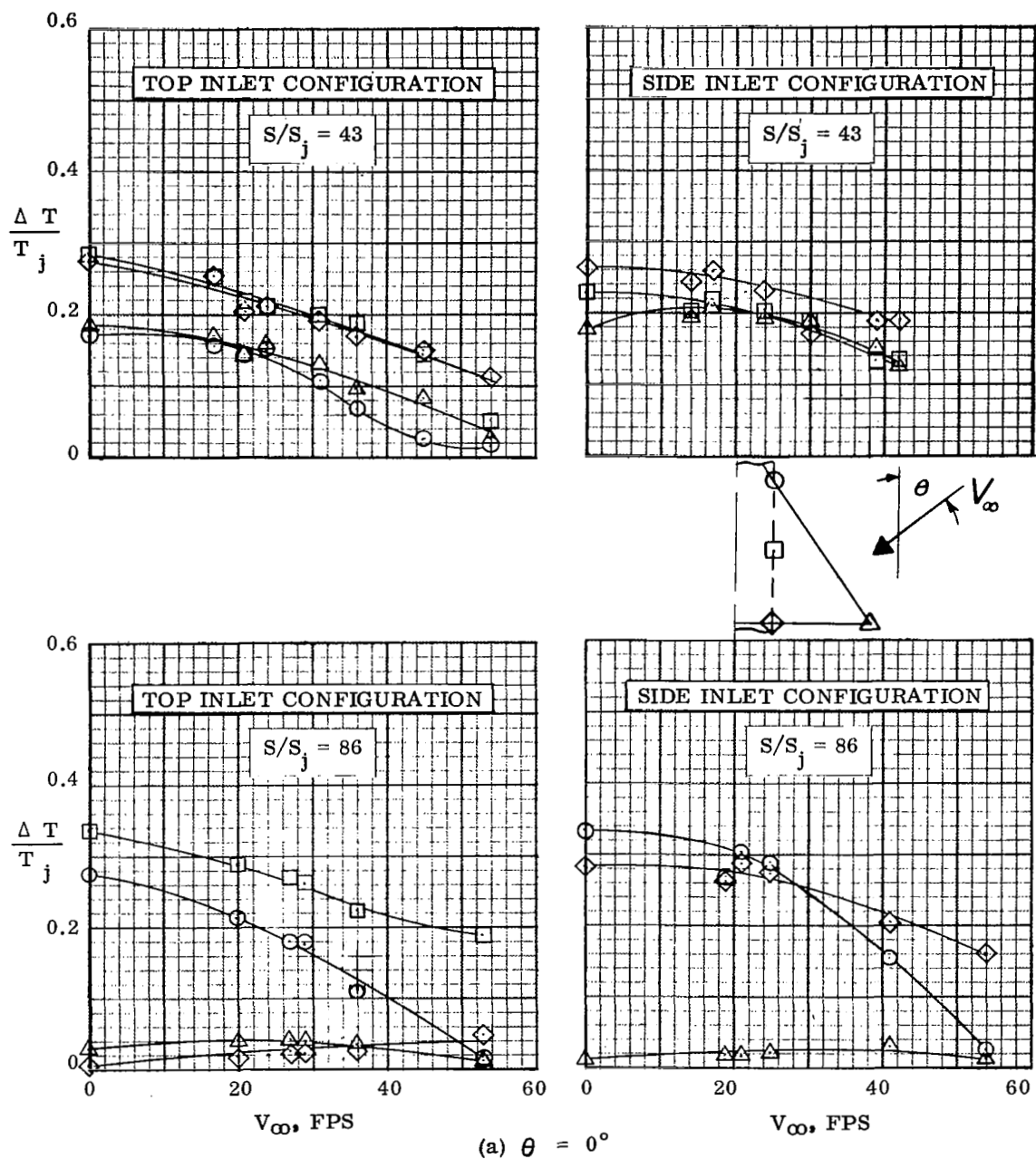
Figure 36. – Variation Of Wing Temperature With $V_\infty$ At $h/D_e = 3$, Scaled NASA Model.

(a) $\theta = 0°$

(b) $\theta = 45°$
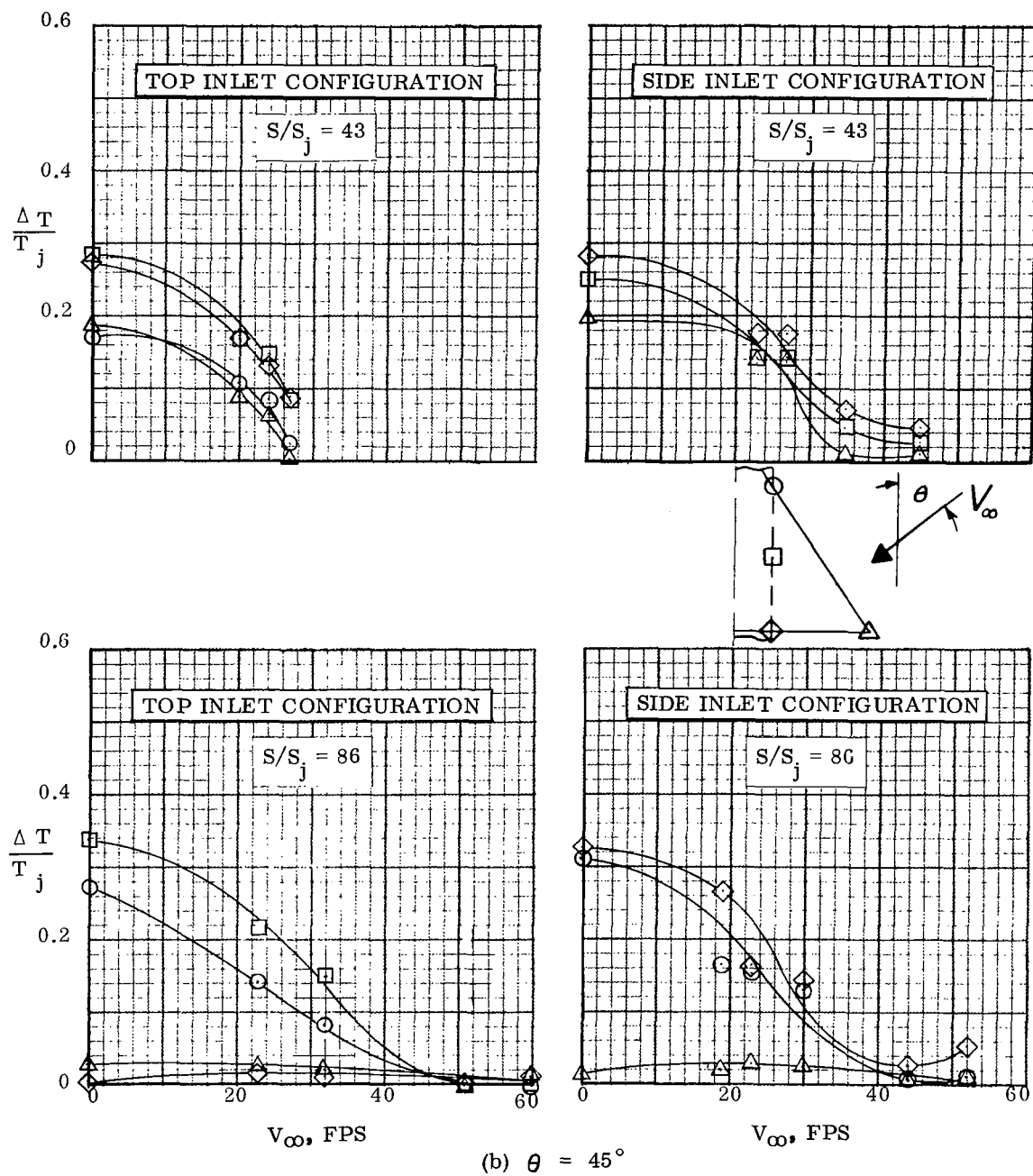
Figure 36.–Continued.

74
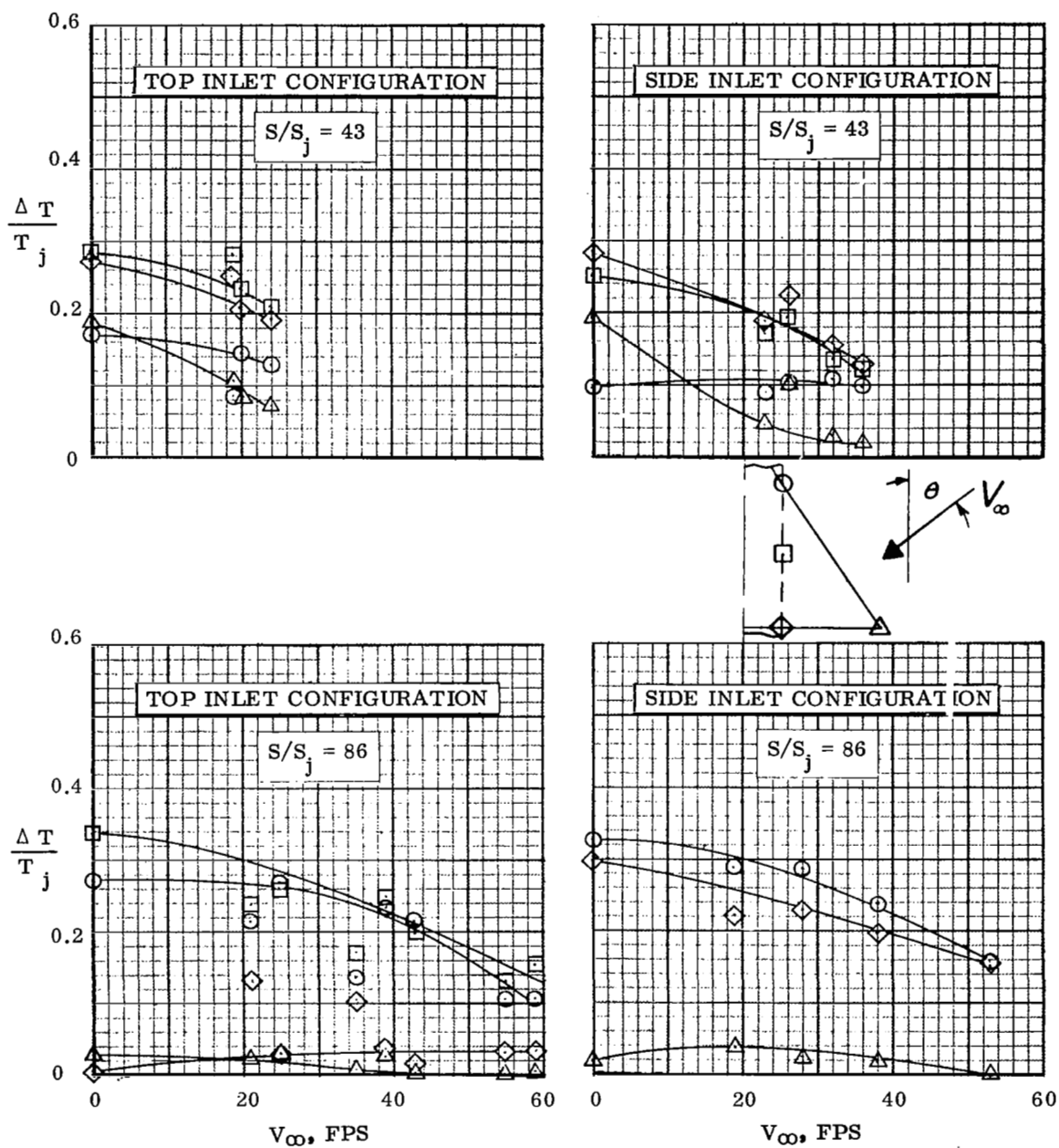
(c) $\theta = 90°$

Figure 36. - Concluded.
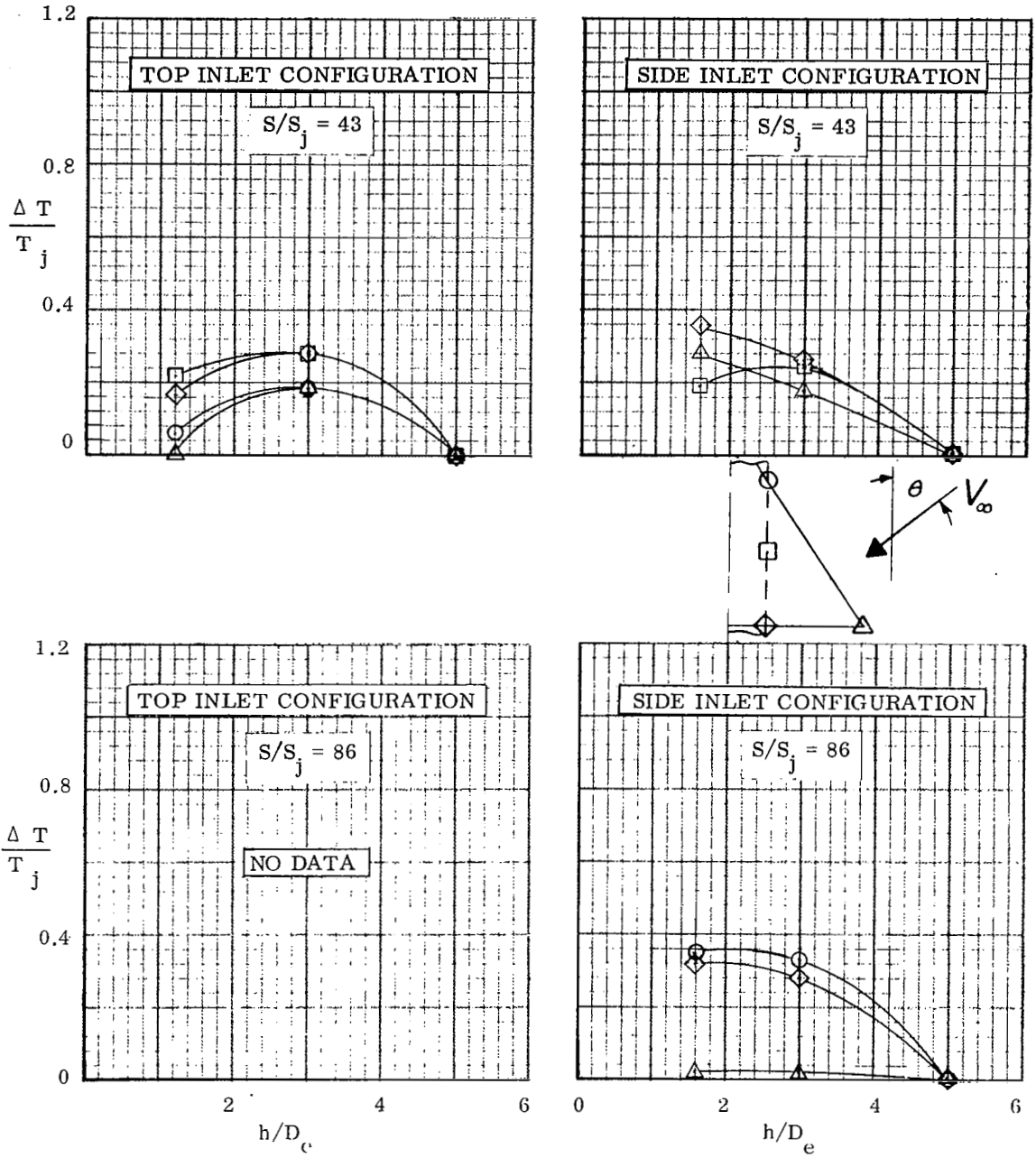
Figure 37. – Variation of Wing Temperature with $h/D_e$ at $V_\infty = 0$, Scaled NASA Model.

76
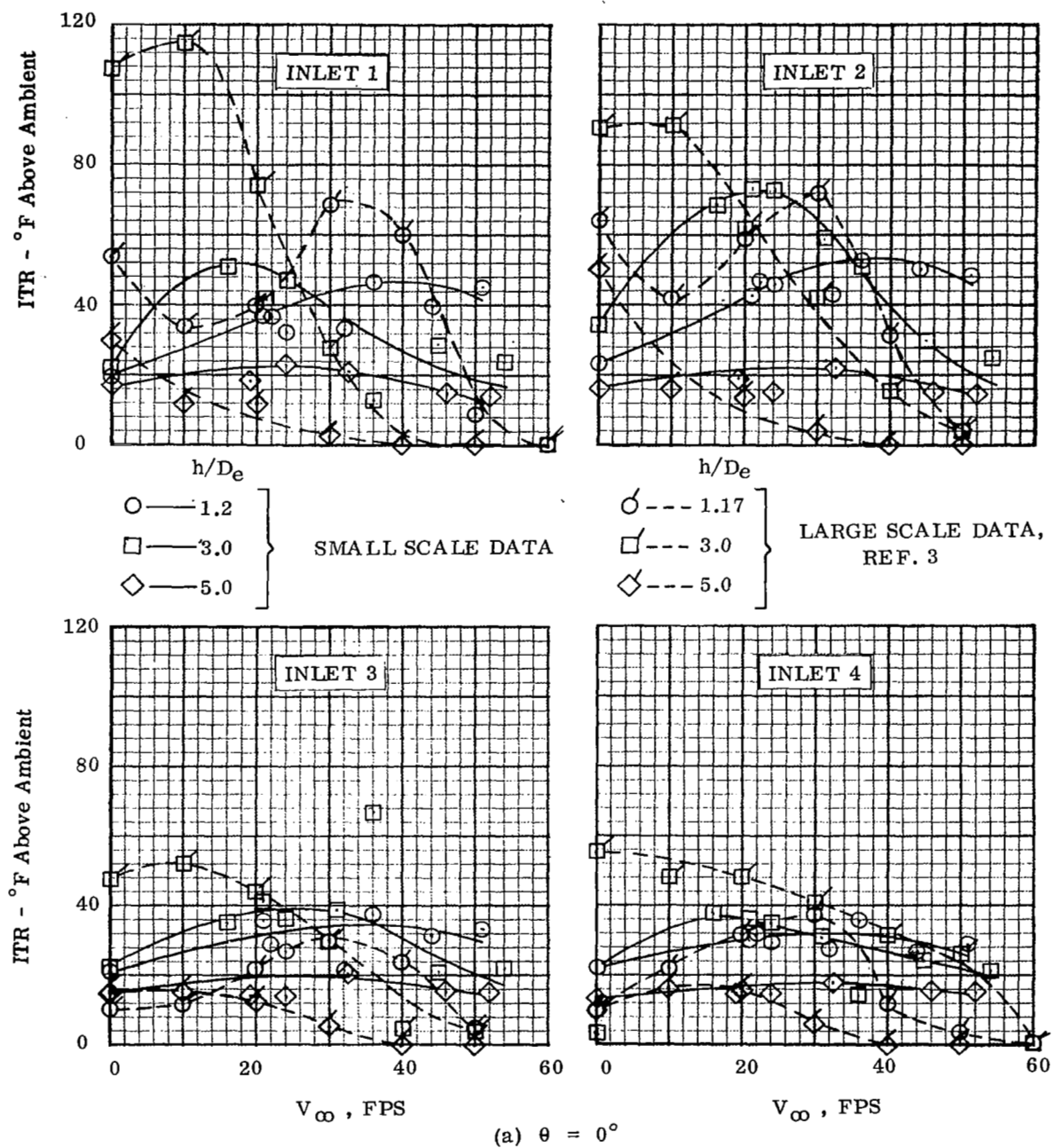
Figure 38. – Variation Of ITR With $V_\infty$ For The Top Inlet Configuration. $S/S_j = 43$.

77
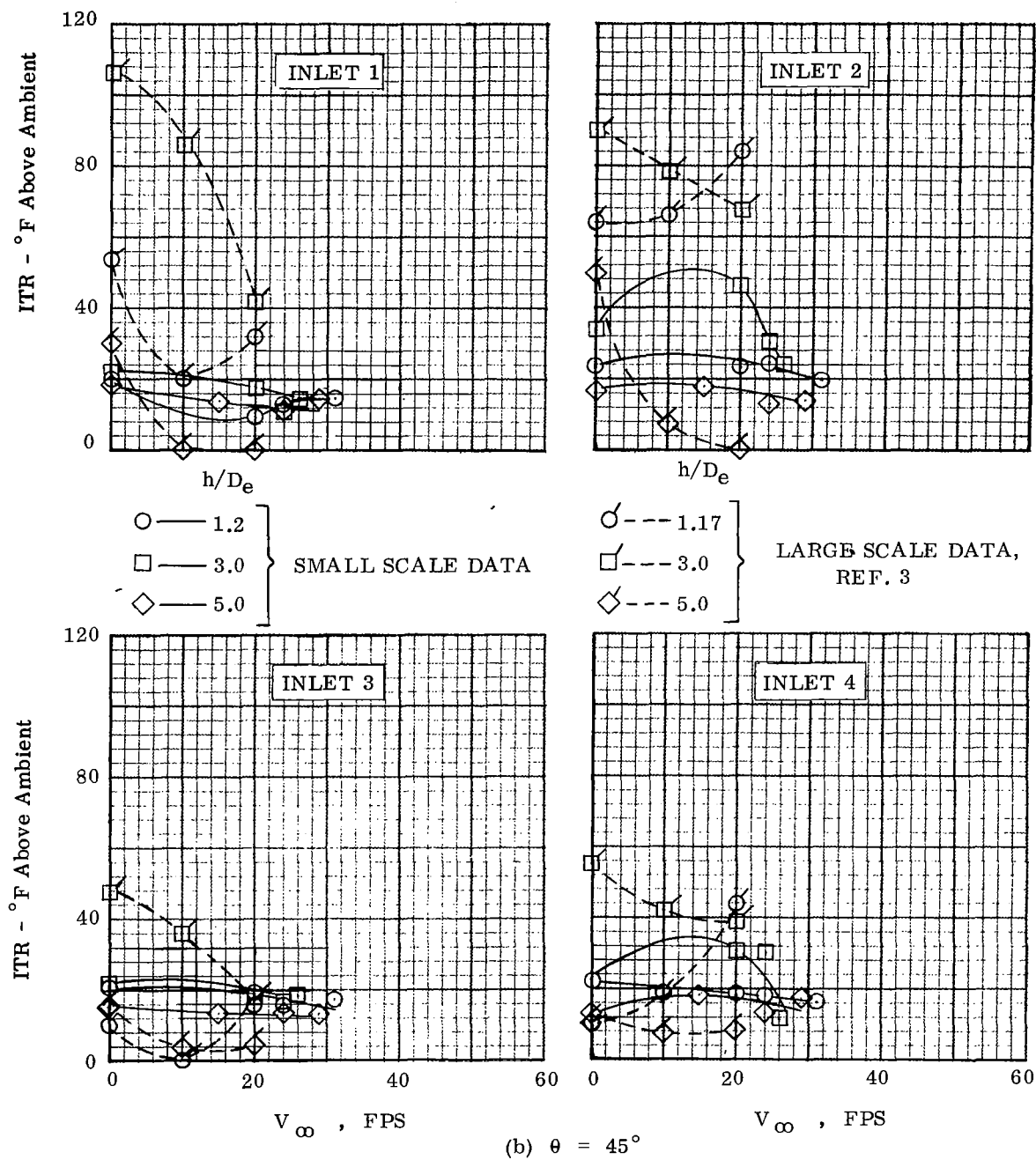
Figure 38. - Continued.

(c) θ = 90°
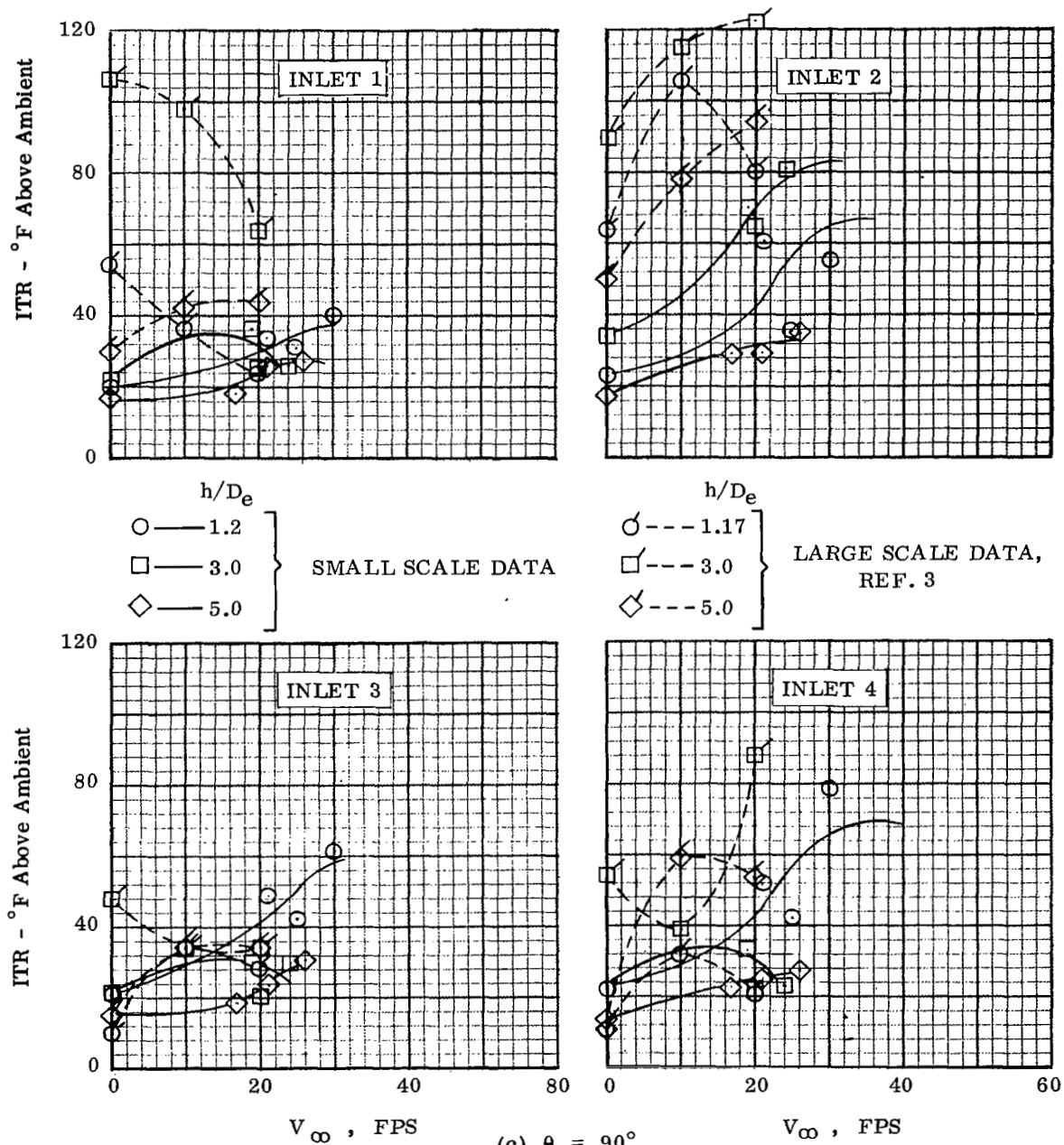
Figure 38. - Concluded.
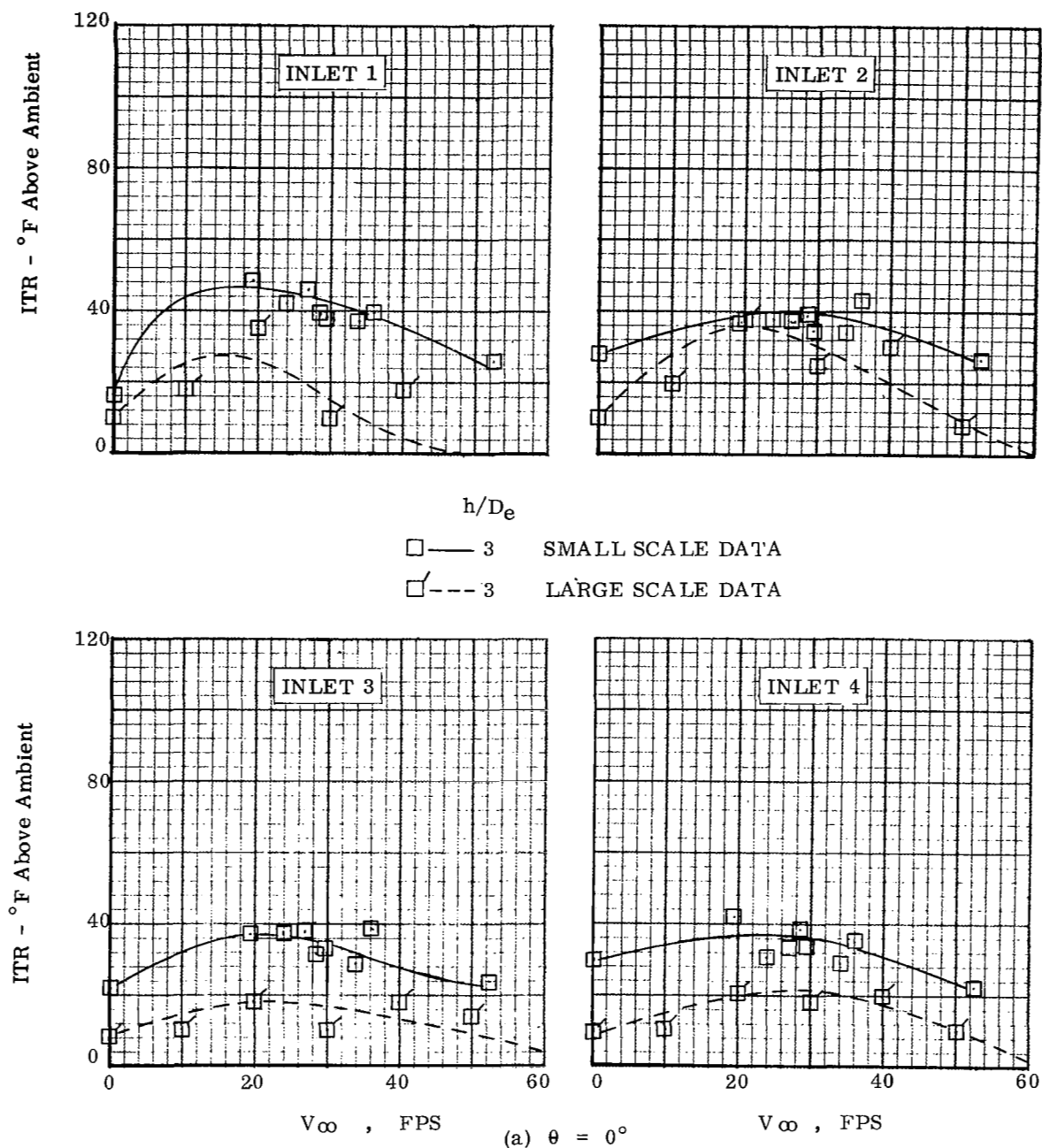
Figure 39. – Variation Of ITR With $V_\infty$ For The Top Inlet
Configuration. $S/S_j = 86$.

$$h/D_e$$

□——— 3    SMALL SCALE DATA

□---- 3    LARGE SCALE DATA

$V_\infty$ , FPS        (b)  $\theta$  = 45°        $V_\infty$ , FPS

Figure 39. - Continued.

81

Figure 39. - Concluded.

## h/D_e

- ○ —— 1.6
- □ —— 3.0      } SMALL SCALE DATA
- ◇ —— 5.0

- ● --- 1.6 *   } LARGE SCALE DATA
- ■ --- 3.0     *      INTERPOLATED
- ◆ --- 5.0     }        VALUES

INLET 1

INLET 2

ITR - °F ABOVE AMBIENT

V_∞ , FPS

(a)  θ = 0°

Figure 40. - Variation Of ITR With $V_\infty$ For The Side Inlet Configuration $S/S_j = 43$.

(b)  $\theta = 45°$

h/D$_e$

SMALL SCALE DATA
○ —— 1.6
□ —— 3.0
◇ —— 5.0

h/D$_e$

LARGE SCALE DATA
● --- 1.6 *
■ --- 3.0
● --- 5.0
* INTERPOLATED VALUES

(c)  $\theta = 90°$
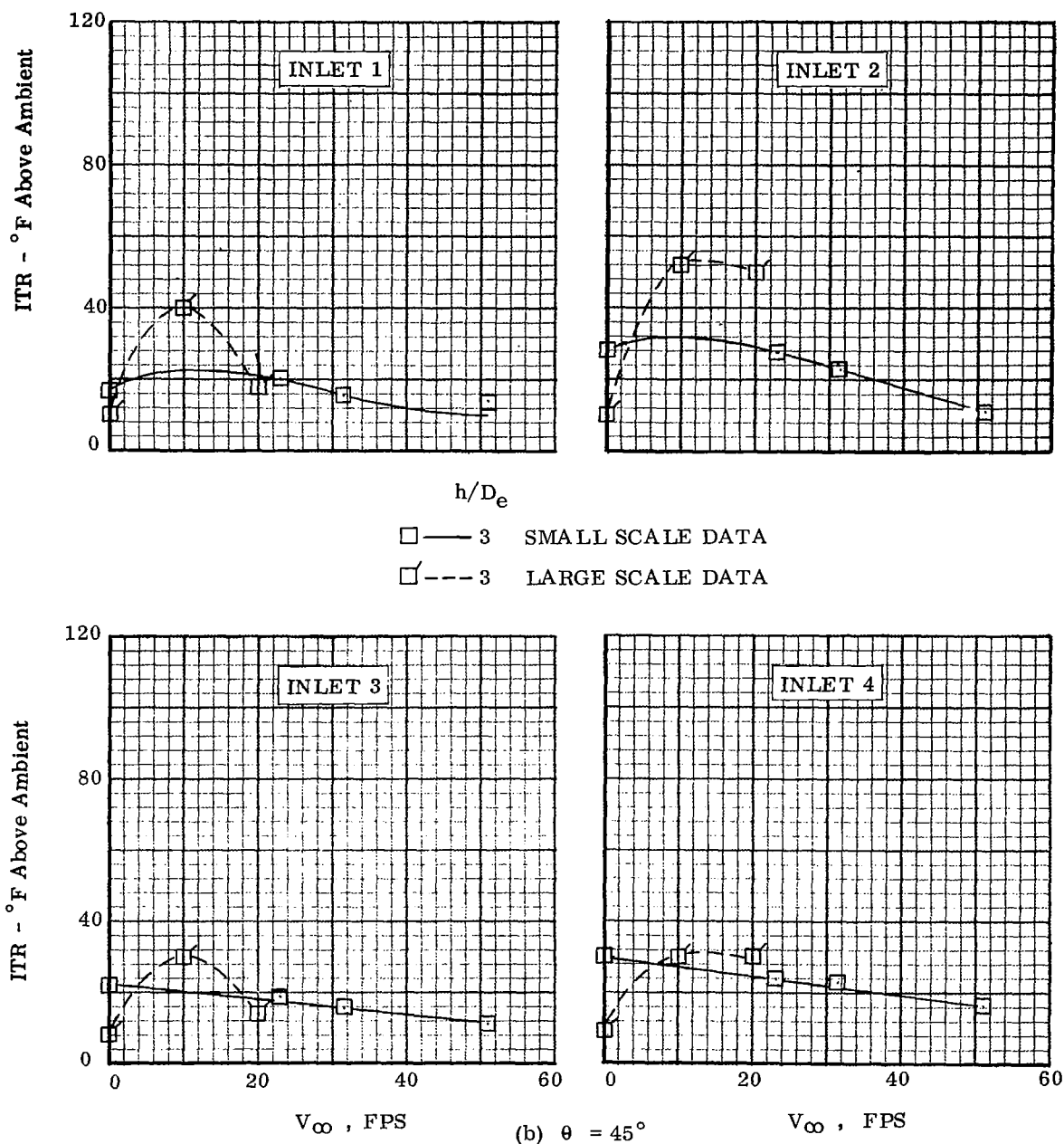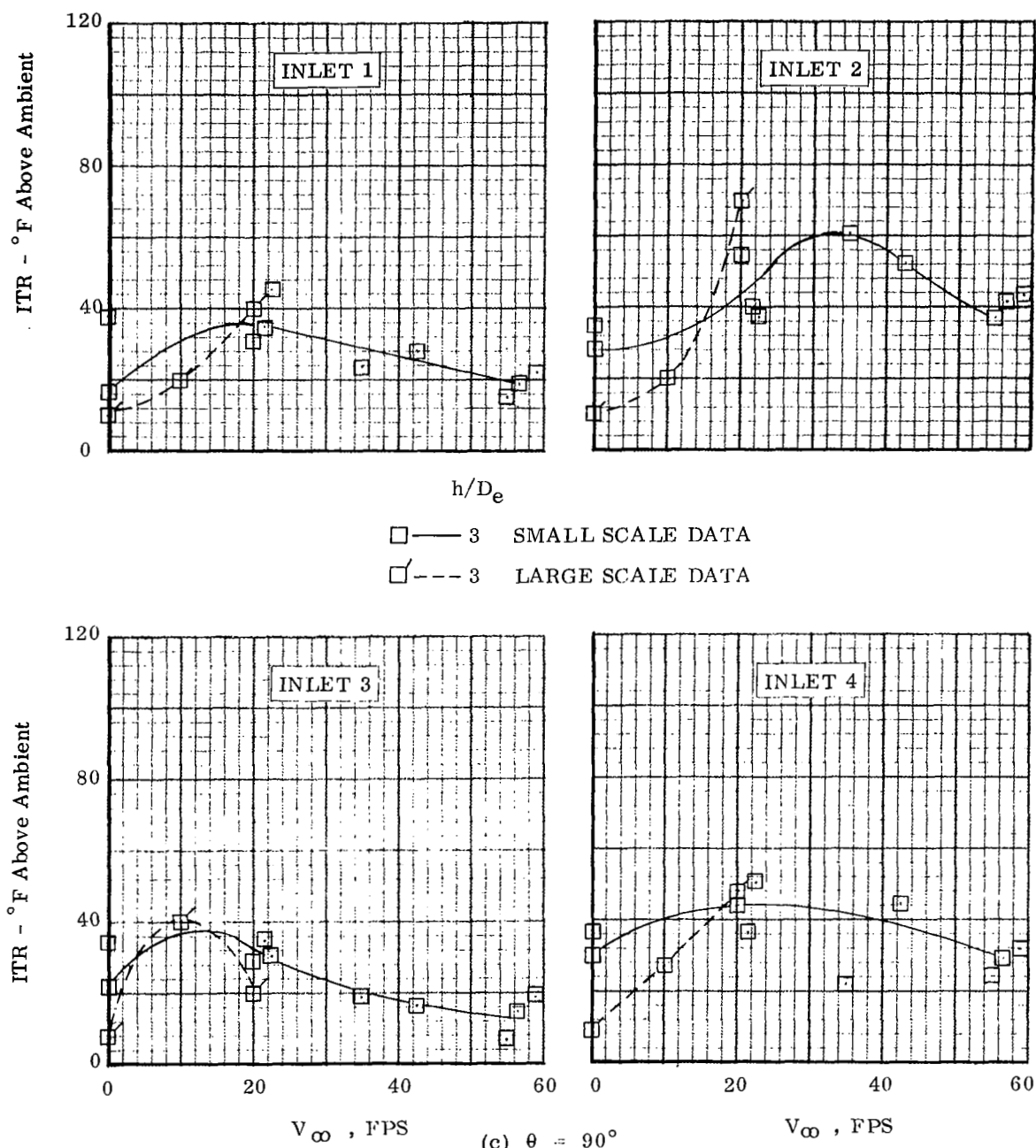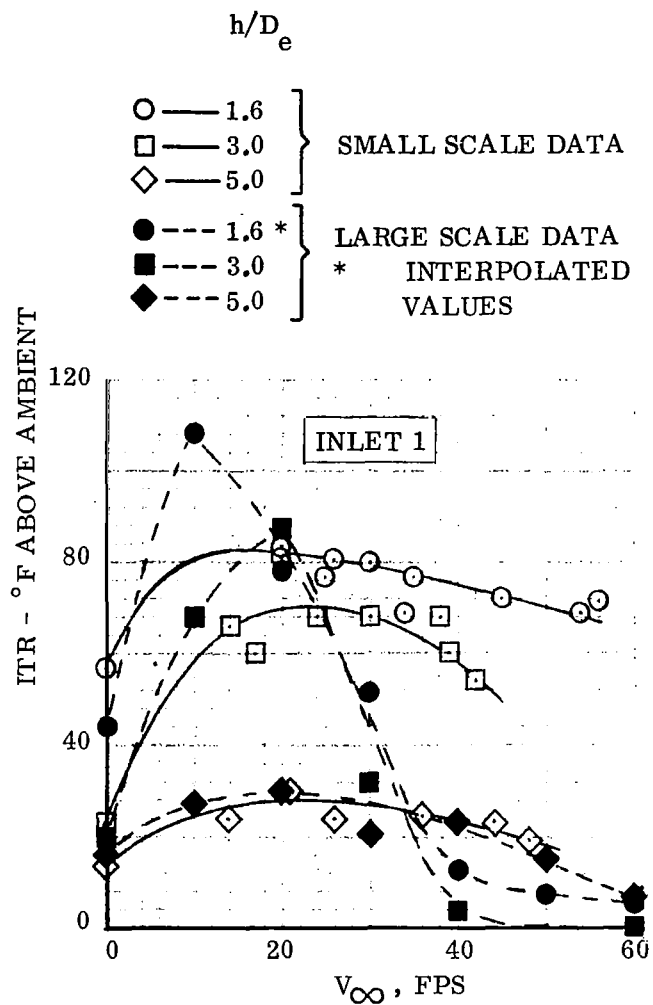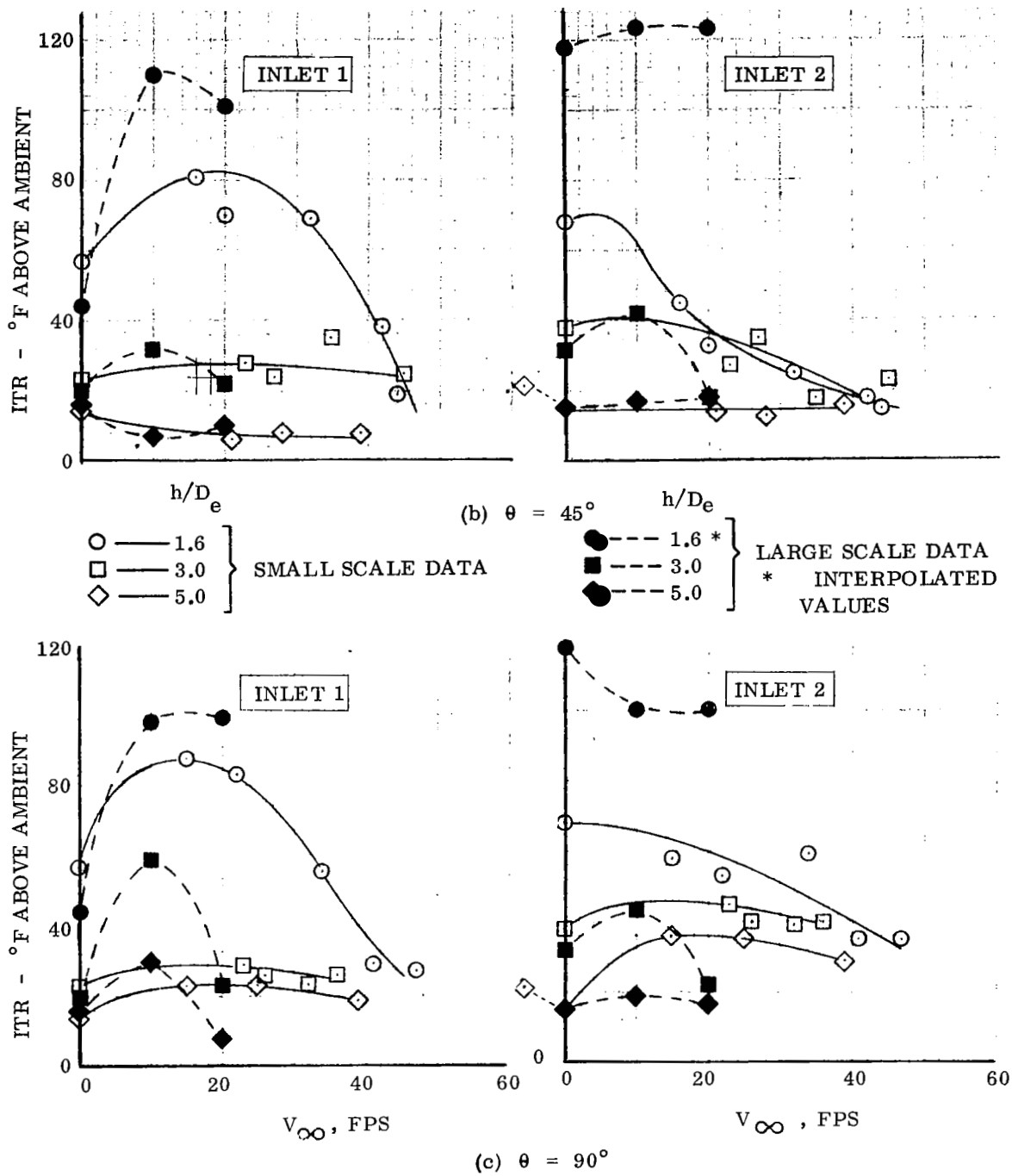
Figure 40. - Concluded.

(a) θ = 0°
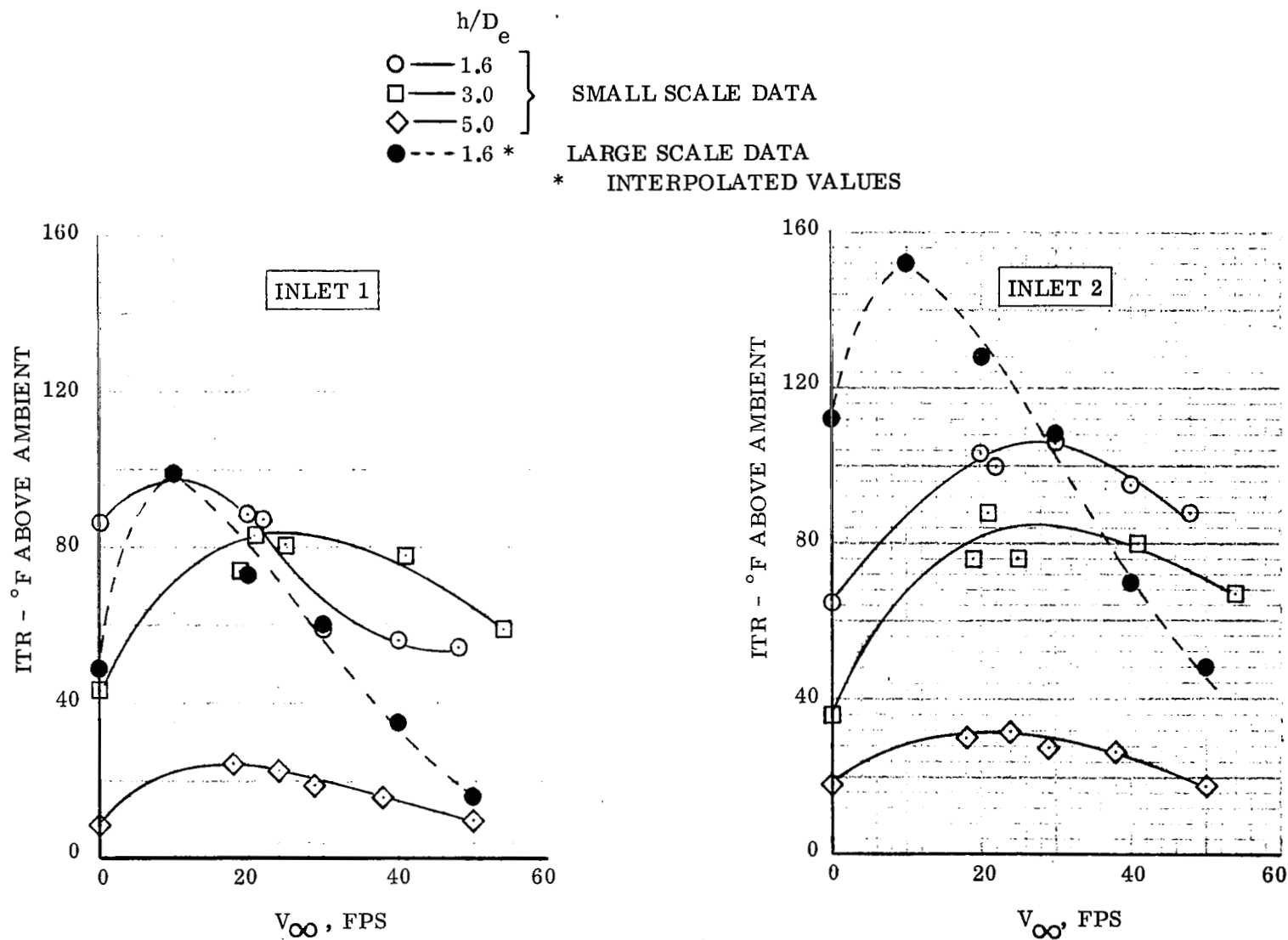
Figure 41. – Variation Of ITR With V∞ For The Side Inlet Configuration $S/S_j = 86$.

h/D_e

○ —— 1.6
□ —— 3.0      } SMALL SCALE DATA
◇ —— 5.0

● - - - 1.6 *   LARGE SCALE DATA
        *     INTERPOLATED VALUES

INLET 1

INLET 2

ITR - °F ABOVE AMBIENT

V∞ , FPS

(b)  θ = 45°

Figure 41. - Continued.

h/D$_e$

○ —— 1.6 ⎤
□ —— 3.0 ⎬ SMALL SCALE DATA
◇ —— 5.0 ⎦
● - - - 1.6 * LARGE SCALE DATA
   * INTERPOLATED VALUES



INLET 1

INLET 2

(c) θ = 90°
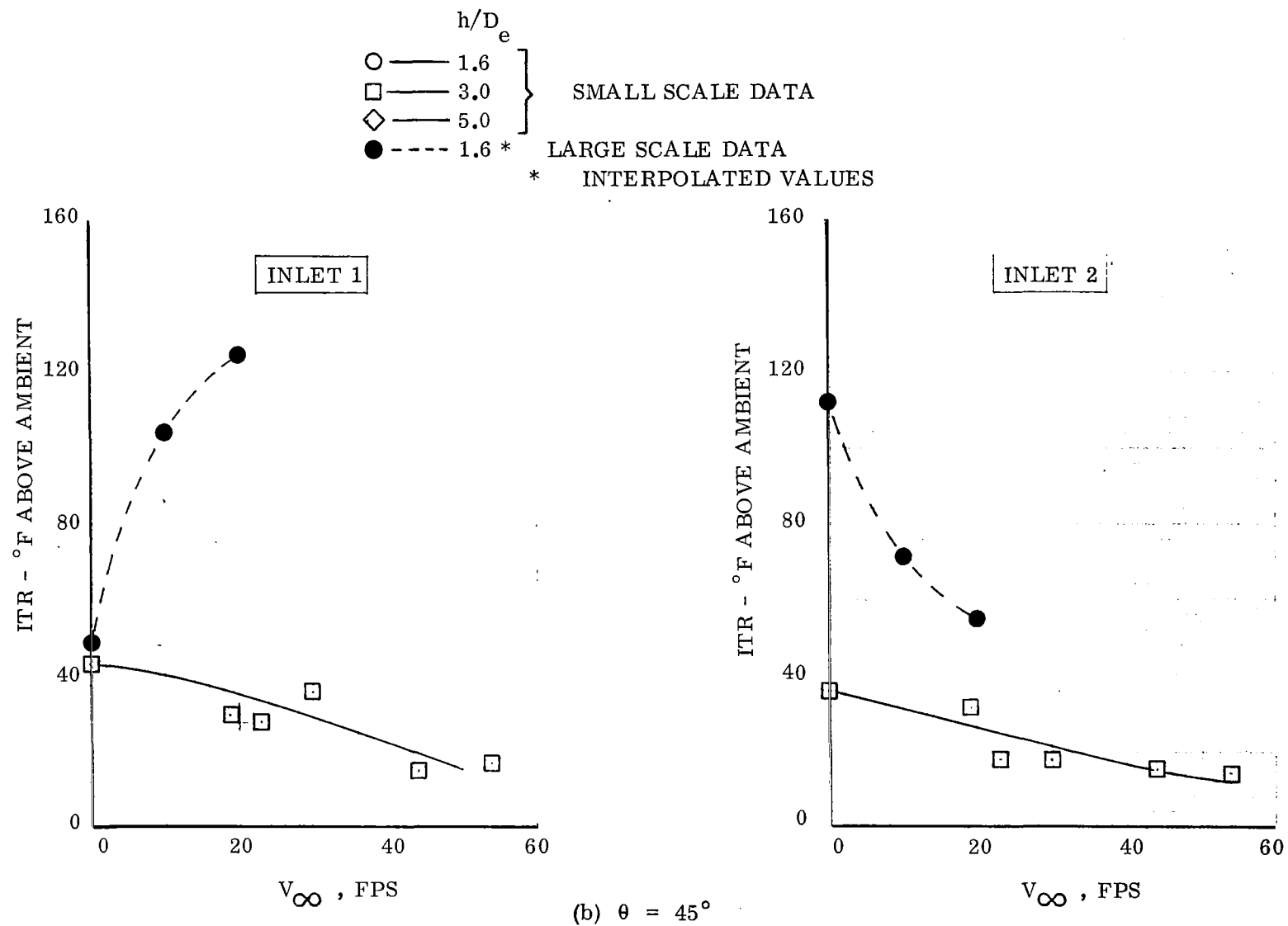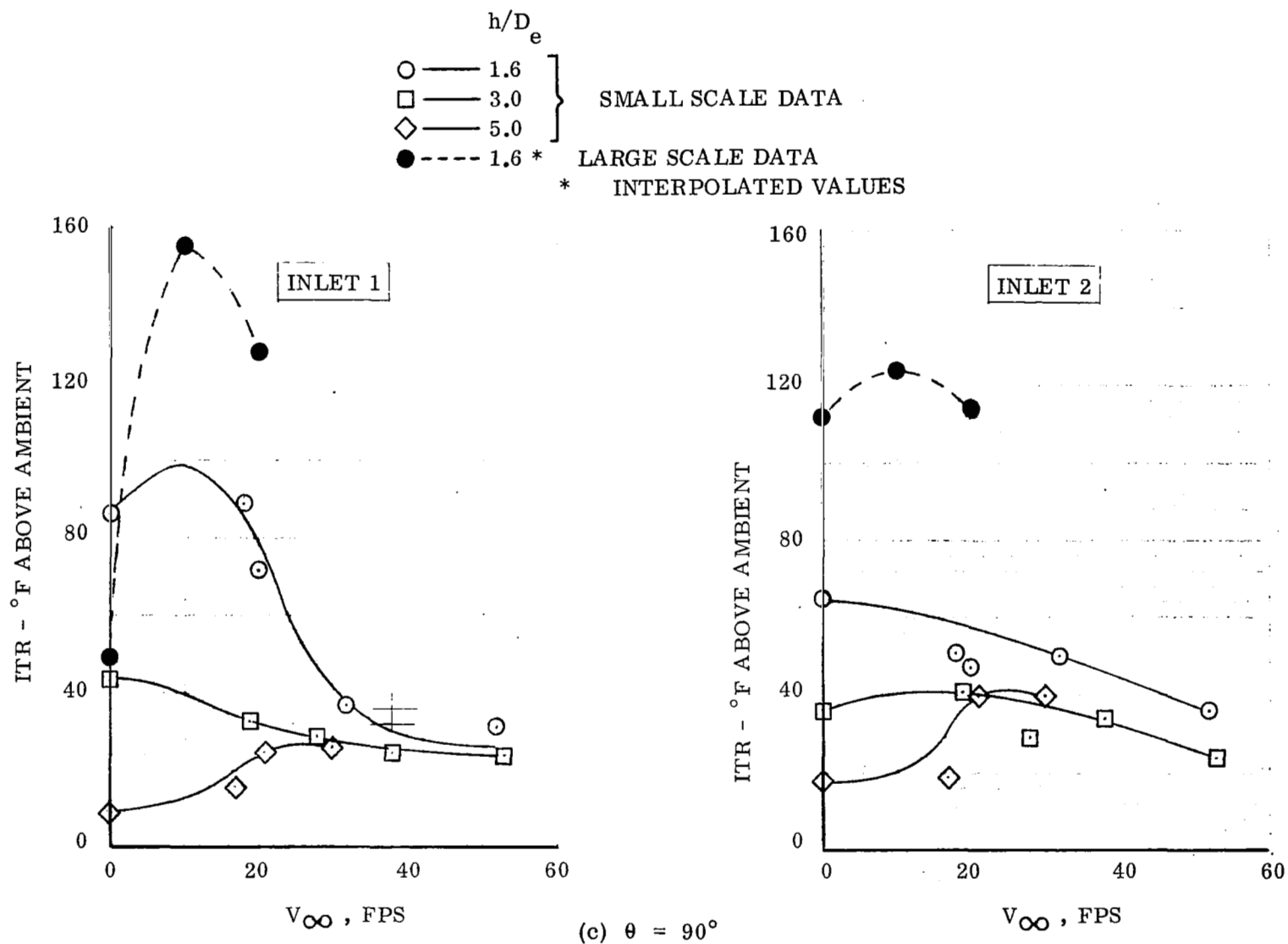
Figure 41. - Concluded.
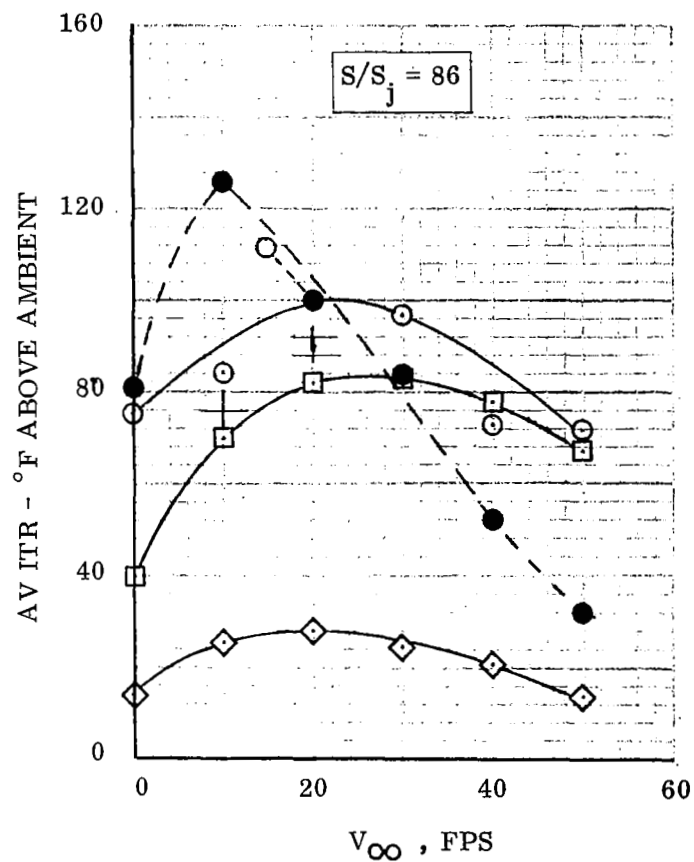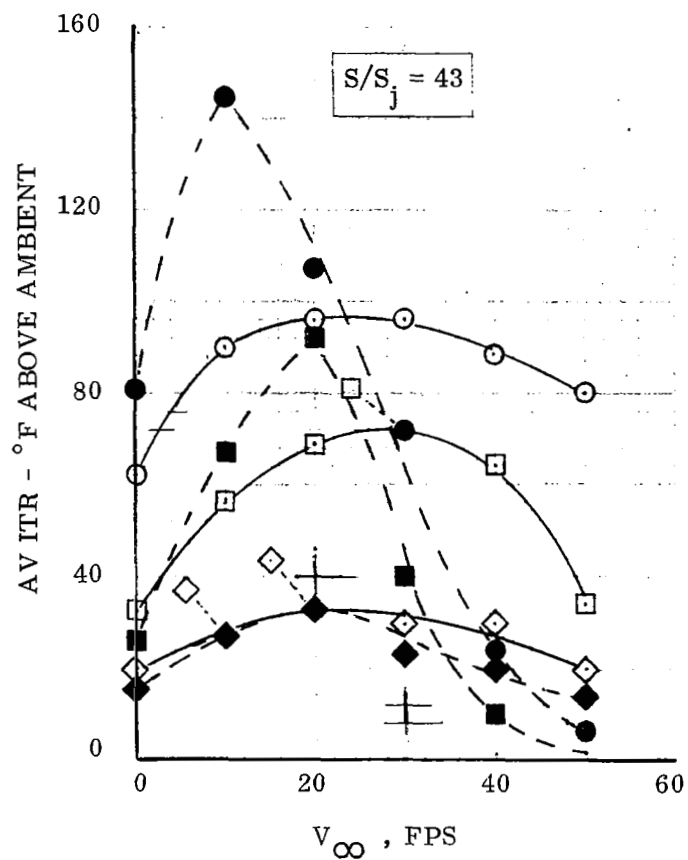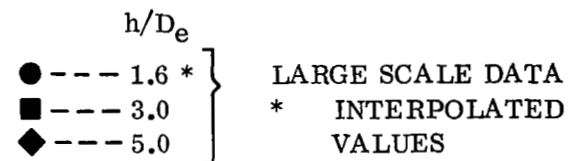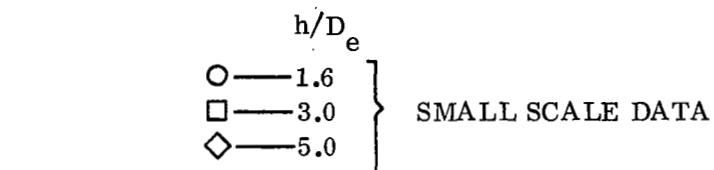
Figure 42. - Variation Of Average ITR With $V_\infty$ For The Side Inlet Configuration, $\theta = 0°$.
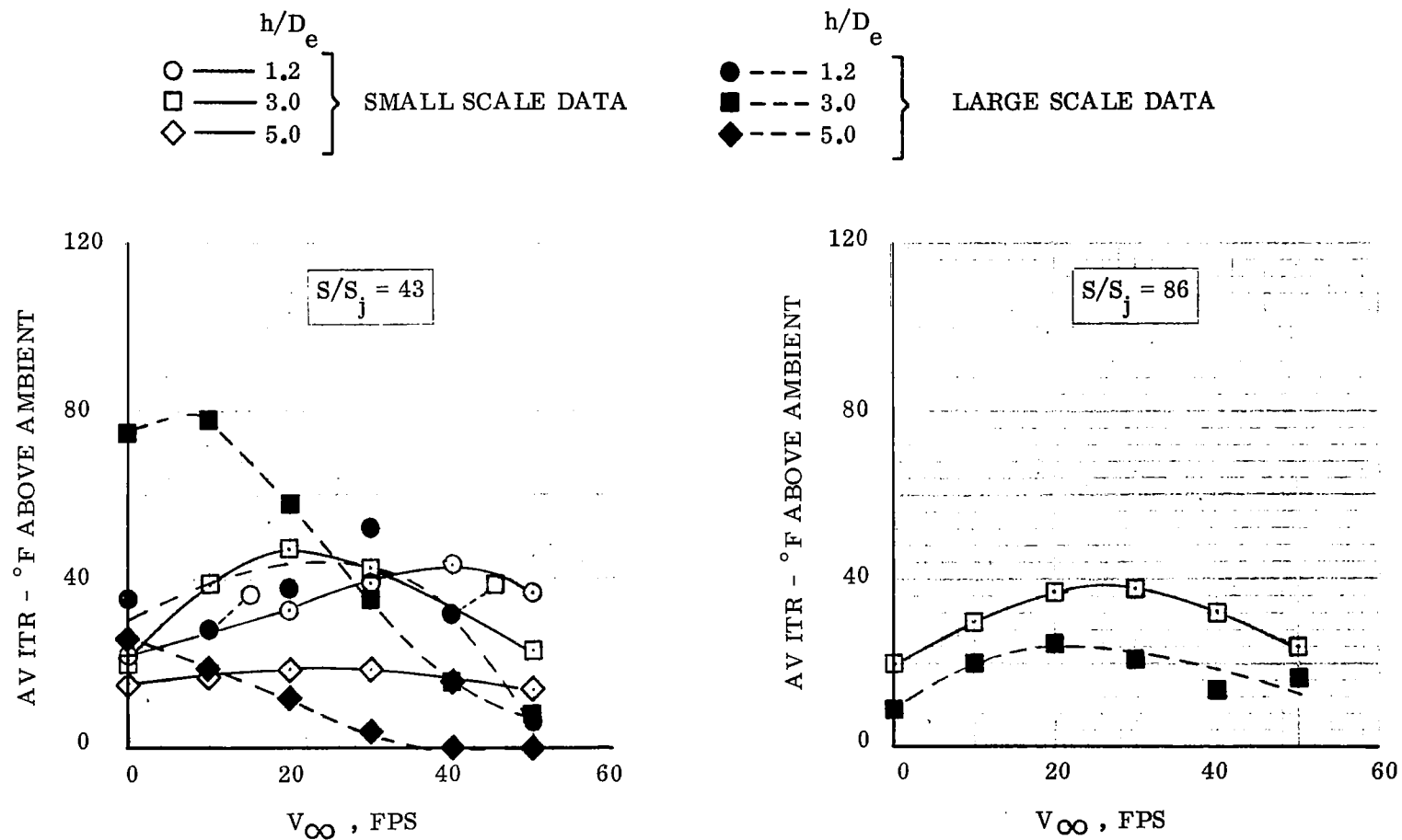
Figure 43. – Variation Of Average ITR With $V_\infty$ For The Top Inlet Configuration, $\theta = 0°$.

|  | $V_\infty$ |  | h/D |
|---|---|---|---|
| ○ | = 0 | PLAIN SYMBOL (○) | = 1.2 |
| □ | = 10 | SHADED SYMBOL (●) | = 3.0 |
| △ | = 20 | FLAGGED SYMBOL (○́) | = 5.0 |
| ◇ | = 30 | | |
| ▽ | = 40 | — - -— ONE TO ONE | |
| ◁ | = 50 | CORRELATION LINE | |
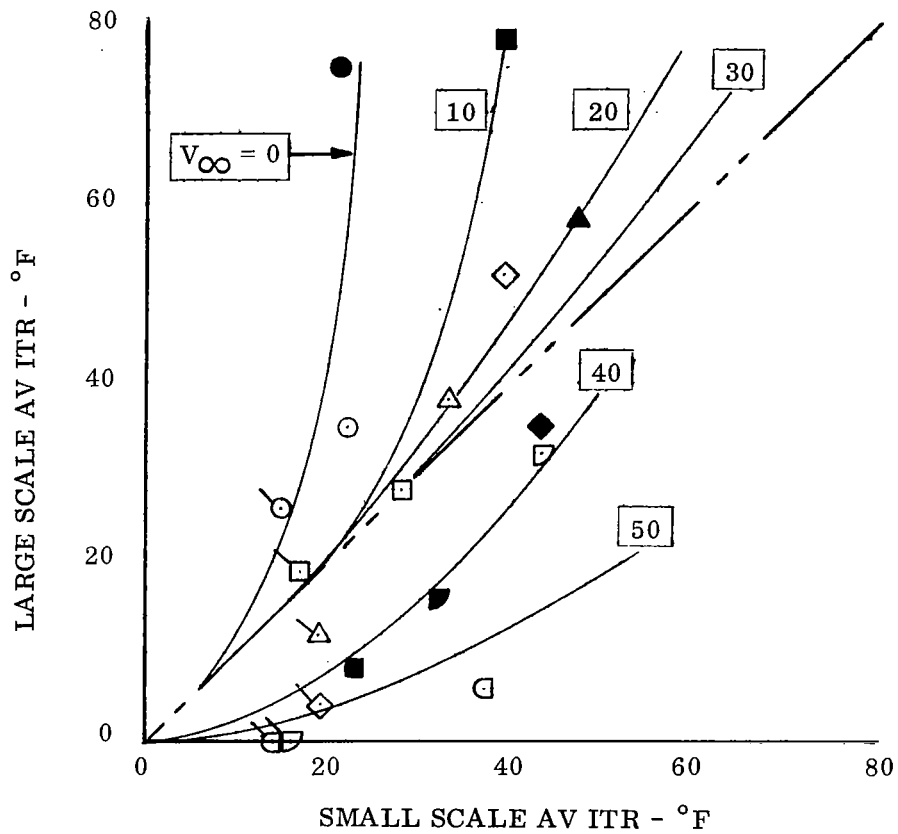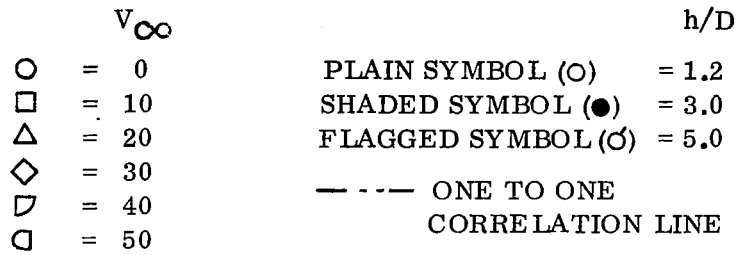
(a)  Top Inlet Configuration

Figure 44. – Comparison Of Large And Small Scale Average ITR For
Various $V_\infty$ At $S/S_j$ = 43 and $\theta$ = 0°.

90
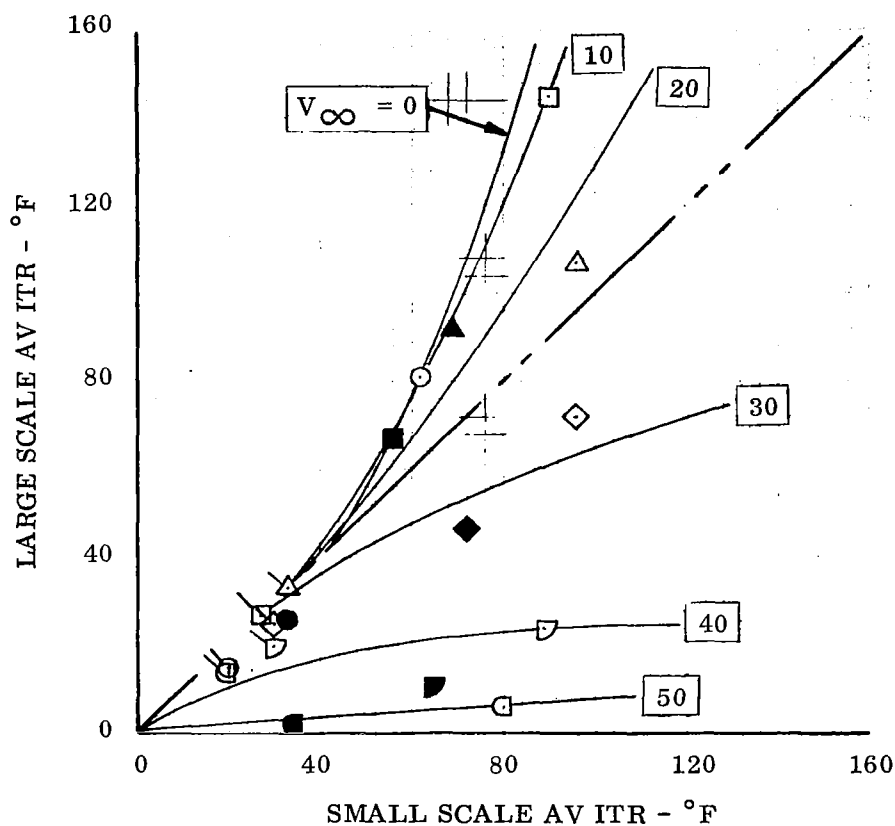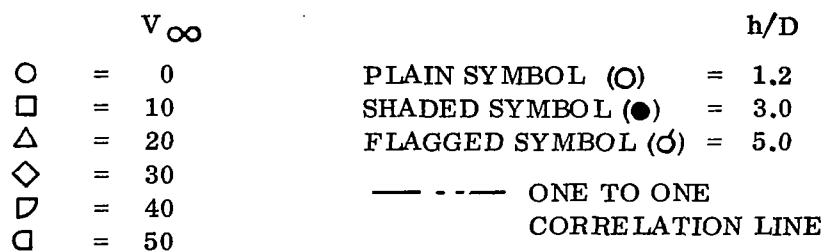
(b)  Side Inlet Configuration

Figure 44. – Concluded.

91

# APPENDIX A

## THEORETICAL ANALYSIS OF SCALE EFFECTS

### LIST OF SYMBOLS

| | |
|---|---|
| $C_F$ | Force coefficient |
| $C_p$ | Specific heat at constant pressure, $\text{BTU}/(\text{lb}_m)(^\circ F)$ |
| D | Diameter, ft |
| f | Function |
| F | Force, lb |
| g | Acceleration due to gravity, $\text{ft/sec}^2$ |
| h | Nozzle height above ground, ft |
| k | Thermal conductivity, $\text{BTU}/(\text{hr})(\text{Sq ft})(^\circ F/\text{ft})$ |
| n | Experimentally determined constant |
| $P_r$ | Prandtl Number |
| r | Radius, ft |
| $R_e$ | Reynolds Number |
| t | time, seconds |
| T | Temperature, $^\circ R$ |
| V | Velocity, ft/sec |
| y | Lateral spacing between engines, ft |

Greek :

| | |
|---|---|
| $\beta$ | Bulk coefficient of thermal expansion, $1/^\circ R$ |
| $\rho$ | Density, $\text{slugs/ft}^3$ |
| $\lambda$ | Scale factor |
| $\mu$ | Absolute viscosity, $\text{lb}_m \, (\text{hr})/(\text{ft})^2$ |

Subscripts:

| | |
|---|---|
| a | Ambient |
| b | Buoyancy |
| f | full scale |

APPENDIX A (CONT)

Subscripts:

| | |
|---|---|
| H | hot flow field gas |
| i | inlet, induced |
| j | jet exit |
| m | model |

## HOT GAS INGESTION SCALING PARAMETERS

An analysis is made to evolve the various dimensionless terms from the parameters influencing the inlet temperature rise phenomena so that these correlating parameters may be used when simulating full scale conditions by model tests. As a first step, the problem is restricted to the still air condition and the effect of surface winds on the inlet temperature rise is ignored.

Assume the inlet temperature will depend upon the following variables:

$$T_i = f \left[ V_j, \rho_j, T_j, D_j, \rho_a, T_a, (T_j - T_a), \beta, g, h, y, t, \mu_j, k_j, C_{pj}, \mu_a, k_a, c_{p_a} \right]$$

$$\text{---(1)}$$

The dependence of the temperature at any point in the flow field on jet exit velocity, density, total temperature, and diameter of the jet is evident from considerations of the jet mass flow rate and the thermal energy contained in the jet. The ambient air density and temperature values are changed due to the spreading and mixing of the heated jet with cool air. The temperature difference, the thermal volume expansion of the exhaust gases, and the acceleration due to gravity are important in assessing any buoyancy effect. The vertical distance of the jet exit from the ground, the lateral spacing between jets and the time also affect the temperature at the inlet. The effects of the coefficient of viscosity, heat conductivity and the specific heat on the inlet temperature are expected to be less significant since the momentum and heat transports are due to turbulent mixing and these far outweigh any molecular transport effects.

Using the $\pi$ theorem, Equation (1) may be rearranged as

$$\frac{T_i}{(T_j - T_a)} = f_1 \left[ R_{e_j}, \frac{T_j}{(T_j - T_a)}, \frac{\rho_j}{\rho_a}, \frac{T_j}{T_a}, \frac{V_j^2}{g\, C_{p_j}(T_j - T_a)}, \beta(T_j - T_a), \right.$$

$$\left. \frac{V_j^2}{g \beta (T_j - T_a) D_j}, \frac{h}{D_j}, \frac{y}{D_j}, \frac{t V_j}{D_j}, P_{r_j}, \frac{\mu_a}{\mu_j}, \frac{k_a}{k_j}, \frac{C_{p_a}}{C_{p_j}} \right]$$

$$\text{---(2)}$$

where $R_{e_j}$ is the Reynolds number of the jet and $P_{r_j}$ is the Prandtl number of the jet.

Assume the following parameters can be simulated between model and full-scale tests:

$$T_{j_m} = T_{j_f}, \quad \rho_{j_m} = \rho_{j_f}, \quad C_{p_{j_m}} = C_{p_{j_f}}, \quad \mu_{j_m} = \mu_{j_f}, \quad k_{j_m} = k_{j_f}, \quad \beta_m = \beta_f$$

94

Where the subscripts m and f denote model and full-scale respectively. Also assume the ambient conditions for the model and full scale are the same. Then for geometrically similar conditions, the inlet temperature will depend upon.

$$\frac{T_i}{(T_j - T_a)} = f_1 \left[ \frac{t V_j}{D_j} , \quad R_{e_j} , \quad \frac{V_j^2}{g \beta (T_j - T_a) D_j} , \quad \frac{V_j^2}{g c_{p_j} (T_j - T_a)} \right] \quad \text{---(3)}$$

The ratio, $\frac{t V_j}{D_j}$ , represents the time scaling parameter which may assume importance in transient conditions, such as the lift-off from the ground plane or the sudden opening of the hot jet and the progress of the hot gas front across the ground. In order to simulate full scale time on model tests, this ratio should be the same for model and full scale tests.

The simulation parameter, $R_{e_j}$ , represents the ratio of inertia to viscous forces of the jet. In Model tests the jet flow is usually turbulent as it would be in full scale tests, and therefore the effect of $R_{e_j}$ on the scaling of inlet temperature is expected to be small.

The relative importance of the remaining two non-dimensional terms in Equation (3) is best understood by considering the mechanism of the hot gas ingestion phenomenon of a single jet and a multi-jet configuration separately. The reason for this arises because of the fact that the two non-dimensional numbers cannot be maintained simultaneously the same for model and full scale tests.

Single Jet Case

The parameter, $\dfrac{V_j^2}{g \beta (T_j - T_a) D_j}$ , in equation (3) represents the ratio of the jet kinetic energy per unit mass to the buoyant forces in a fluid. Cox and Abbott (Reference 4) have shown that a more suitable parameter for correlating experimental data for a single jet case is

$$\frac{V_j^2}{g \beta (T_j - T_a) D_j} \qquad \left( \frac{T_a}{T_j} \right)^n$$

The reasons for the choice of exponents and proof of their use in scaling inlet temperature rise from model tests are not clear.

For a single jet, the hot exhaust gas from the nozzle impinges on the ground plane and spreads radially. The ground jet entrains air similar to a free jet, and mixes with the ambient cool air. The maximum dynamic pressure of the spreading flow is proportional to the jet dynamic pressure at the nozzle exit and varies inversely with

the square of the radious. According to Cox, at some radial distance from the jet impingement point, the flow separates from the ground when the pressure difference between ambient pressure and local surface static pressure exceeds a certain fraction of the local maximum dynamic pressure in the spreading jet. The variation of ground flow separation radius with Cox's correlating parameter is found to be linear. For geometrically similar conditions the separation radious is independent of scale effect if Cox's parameter is held the same for model and full scale tests.

When the hot gases separate and leave the ground they are influenced by two forces, buoyancy and the induced force due to the inlet and entrainment in the ground jet. If we consider an element of rising hot gas of density $\rho_H$ with dimension r, the buoyant force $F_b = (\rho_a - \rho_H) g \, r^3$.

$$\text{or} \qquad F_b \sim r^3 (T_H - T_A) \qquad\qquad \text{--- (4)}$$

The induced force, $F_i = C_F \, \frac{1}{2} \rho_a V_i^2 \, r^2$ where the induced velocity, $V_i$, is a function of the flow field and $C_F$ is a constant. If the whole flow field is represented by line sinks, the induced velocity at any point will be a function of the strengths of these sinks and the location of the point from these sinks. Neglecting the effects of ground entrainment and assuming equal inlet and exhaust mass flow through the nozzle,

$$V_i \sim \rho_j / \rho_a \quad \frac{D_j^2 \, V_j}{r_1^2}$$

where $r_1$ is the radius of the point under consideration from the nozzle inlet. Then

$$F_i \sim \rho_a \, (\rho_j / \rho_a)^2 \quad \frac{D_j^4 \, V_j^2}{r_1^4} \quad r^2 \qquad\qquad \text{---(5)}$$

Therefore,

$$\frac{F_b}{F_i} \sim \frac{r \, (T_H - T_a)}{\rho_a \, (\rho_j / \rho_a)^2 \, D_j^4 \, V_j^2} \quad r_1^4 \qquad\qquad \text{---(6)}$$

Let $D_{j_f} = \lambda \, D_{j_m}$ , $r_f = \lambda \, r_m$ , $V_{j_f} = V_{j_m}$ ,

$T_{j_f} = T_{j_m}$ , $\rho_{j_f} = \rho_{j_m}$ , and $\rho_{a_f} = \rho_{a_m}$ , Here $\lambda$ is

a scale factor. For equally scaled points away from the inlet of full scale and model,

$$\left(\frac{F_b}{F_i}\right)_f \bigg/ (F_b/F_i)_m = \left(\frac{r_f}{r_m}\right) \frac{(T_H-T_a)_f}{(T_H-T_a)_m} \qquad ---(7)$$

From the foregoing approximate analysis, it appears that the ingestion of the hot gas into the inlet depends on the scale of the eddies separating from the ground and the temperature differences of the hot elemental gas with the ambient air. Further experiments are needed to understand the energy transport and mixing phenomenon of the hot gases with the ambient air. The size and shape of the eddies breaking from the ground, the velocity of rising hot gas element, the height above ground and the path traced by the hot gases before arriving at the inlet are to be measured in the tests.

Two Jet Configuration

The flow field of a two jet configuration differs from the single jet case in some respects; the normal impinging jets spread radially and form a 'fountain' of hot gas in between the jets. There is very little experimental data regarding the flow character-istics of the 'fountain'. The far fields of the two ground jets are similar to that of a single jet case. Tests show that the inlet temperature rise for the two jet case is higher and more severe than the single jet. In the two jet case the total ingestion of hot gases at each inlet should comprise of the 'fountain effect' and of the natural free convection of the far field gases of each jet. No tests have been done so far to separate the inlet temperature rise contribution due to these two effects.

The question arises whether the 'fountain effect' is a free or forced convection of rising hot gases. If it is the latter, the non-dimensional number $V_j^2/g\beta (T_j-T_a)D_j$ in Equation (3) need not be the same for the model and full scale tests. On the other hand the parameter $\dfrac{V_j^2}{g \, C_{p_j} (T_j-T_a)}$ in Equation (3) may have greater influence on the ingestion phenomenon. This parameter represents the ratio of the kinetic energy of the jet to the heat lost by the exhaust gases.

97

In order to understand the process of hot gas ingestion in the two jet case, more should be known of the fountain. The fountain height above the ground, the maximum vertical velocity at fountain axis, the velocity decay along the axis of the fountain, and the corresponding temperature distributions are expected to influence the ingestion process. Even though the jet dynamic pressure in the near field of the jets is high in the formation of the fountain the horizontal velocity components of the two ground jet are redirected and form the reinforced ground jets as well as vertical velocity in the fountain. The magnitude of this vertical velocity may give an indication whether the 'fountain effect' is a free or forced convection of rising hot gases.

## Conclusions

It can be concluded that for the single jet case, the Cox criterion must be satisfied. This implies that scale tests should not be conducted at $V_{j_m} = V_{j_f}$ and $T_{j_m} = T_{j_f}$, but rather

$$\left[ V_j^2/T_j^{1/2}(T_j - T_a)\beta \right]_m = \frac{1}{\lambda} \left[ V_j^2/T_j^{1/2}(T_j - T_a)\beta \right]_f.$$

It is not known whether this criterion is valid for multiple jet configurations primarily because of the presence of the fountain.

Experimental data are needed to:

1.   Isolate the effects on ITR due to the fountain, and the far field.

2.   Determine the effect of exhaust mass flow and momentum on ITR scale effect.

3.   Determine model to full scale correlation of ITR when the Cox criterion is satisfied, and again when the forced convection criterion is satisfied.

4.   Provide additional information pertaining to the characteristics of the fountain.

# APPENDIX B

## Data Analysis

General. -- During the course of this test program, all inlet temperature rise data were permanently recorded as time histories on oscillographs. Temperature time histories typical of the results obtained for the four models tested are shown in Figures B-1 through B-4 in which, for the sake of clarity, selected channels of the maximum, minimum and electrical average temperatures for the test have been shown. It may be seen that actuation of the trap door provided a satisfactory definition of test start and test end and that approximately 2 seconds was required to reach steady state.

The ITR quoted in this report are steady state values which were obtained from a section of the oscillograph record where the thermocouple traces exhibited steady state temperatures and where satisfactory values of test conditions (model pressures and wind velocity) were indicated.

Accuracy of electrical average technique. -- The special electrical averaging circuits accurately represented the arithmetic average of the temperatures sensed by all the thermocouples at each inlet as can be seen in Figure B-5. The seven sets of data used in the figure were randomly selected from actual test runs and show an average 5.2% deviation of the electrical average value from the arithmetic average. It was concluded that the electrical average trace was indeed a good representation of the average ITR at each inlet.

Pod (circ) model inlet tube temperatures. -- The temperatures measured inside the inlet tubes of the Pod (circ) model represent ITR at each inlet, as shown in Figure B-6. This correlation negates the necessity for locating thermocouples in every inlet and permits inlet tube temperatures to be used whenever ITR comparisons between engine 1 and 2 or inlets A, B, and C are needed.

Repeatability. -- During the course of this program, several tests were repeated. The temperature data from these runs are shown in Table B-1. Here, it may be seen that repeatability is good except when fountain instability was encountered for the dual (circ) model. The high degree of repeatability is graphically presented in Figure B-7. The accuracy of temperature measurements is seen to be approximately $\pm 5^{\circ}$ F.

## TABLE B-I

### REPEATABILITY

| | | $\alpha$ | $V_\infty$ | $\theta$ | POD (CIRC) MODEL | | | | | | | |
|---|---|---|---|---|---|---|---|---|---|---|---|---|
| | | | | | TEMPERATURE - $^\circ$F ABOVE AMBIENT | | | | | | | |
| $h/D_e$ | $S/S_j$ | | | | ELECTRICAL AV. | | INLET TUBES - ENG. NO. 1 | | | INLET TUBES - ENG. NO. 2 | | |
| | | (DEG) | (FPS) | (DEG) | INLET A | INLET B | A | B | C | A | B | C |
| 3 | 100 | 0 | 40 | 0 | 60/57 | 40/42 | 66/59 | 52/39 | 40/26 | 34/33 | 65/71 | 51/51 |
| 3 | 100 | 0 | 45 | -30 | 16/13 | 3/6 | 16/11 | 0/3 | 0/0 | 23/20 | 48/48 | 33/34 |
| 3 | 100 | 10 | 40 | 0 | | - | 43/50 | - | 31/27 | - | - | 43/53 |

NOTES:

(1) Tabulated data shows temperatures from the first/repeat test

(2) ( - ) indicates thermocouple inoperative

| | | EDA | $V_\infty$ | $\theta$ | DUAL (CIRC) MODEL | | | | | | |
|---|---|---|---|---|---|---|---|---|---|---|---|
| | | | | | TEMPERATURE - $^\circ$F ABOVE AMBIENT | | | | | | |
| $h/D_e$ | $S/S_j$ | | | | ELECTRICAL AV. | | FIELD THERMOCOUPLES | | | | |
| | | (DEG) | (FPS) | (DEG) | ENG.NO.1 | ENG.NO.2 | 23 | 24 | 25 | 26 | 27 |
| 2 | 0 | 0 | 53 | 0 | 16/24 | 12/23 | 14/22 | 14/20 | 69/73 | 16/20 | 14/24 |
| 2 | 100 | 20 | 32 | 0 | 15/15 | 11/10 | 18/14 | 13/15 | 25/17 | 9/14 | 20/13 |
| 2 | 100 | 20 | 20 | -30 | 4/5 | 2/3 | 6/6 | 4/4 | 2/1 | 0/0 | 0/1 |
| 2 | 100 | 20 | 15 | -60 | 0/3 | 1/7 | 0/5 | 0/3 | 0/5 | 1/5 | 1/4 |
| 2 | 0 | 20 | 22 | -30 | 10/9 | 25/24 | 8/9 | 7/6 | 26/22 | 8/12 | 5/4 |
| 2 | 0 | 20 | 27 | -60 | 7/11 | 8/15 | 10/10 | 6/10 | 4/9 | 2/0 | 1/6 |
| 2 | 0 | 20 | 20 | 0 | 36/32 | 41/19 | 21/11 | 29/20 | 87/65 | 33/16 | 13/7 |

REPEATABILITY

| | | | | SCALED NASA MODEL  –  TOP  INLET CONFIGURATION | | | | | | | | | |
|---|---|---|---|---|---|---|---|---|---|---|---|---|---|
| | | | | TEMPERATURE – °F ABOVE AMBIENT | | | | | | | | | |
| $h/D_e$ | $S/S_j$ | $V_\infty$ (FPS) | $\theta$ (DEG) | INLET NO. 1 | | | INLET NO. 2 | | INLET NO. 3 | | INLET NO. 4 | | |
| | | | | MIN | MAX | ELEC. AV. | MIN | MAX | MIN | MAX | MIN | MAX | ELEC. AV. |
| 3 | 86 | 36 | 0 | 37/40 | 53/53 | 46/39 | 32/23 | 43/47 | 32/31 | 44/35 | 34/33 | 40/30 | 33/34 |
| 3 | 86 | 53 | 0 | 24/25 | 33/32 | 26/23 | 25/22 | 28/27 | 22/21 | 26/25 | 18/16 | 23/22 | 22/18 |
| 5 | 43 | 26 | 90 | 22/29 | 25/32 | 22/28 | 32/37 | 31/33 | 25/28 | 26/34 | 26/32 | 25/29 | 26/27 |
| 3 | 43 | 21 | 0 | 40/46 | 86/82 | 43/42 | 45/44 | 102/93 | 34/35 | 48/50 | 32/27 | 47/43 | 36/32 |

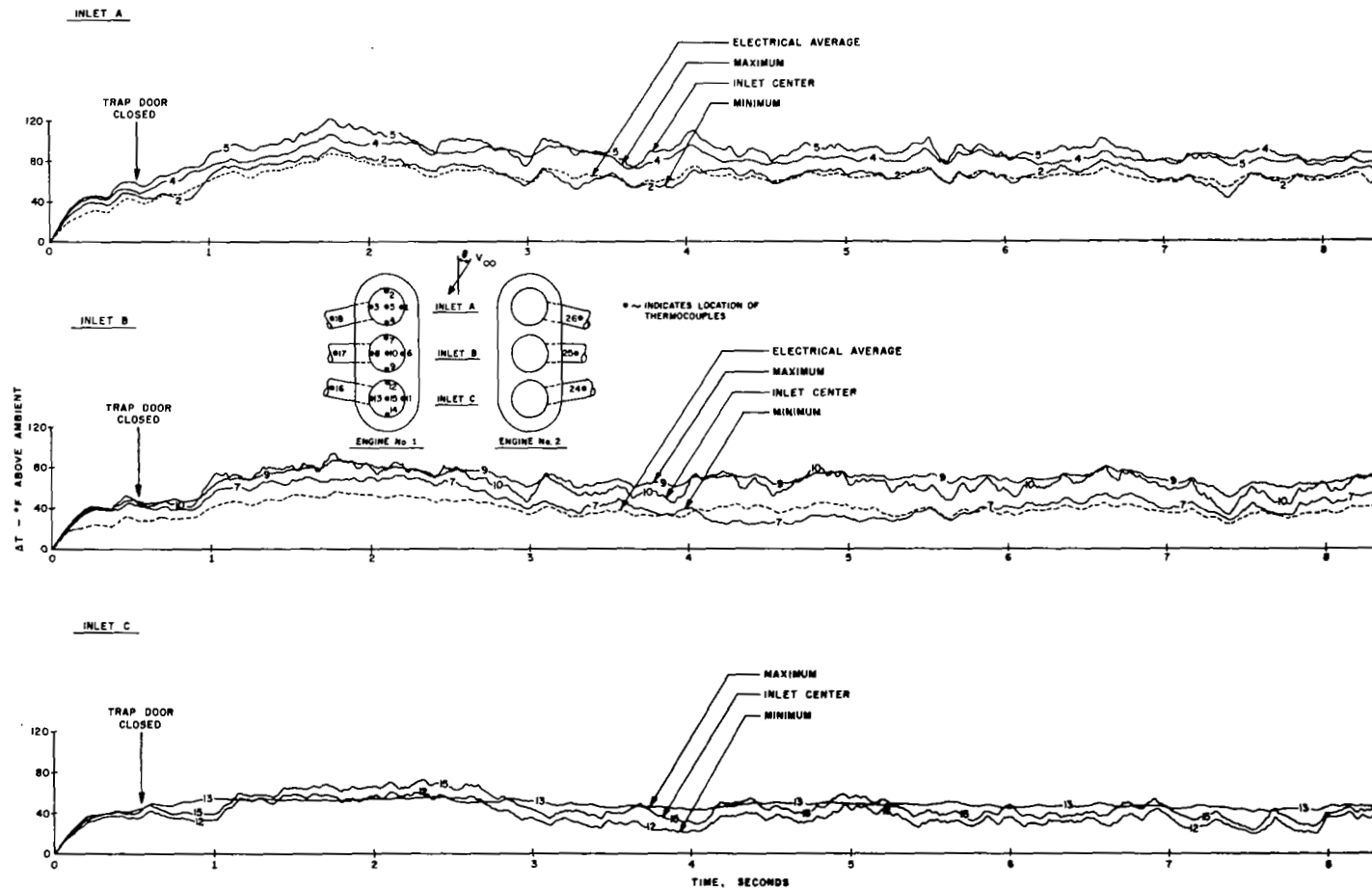| | | | | SCALED NASA MODEL – SIDE  INLET  CONFIGURATION | | | | | |
|---|---|---|---|---|---|---|---|---|---|
| | | | | TEMPERATURE – °F ABOVE AMBIENT | | | | | |
| $h/D_e$ | $S/S_j$ | $V_\infty$ (FPS) | $\theta$ (DEG) | INLET NO. 1 | | | INLET  NO. 2 | | |
| | | | | MIN | MAX | ELEC. AV. | MIN | MAX | ELEC. AV. |
| 1.6 | 43 | 20 | 0 | 48/43 | 242/241 | 83/81 | 42/39 | 177/190 | 106/117 |

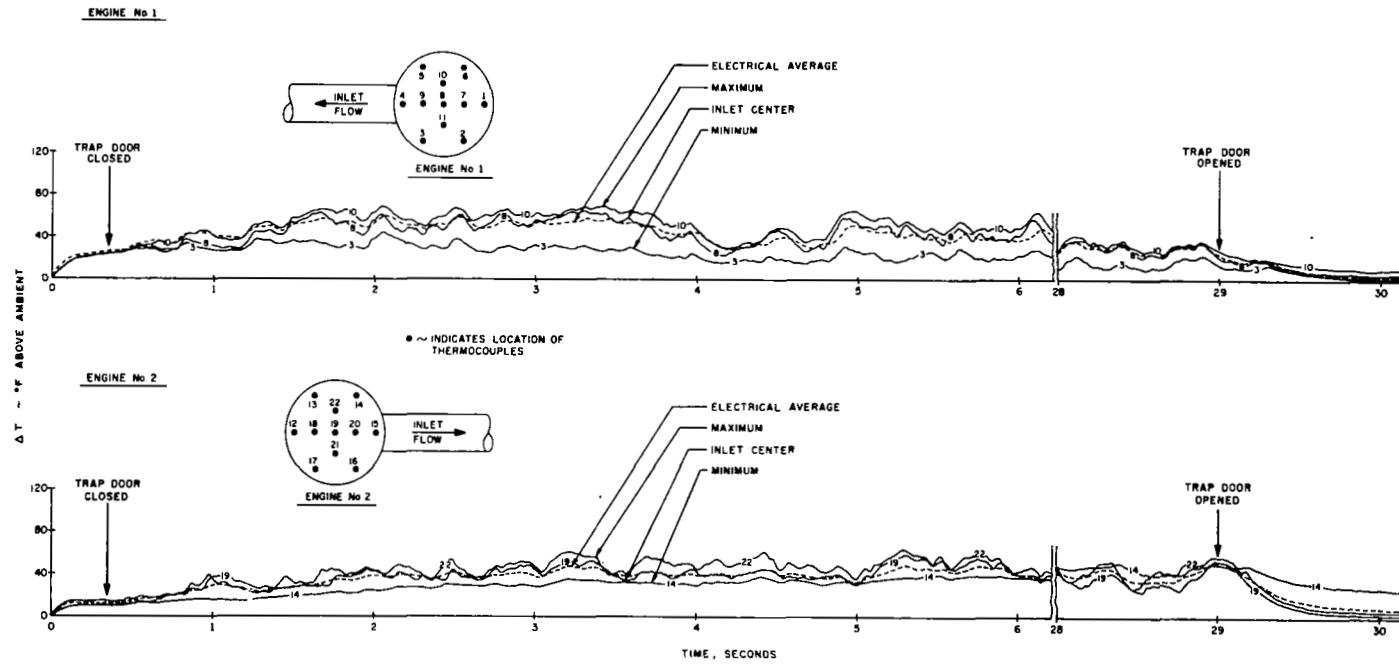Figure B-1. - Typical Inlet Temperature Time History.  Pod (circ) Model, Engine No. 1

Figure B-2. – Typical Inlet Temperature Time History, Dual (circ) Model.
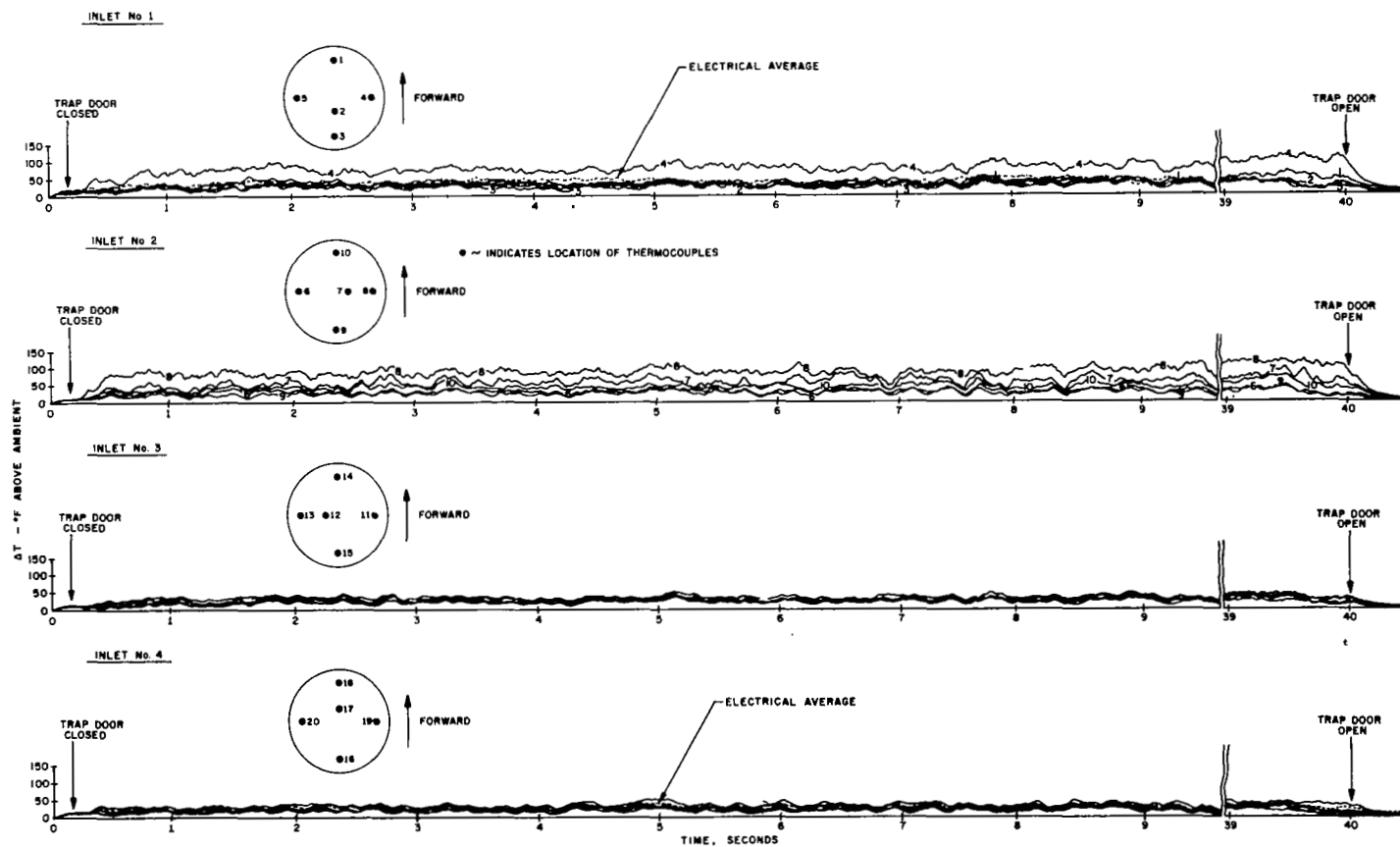
Figure B-3. – Typical Inlet Temperature Time History, NASA Model, Top Inlet Configuration.
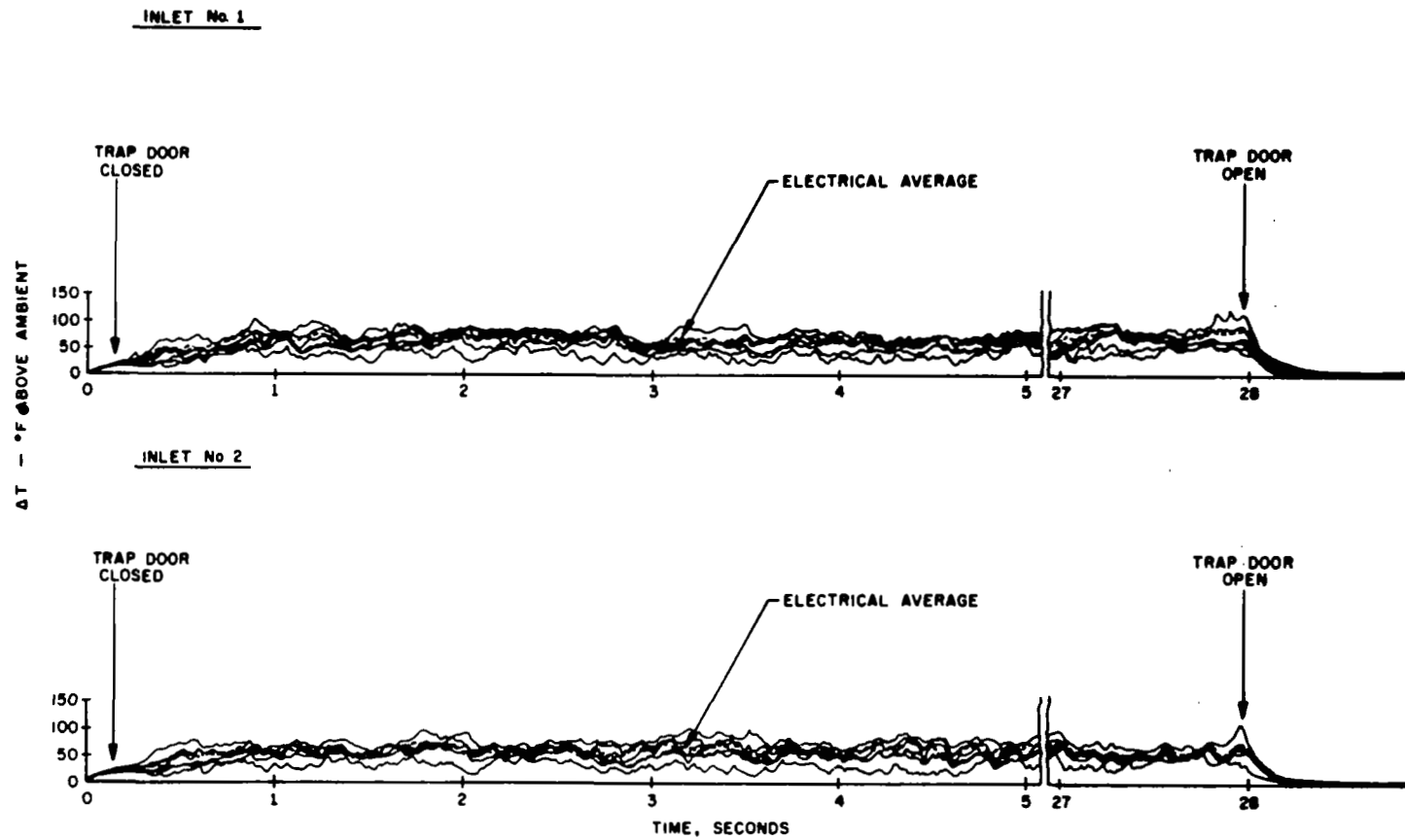
INLET No. 1



INLET No 2



TIME, SECONDS

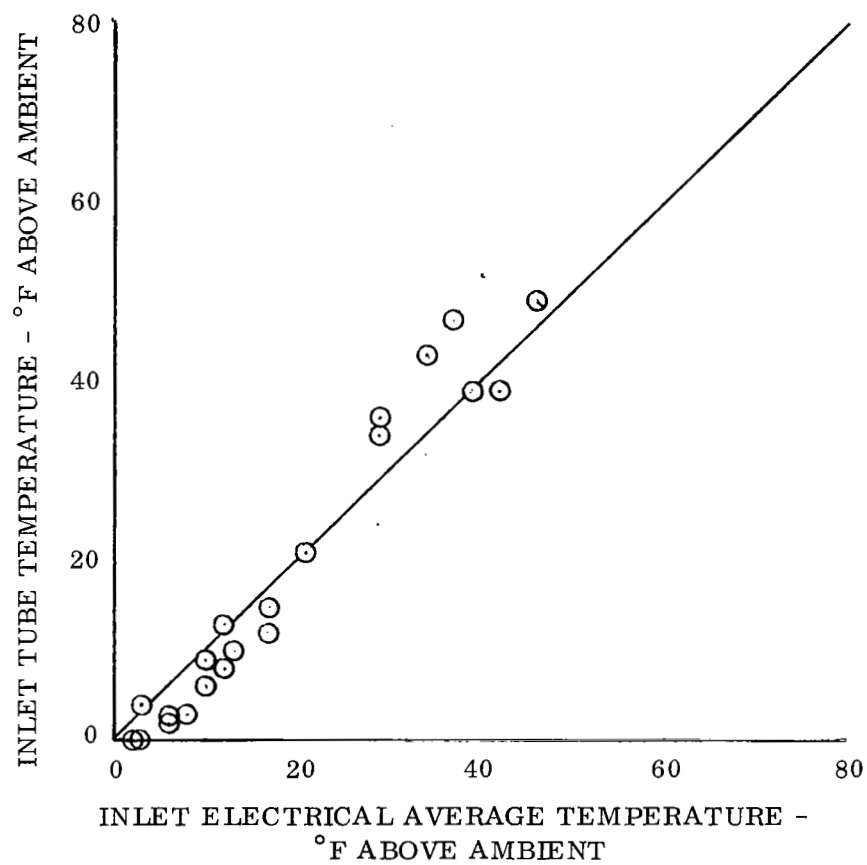Figure B-4. - Typical Inlet Temperature Time History, NASA Model, Side Inlet Configuration.
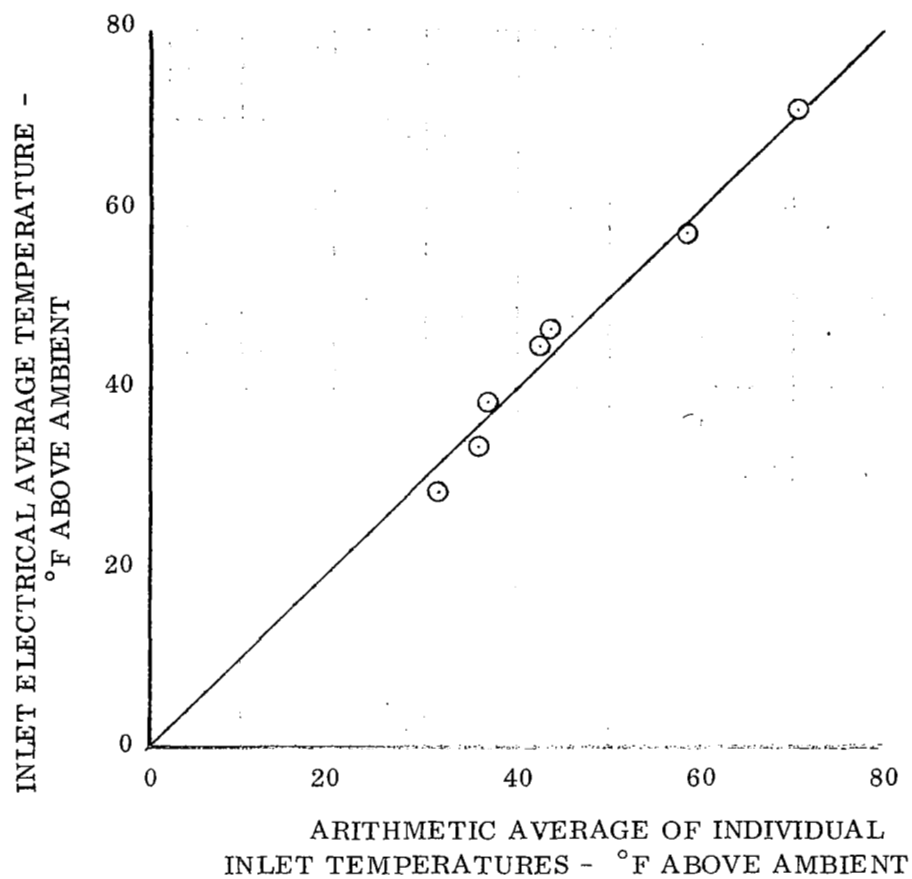
Figure B-5. – Accuracy of Electrically Averaged Temperatures.
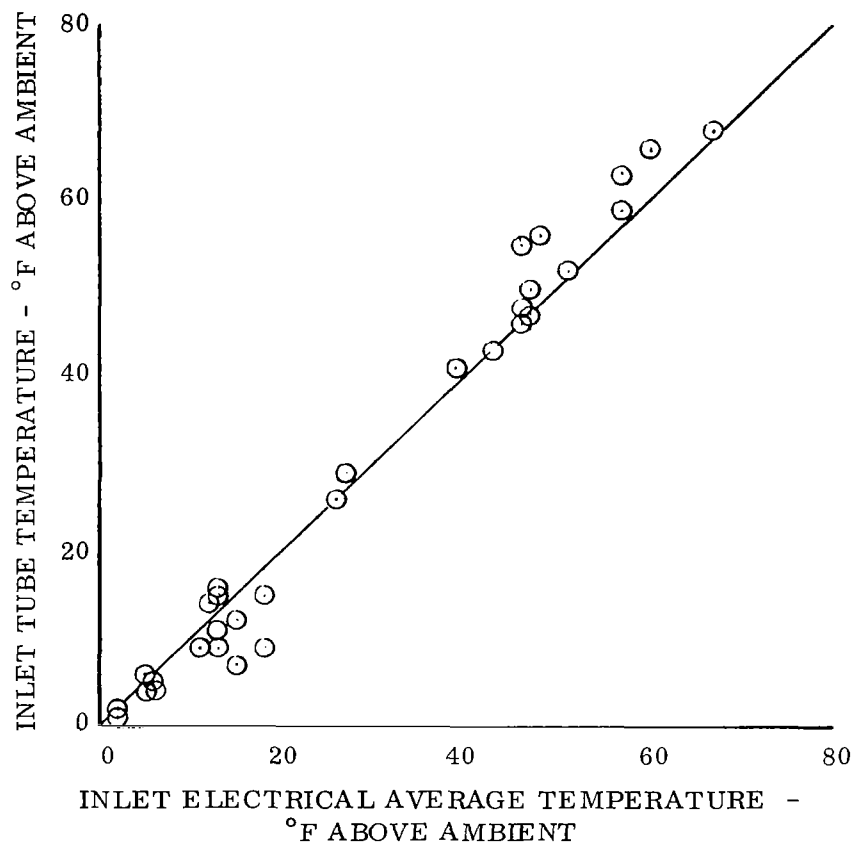
(a) Inlet A

Figure B-6. - Comparison Of Inlet Tube And Electrically Averaged Temperatures For The Pod (circ) Model.

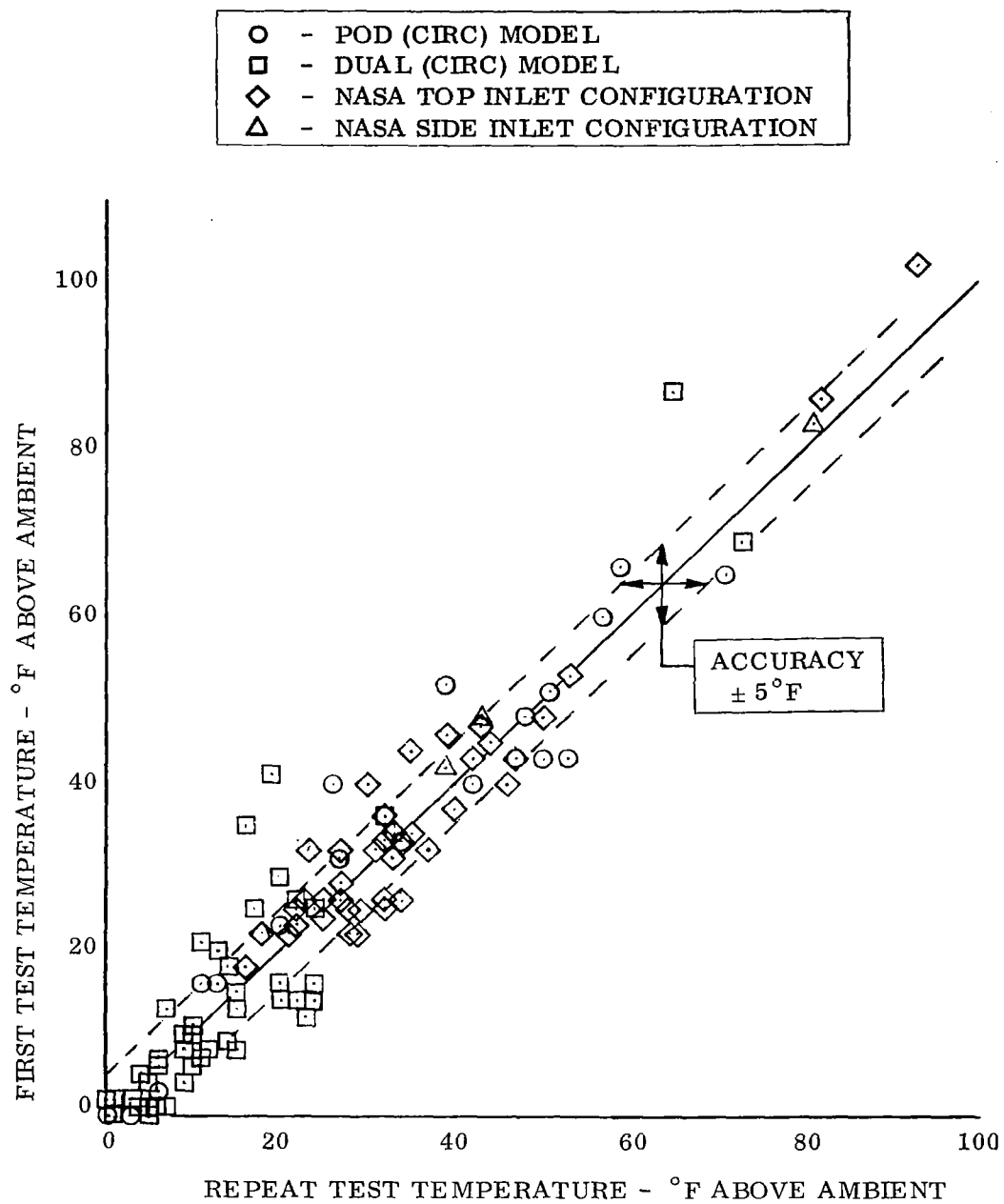(b) Inlet B

Figure B-6. - Concluded.

ACCURACY
± 5°F

Figure B-7. – Repeatability.

109

# APPENDIX C

## Wind Effects

Ground plane boundary layer thickness. - The boundary layer on the auxiliary ground plane was approximately 0.9 inches thick 3 feet from the ground plane leading edge for a free stream velocity of 46 fps. The thickness was determined from velocity measurements made with the hot wire anemometer located near the ground plane surface. The thickness of the boundary during large scale tests in the NASA Langley 30 x 60 foot wind tunnel was calculated to be 3.6 inches 12.5 feet from the ground board leading edge for a free stream velocity of 50 fps. For a model linear scale factor of 0.24 calculation shows that the small scale boundary layer thickness very closely represents (0.87 inches actual, 0.9 inches required) the large scale conditions.

Effect of random wind on ITR transients. - When hot gas ingestion tests are conducted out of doors the effects of random winds on ITR measurements must be considered. Reference 2 has shown that winds less than 2 fps do not significantly effect ITR. During this present program, hot wire anemometry was used to assess in more detail the effects of random winds on temperature measurements.

Temperature time histories of 3 field thermocouples located above the Dual (circ) model and the simultaneous time history of random wind speed and direction are shown in Figures C-1 and C-2. These plots are typical of those encountered in tests conducted during high random wind situations and show that the field temperatures are directly influenced by random wind.

Median curves were faired through the rapidly fluctuating random wind traces to permit a gross analysis of results. It is noted that variations in random wind speed directly influence the temperature measured in the field above the model. The indicated time phase lag between wind speed and temperature agrees with computed values based on a mean wind speed over the distance between the hot wire anemometer and the field thermocouples (approximately 6 feet).

It is noted that the data in Figures C-1 and C-2 were measured during high and gusty wind conditions. These conditions were chosen so that the resulting high temperatures would provide a measure of temperature effects which would not be masked by the noise level of the experiment. An analysis of the data shows (Figure C-3) that ITR will increase approximately $2°F$ for every 1 fps increase of random wind speed. This agrees with the Reference 2 conclusion alluded to above.

Since ITR data will generally not be more accurate than $\pm 5°F$, it can be concluded that outdoor tests may be conducted when random winds do not exceed 2 to 3 fps.
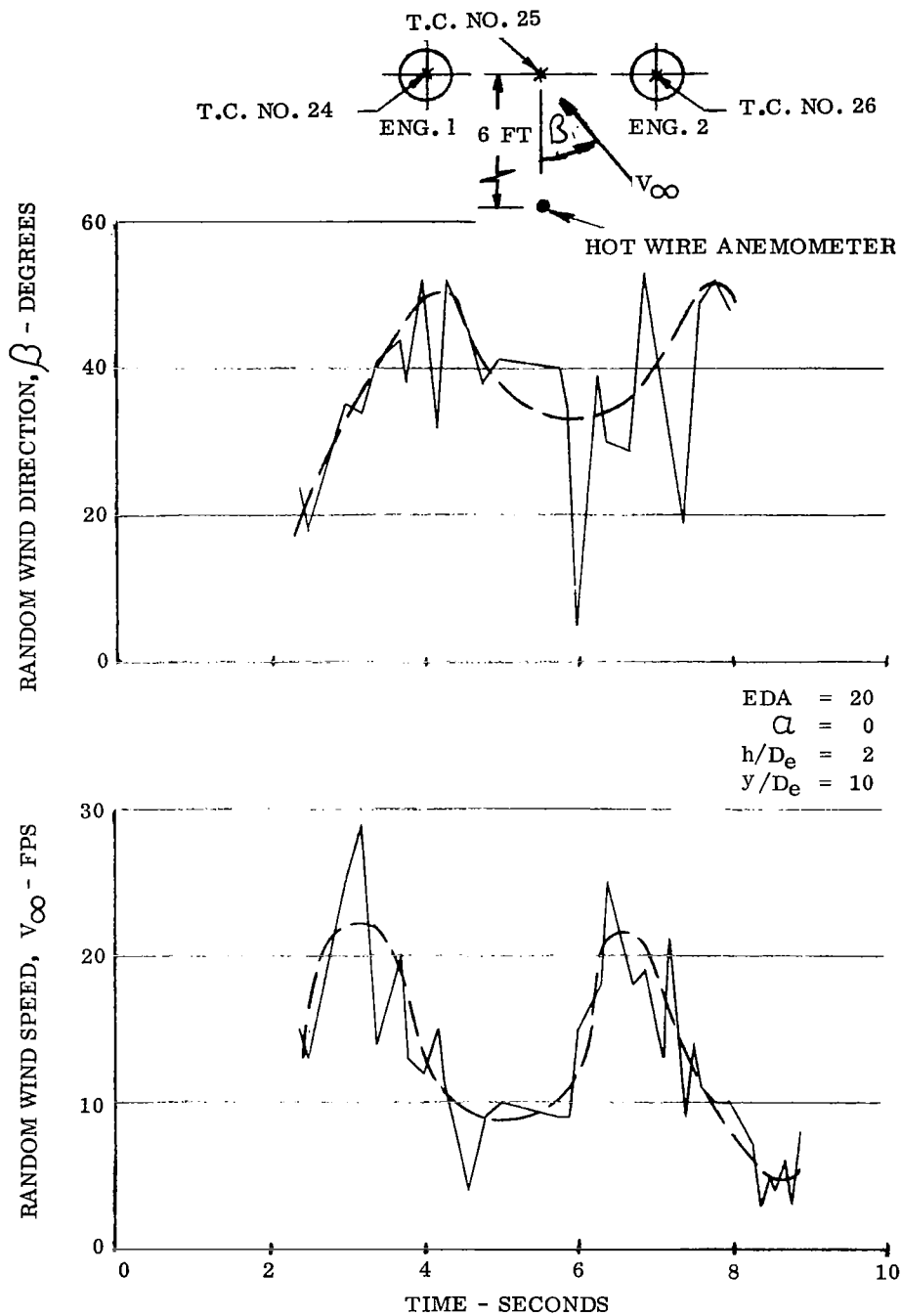
Figure C-1. – Time Histories of Field Temperatures And Random
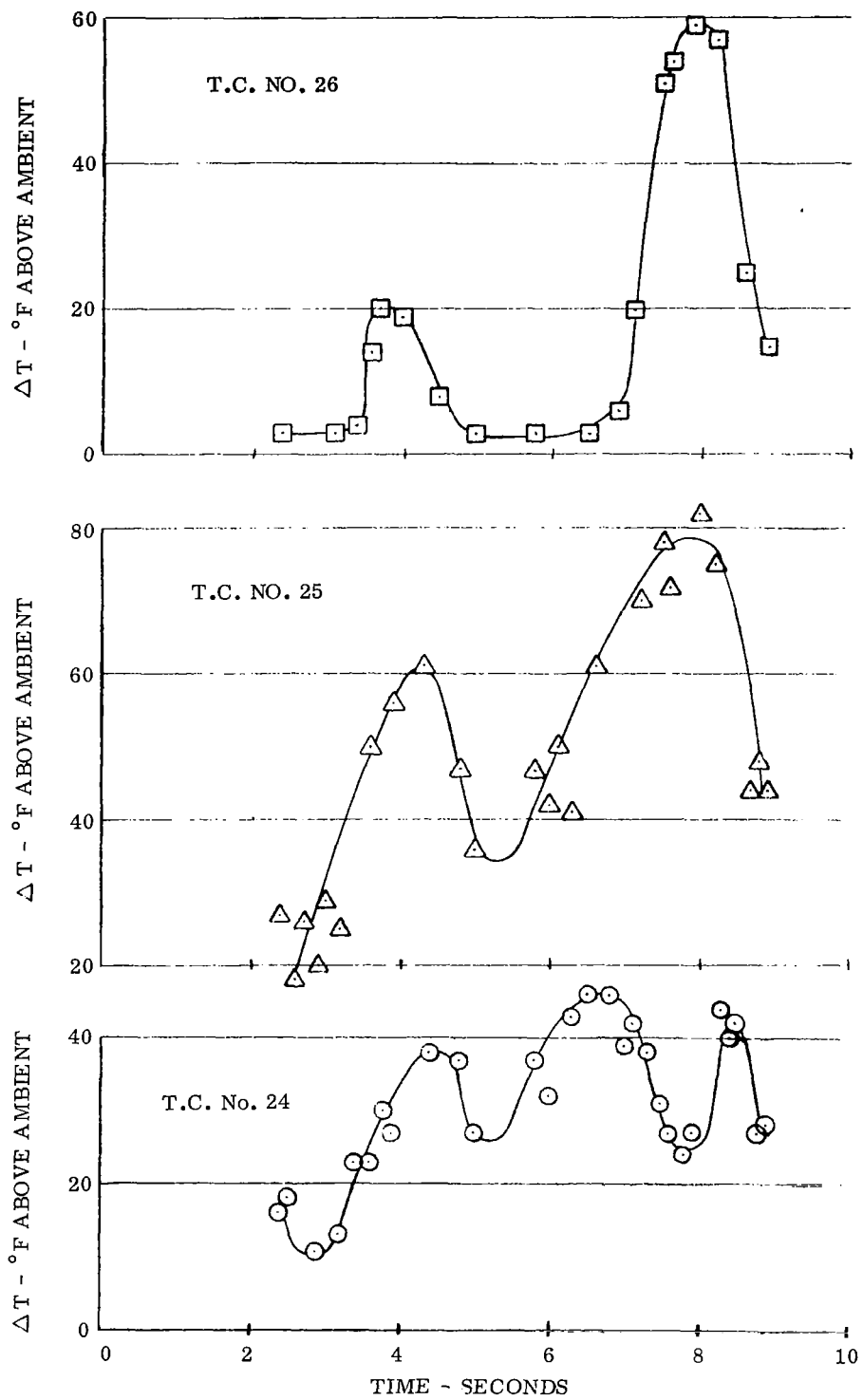Wind Velocity, Dual (circ) Model, $S/S_j = 0$ .
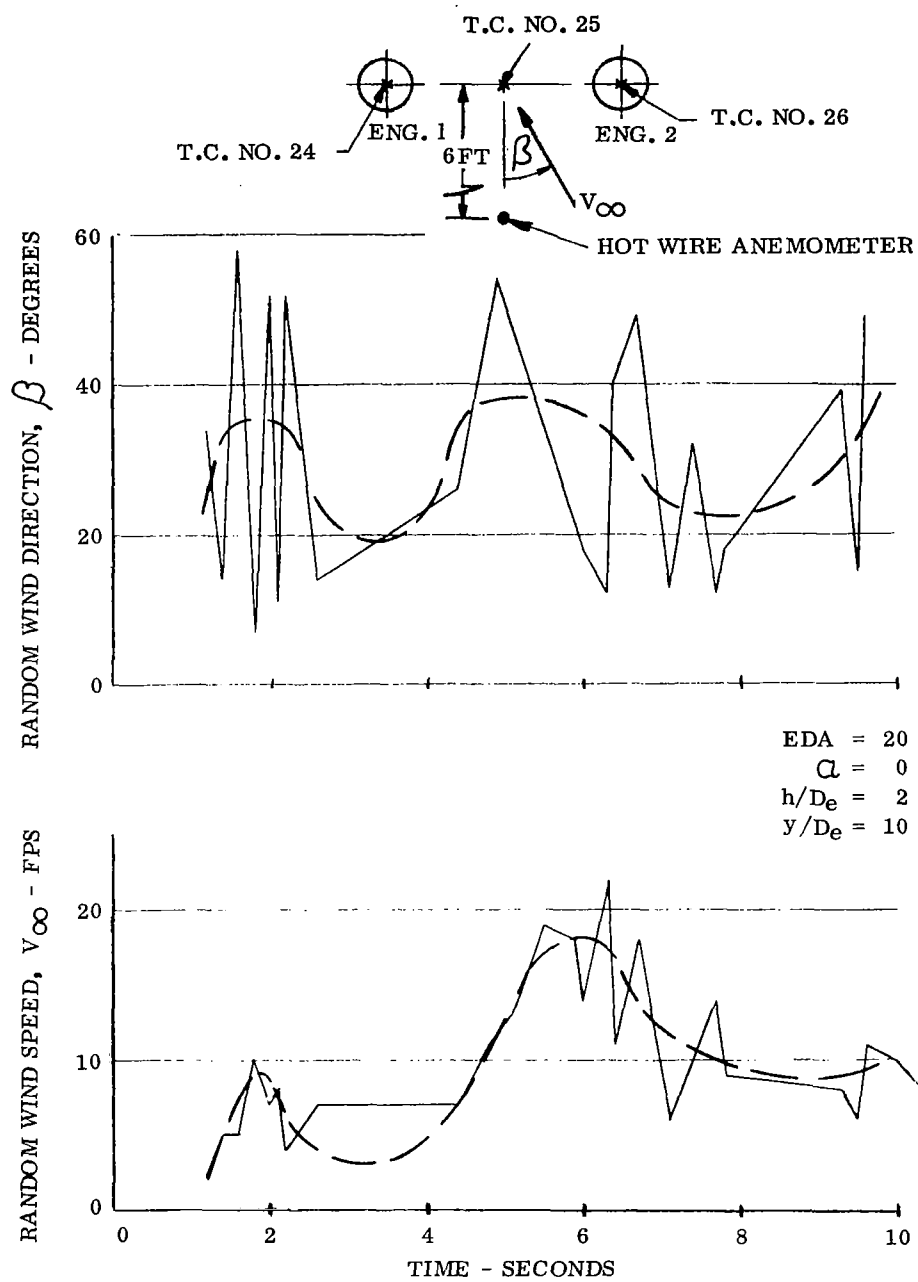
111

Figure C-1. - Concluded.

Figure C-2. - Time Histories of Field Temperatures and Random
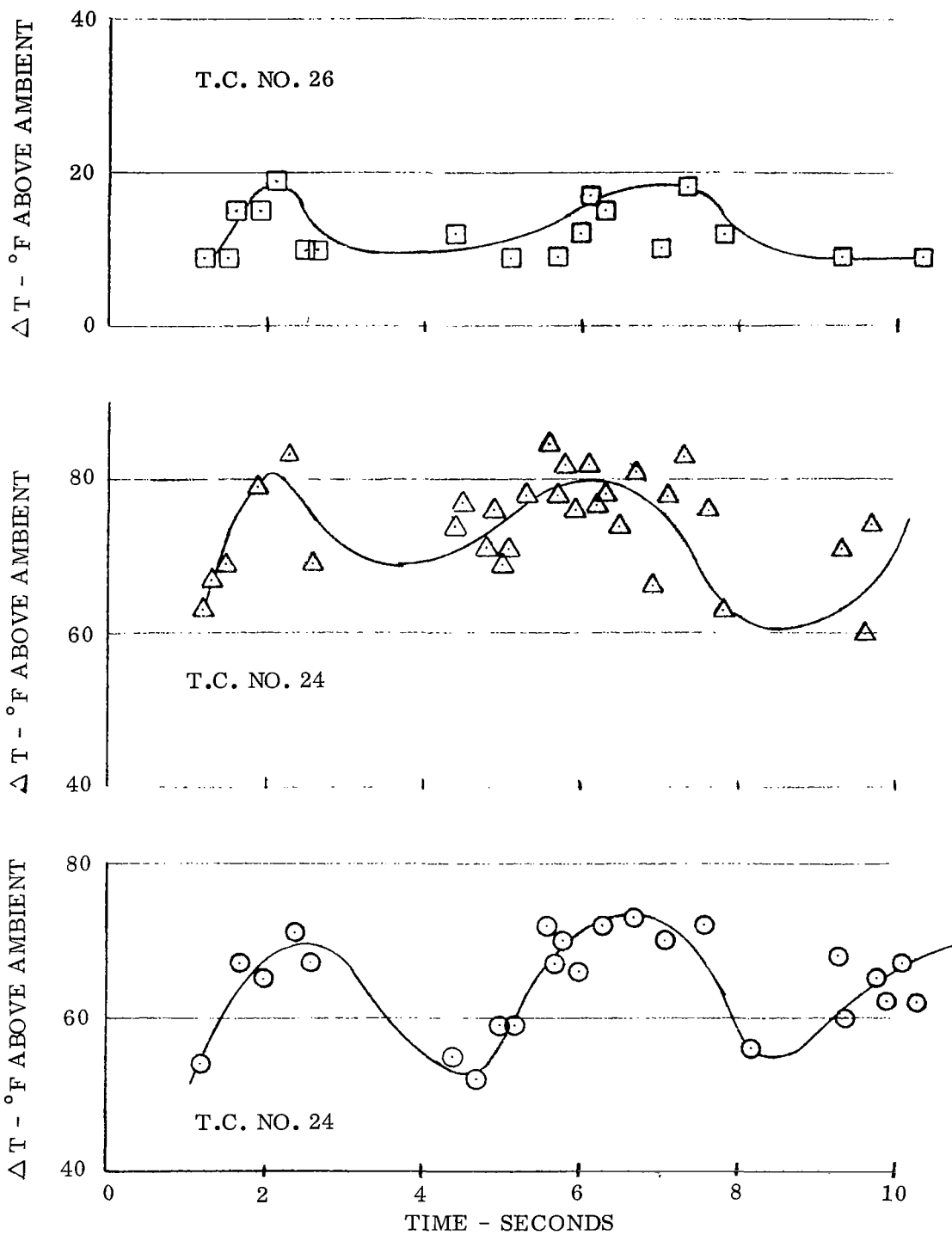Wind Velocity, Dual (circ) Model, $S/S_j = 100$.
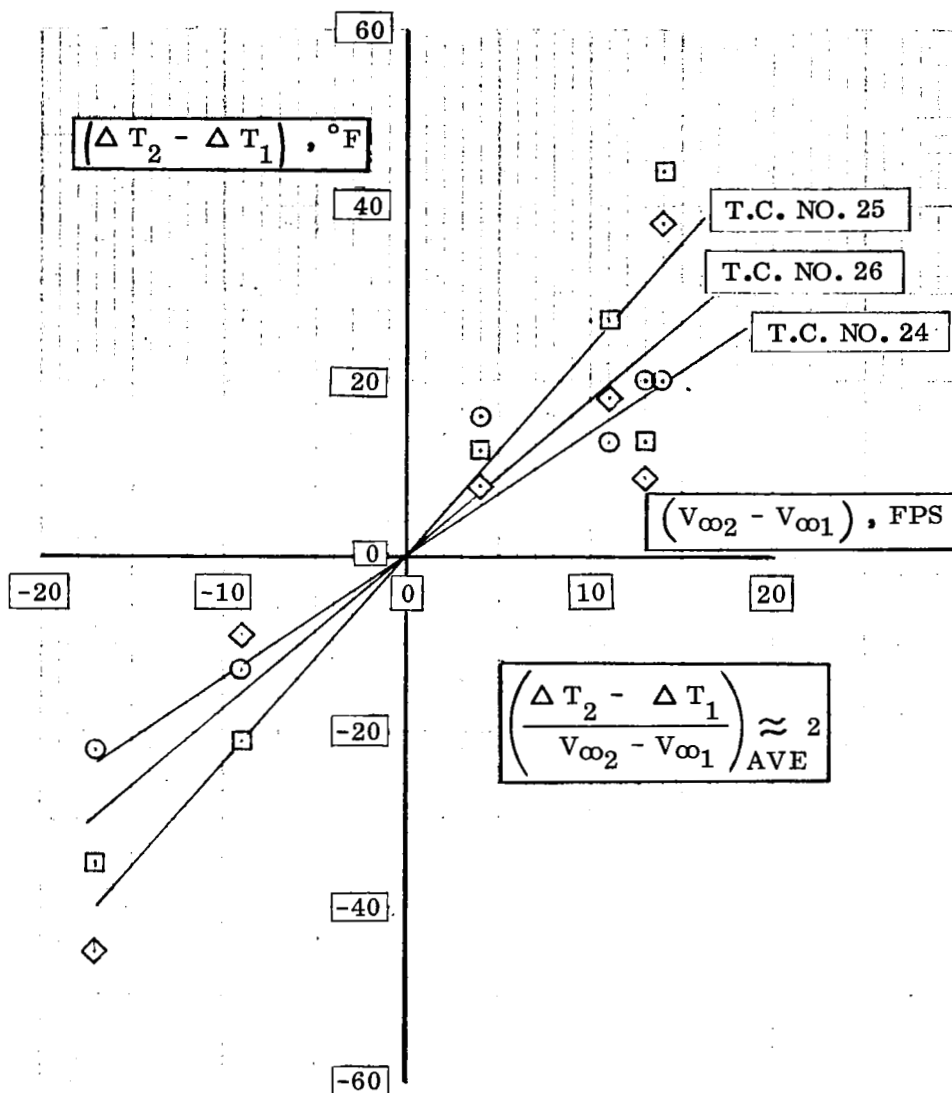
113

Figure C-2. - Concluded.

Figure C-3. – Effect of Random Wind Speed On $\Delta$ T, Dual (circ) Model.

# APPENDIX D

## Scaled NASA Model Exhaust Characteristics

Jet impingement angles ( $\delta$ ). - Small exhaust impingement angles were found to significantly affect ITR (Reference 9), therefore great care was taken to insure vertical jets. Adjustments and measurements were made using a surveyors transit in conjunction with ground flow patterns and the servo positioned exhaust gas probe described in the apparatus section of this report.

The photograph of Figure D-1 shows the ground flow pattern under the exhausts of the NASA model. This oil and lampblack pattern was obtained for hot jets ($T_j = 1200°F$) with exit pressure ratio of 1.7. The fuselage was removed to show the detail of exhaust supply. The impingement points and reinforced ground jets are visible; the scribed lines indicate the geometric center of the jet nozzles. Final adjustments resulted in the impingement angles shown in Figure D-2.

Exhaust jet quality. - Figures D-3 and D-4 show the velocity and temperature characteristics of the exhaust as well as the impact pressure decay rate (both compressible and incompressible) along the jet axis for the NASA model. The velocity and temperature profiles shown in Figure D-3 are for engine number 2 and are typical of all the engine exhausts. From Figure D-4 it is seen that the small scale exhaust pressure decay rate agrees quite well with the large scale NASA data.
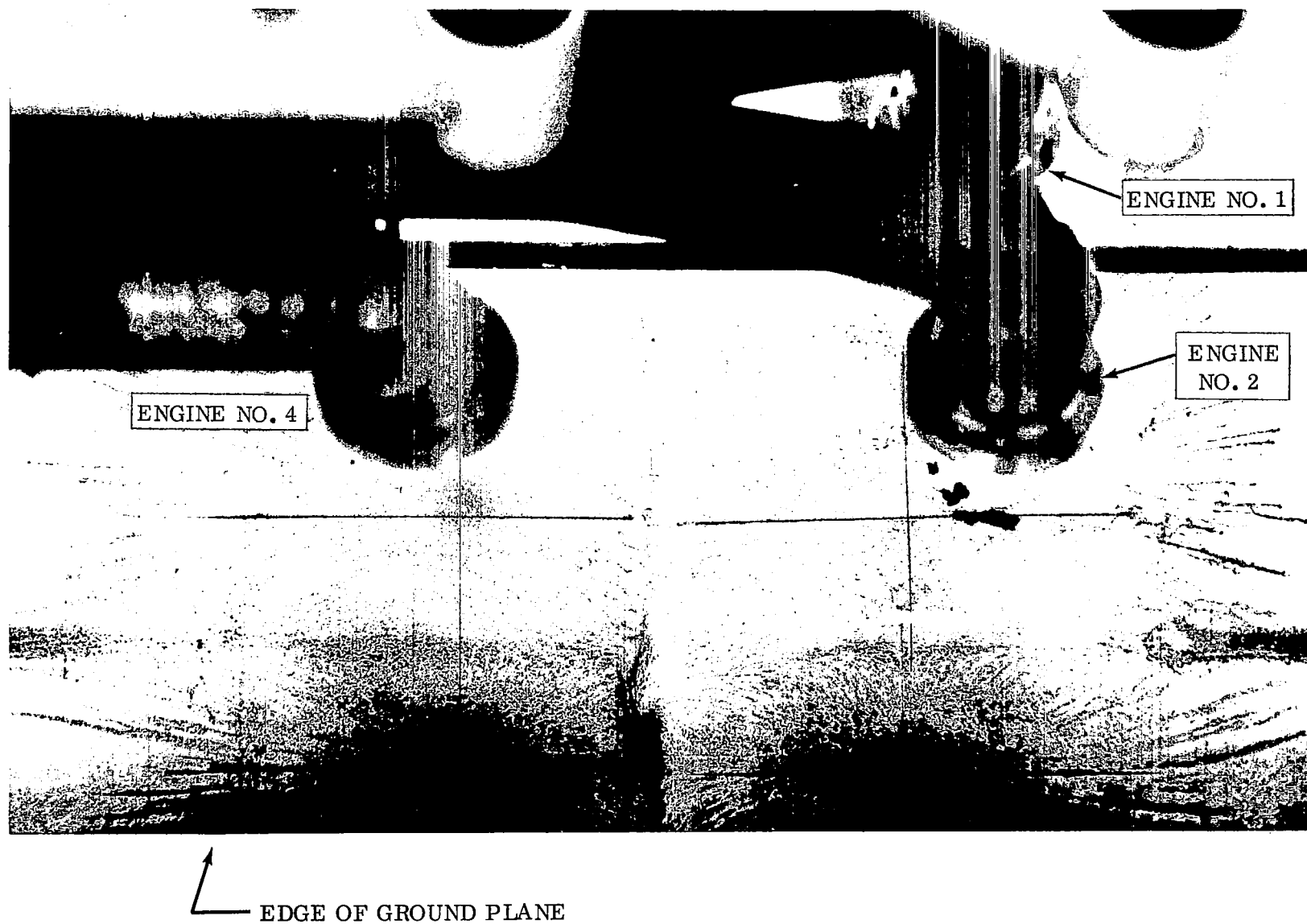
EDGE OF GROUND PLANE

Figure D-1. - Exhaust Ground Flow Pattern, Scaled NASA Model, $P_{T_{ex}}/P_{bar}$ = 1.7, h/D$_e$ = 2.58·

$\delta = .75°$

FORWARD

$\delta = 0°$

ENGINE NO. 1

ENGINE NO. 2

$\delta = 1.1°$

$\delta = 0°$

ENGINE NO. 3

ENGINE NO. 4

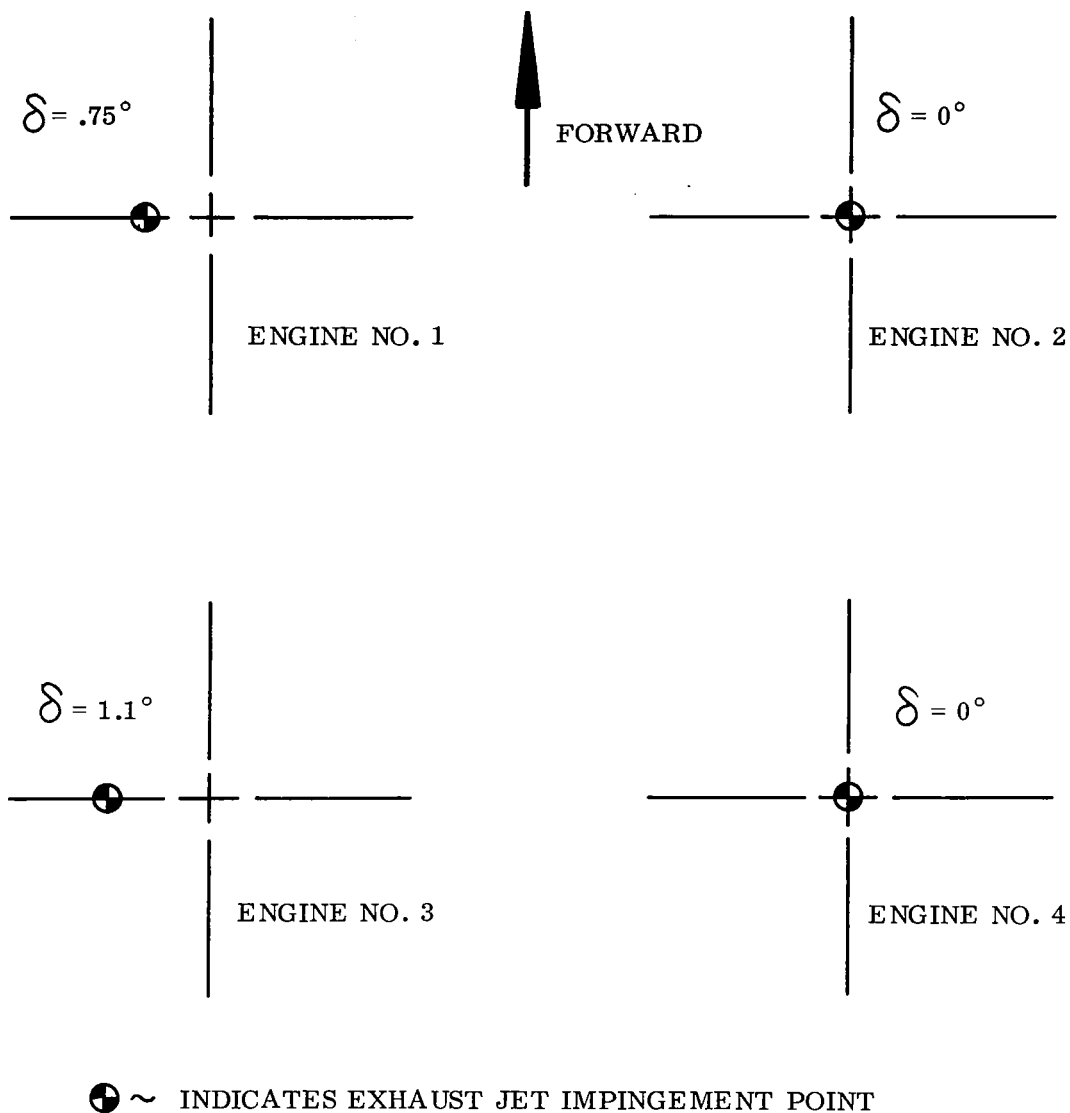⊕ ~  INDICATES EXHAUST JET IMPINGEMENT POINT

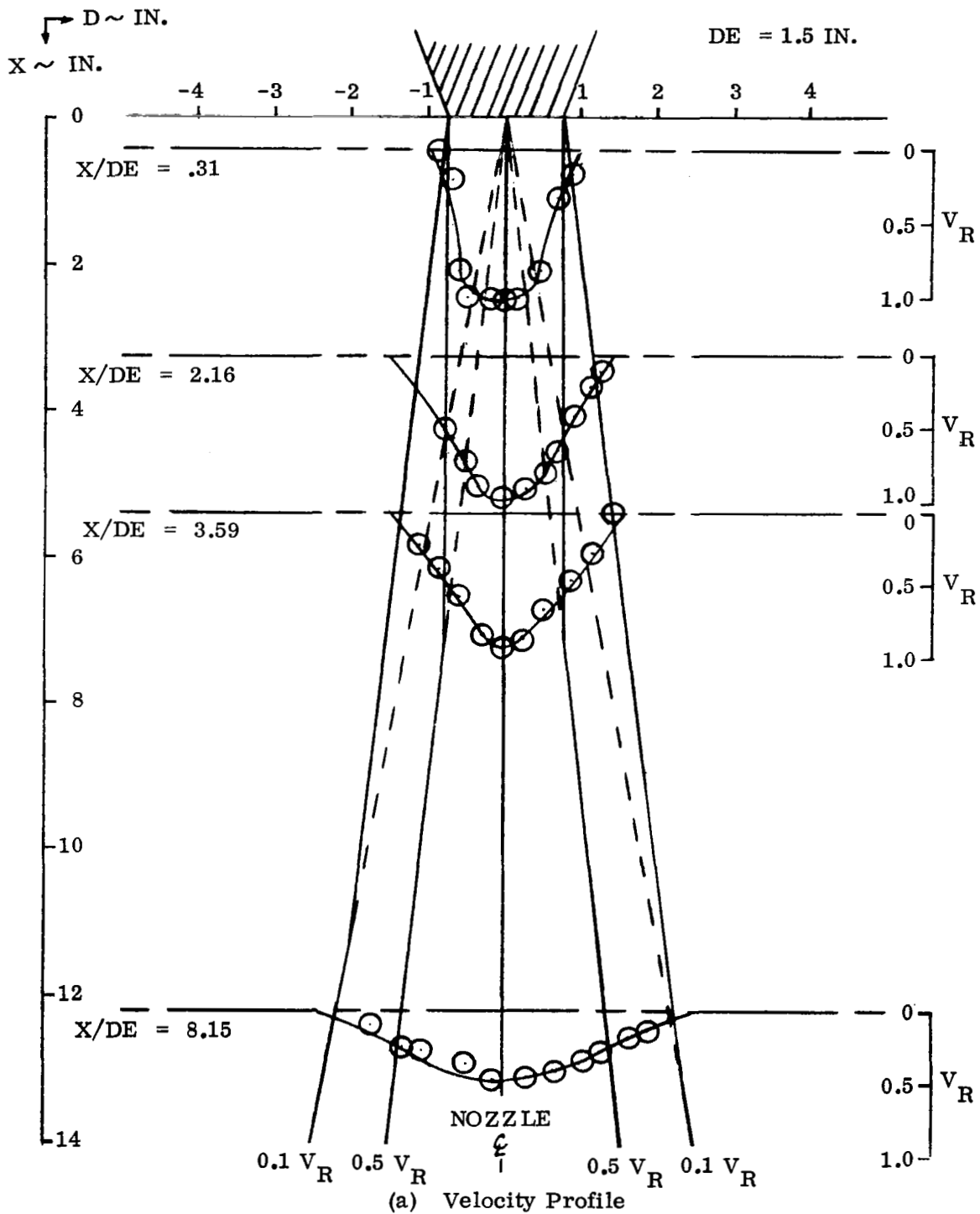Figure D-2. - Exhaust Jet Impingement Angles, NASA Model
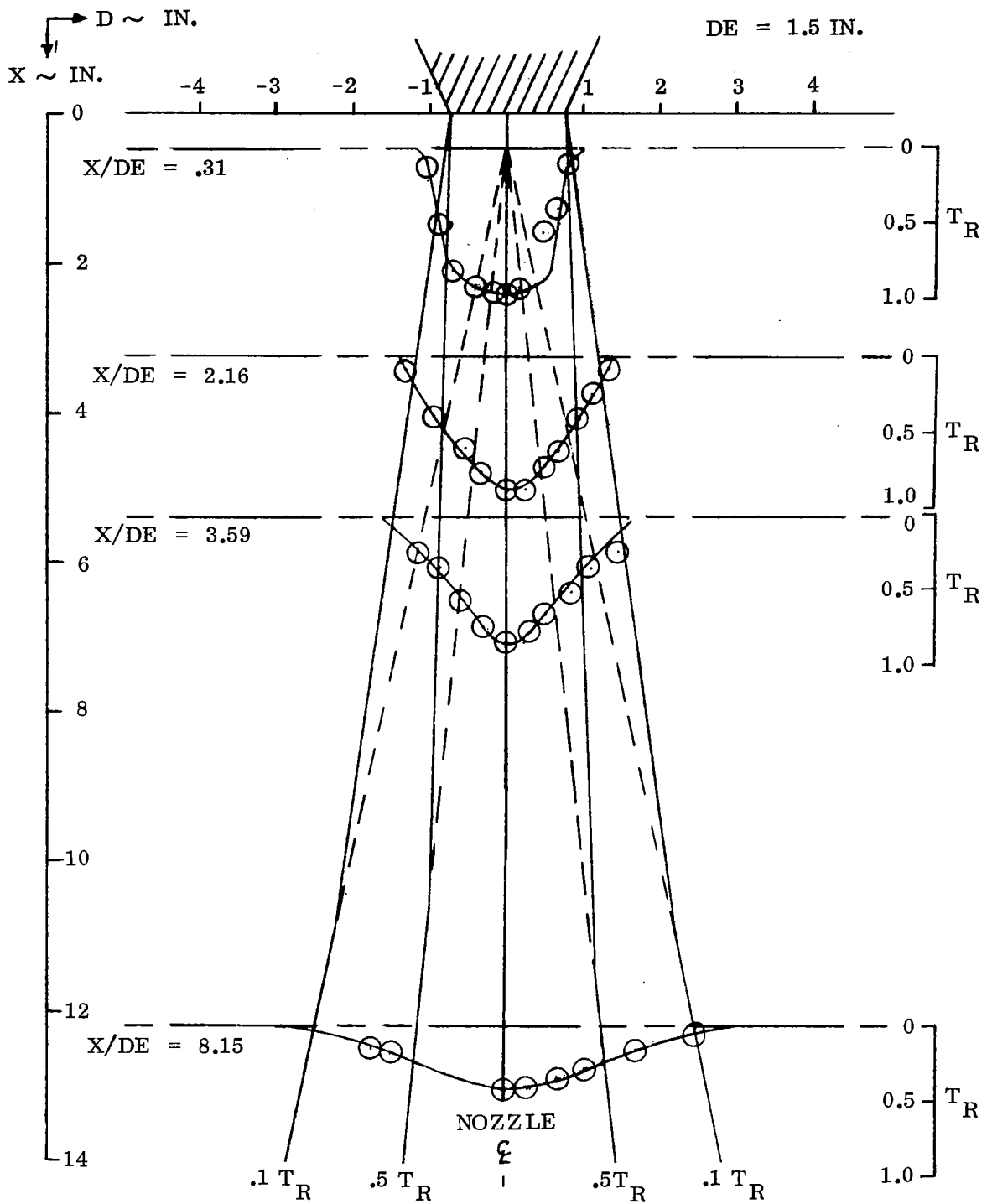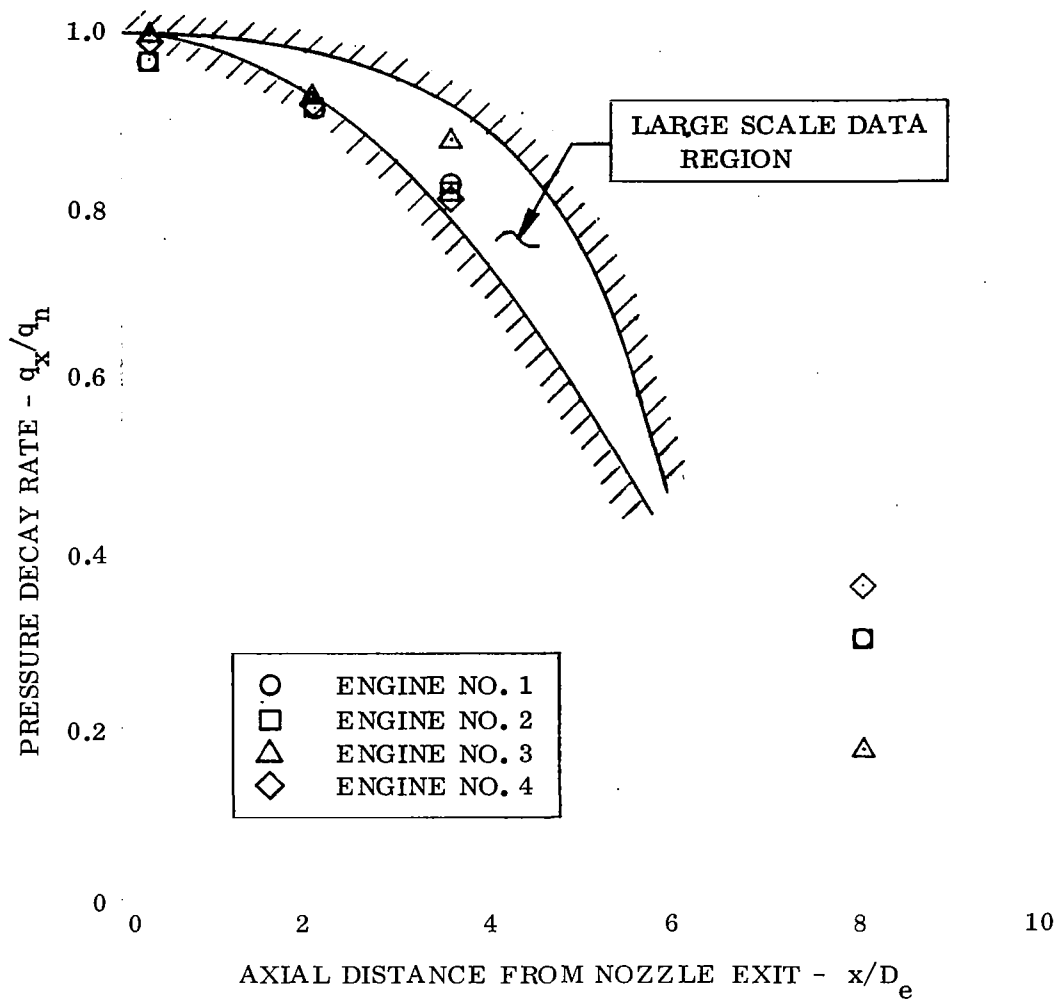
Figure D-3. - Exhaust Survey, Scaled NASA Model .
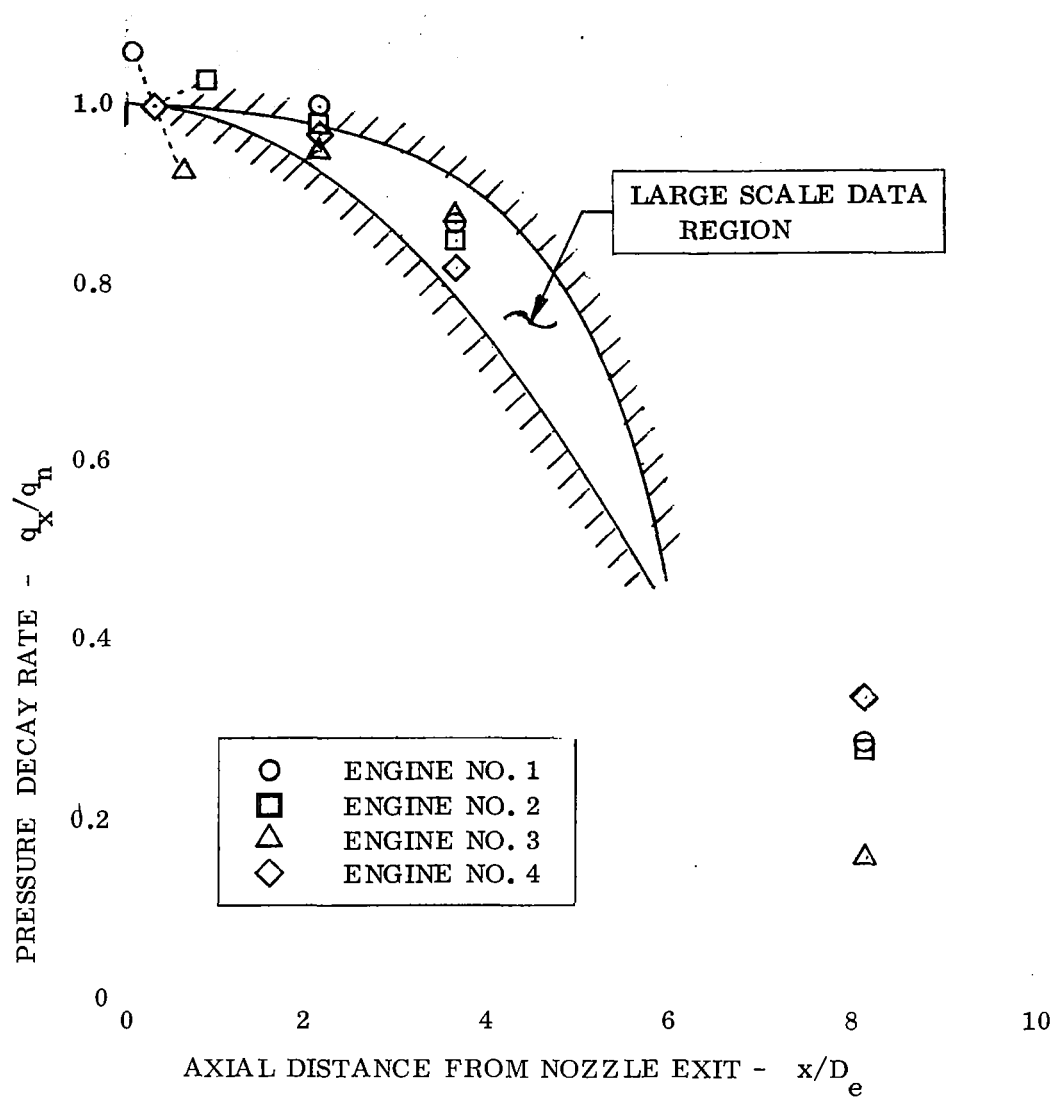
(b) Temperature Profile

Figure D-3. - Concluded .

Figure D-4. – Exhaust Pressure Decay, Scaled NASA Model.

(b) Incompressible

Figure D-4. - Concluded.

# APPENDIX E

## Effect of Inlet and Exhaust Flow Characteristics On ITR

Prior to using the scaled NASA model to obtain ITR data, a series of tests were conducted at $h/D_e$ = 1.2 and again at 8.0 to determine the sensitivity of ITR to variations in inlet and exhaust flow characteristics. The top inlet configuration with $S/S_j$ = 86 was used under zero wind conditions. The ITR under nominal inlet and exhaust conditions ($T_j$ = 1200°F, $P_{T_{ex}}/P_{bar}$ = 1.7, $\dot{w}_{in}/\dot{w}_{ex}$ = 1.0, $\dot{w}_{in}$ = 2.1 lb/sec) was determined and no significant change in ITR was measured when the following parameters were varied independently over the ranges indicated:

| | | |
|---|---|---|
| Exhaust Gas Temperature, | $T_j$ | 600°F to 1400°F |
| Exit Pressure Ratio, | $P_{T_{ex}}/P_{bar}$ | 1.4 to 1.8 |
| Inlet to Exhaust Mass Flow Ratio, | $\dot{w}_{in}/\dot{w}_{ex}$ | .7 to 1.1 |
| Inlet Mass Flow, | $\dot{w}_{in}$ | 1.4 to 2.1 lb/sec |

This result indicated that:

(a)     The ground jets propagated far from the model. They were not peeled from the ground plane and directed back to the model inlet because $V_\infty$ = 0.

(b)     The hot "fountain" gases were effectively blocked by the large ($S/S_j$ = 86) wing.

(c)     The flow field was characterized by a downward flowing mass of relatively cool air from above the model. Even at the low exit pressure ratios the exhaust flow sink was of sufficient strength to maintain the flow field.

It should be noted that these tests indicated that ITR was independent of inlet and exhaust conditions for this specific configuration only and for only $V_\infty$ = 0. Similar tests at various $V_\infty$ and $\theta$ for this and other configurations are required to establish the dependence of ITR on inlet and exhaust conditions.

# REFERENCES

1. Speth, Robert F.; and Ryan, Patrick E.: "A Generalized Experimental Study of Inlet Temperature Rise of Jet V/STOL Aircraft in Ground Effect." Bell Aerosystems Co. Report 2099-928003 (Contract No. N600(19)63320, April 1966. Available from DDC as AD 641610.

2. Ryan, Patrick E.; Heim, Richard J.; and Cosgrove, Wayne J.: "A Generalized Experimental Investigation of Hot Gas Recirculation and Ingestion for Jet VTOL Aircraft", Bell Aerosystems Co., NASA CR-1147, September 1968.

3. McLemore, H. Clyde; and Smith, Charles C., Jr.: "Hot Gas Ingestion Investigation of Large-Scale Jet VTOL Fighter-Type Models", NASA TN D-4609, June 1968.

4. Cox, M.; and Abbott, W.: "Studies of the Flow Fields Created by Single Vertical Jets Directed Downwards Upon a Horizontal Surface". National Gas Turbine Establishment, Memo No. 390, October 1964.

5. Langfelder, Bodeneffekte bei Senkrechtstart-Flugzeugen: (Ground Effects of VTOL Aircraft). EWR-Nr. 37/62, Entwick lungsring Sud (Munchen), March 1963.

6. Harris, A. E.; Marbert, J. A.; and Tatom, J. W.: VTOL Transport Exhaust Gas Ingestion Model Tests. Paper 67 - ENV-17, Seventh Annual National Conference on Environmental Effects on Aircraft & Propulsion Systems, September 1967, Princeton, New Jersey.

7. Lavi, Rahim: Parametric Investigation of VTOL Hot Gas Ingestion and Induced Jet Effects in Ground Proximity. Report NOR 67-32 (Contract NOw 66-0316-f), Northrop Corp., February 1967. Available from DDC as AD 809224.

8. Hall, Gordon R.: Recirculation and Ingestion Characteristics of a Large-Scale VTOL Lift Engine Pod. Northrop Norair, NASA CR-72410, August 1968.

9. Hall, Gordon R. and Rogers, Kenneth H.: Recirculation Effects Produced by a pair of Heated Jets Impinging on a Ground Plane. NASA CR-1307, 1969.